1. Introduction

1.1 General Purpose

The purpose of this thesis is to demonstrate how the observed mesoscale distribution of heavy rainfall in landfalling and transitioning tropical cyclones (TCs) is modulated by interactions between synoptic and mesoscale features in the presence of the complex physiography of the northeast U.S. This research focuses on understanding the key surface and tropospheric dynamics that routinely accompany these TCs. A dataset containing 52 landfalling and transitioning TCs producing greater than 100 mm (~4 in.) of rainfall over the northeast U.S. for 1950–2006 was used to generate a climatology of these TCs. Three representative cases were selected for further study in order to document and illustrate how the dynamical forcing controls the observed mesoscale distribution of heavy precipitation and to provide operational forecasters information that can be utilized for predicting landfalling and transitioning TCs. The remainder of this chapter will review the previous research related to landfalling and transitioning TCs, such as extratropical transition (ET), jet dynamics, frontogenesis (including coastal frontogenesis), orographic precipitation enhancement, and precipitation distribution.

1.2 Motivation and Overview

Despite vast societal and technological advances in atmospheric science, predicting rainfall accompanying TCs still poses a complex challenge. The recent active TC seasons of 2004 and 2005 have grabbed the public eye due to immeasurable loss of property and life near coastal areas, especially over the southeast U.S., where direct wind, storm surge, and precipitation impacts from landfalling TCs were felt. Conversely, there is decreased public awareness of the event after landfall despite the continuing threat to life and property due to flooding (Rappaport 2000; Jones et al. 2003). The aforementioned increase in TC activity has led to a subsequent increase in the number of TC-related flooding events over the northeast U.S. as will be demonstrated in this thesis. This circumstance poses a complex and dangerous situation, because approximately 60% of TC-related deaths in the U.S. are due to freshwater flooding after the TC has moved inland (Rappaport 2000). The study was constructed from 30 years (1970–99) worth of fatality statistics from TCs in the Atlantic.

Difficulty in the prediction of landfalling and transitioning TCs can be attributed to multiple sources. Although TC track improvements have been recently made in numerical weather prediction (e.g., McAdie and Lawrence 2000; Rappaport et al. 2000; Elsberry 2005), inaccuracies in forecasting intensity, ET evolution, winds, and precipitation distribution accompanying a landfalling and transitioning TC has impaired operational forecasts. Much of the forecast difficulty can be attributed to both the intrinsically small-scale nature of a TC and the complex, multiscale interactions between a TC and the surrounding environment during ET (e.g., Jones et al. 2003; Evans et al. 2006). In particular, precipitation forecasts were shown to have inadequate skill past 3 h because the mesoscale features that control the distribution of precipitation accompanying a TC occur on smaller scales than the observations can discern (Marks et al. 1998).

Mesoscale processes such as coastal frontogenesis and topographic-induced ascent can greatly influence small-scale precipitation structures accompanying landfalling and transitioning TCs. These mesoscale processes have been associated with extreme rainfall and inland flash flooding events in the northeastern U.S. For example, coastal frontogenesis and/or orographic precipitation enhancement have been linked to heavy precipitation accompanying transitioning TCs such as Hurricane Camille in 1969 (Schwarz 1970), Tropical Storm Agnes in 1972 (Bosart and Dean 1991), and Hurricane Floyd in 1999 (Atallah and Bosart 2003; Colle 2003).

The Fifth Prospectus Development Team of the U.S. Weather Research Program (PDT-5) identified the improvements needed in numerical weather prediction to effectively save lives and money (Marks et al. 1998). Major research objectives of PDT-5 included: improving forecasts, analysis, and modeling of the surface wind, upper-oceanic thermal, and precipitation fields. Marks et al. (1998) reported that although operational and research models provide information on track, intensity, boundary-layer structure, and rainfall, only validation and assessment of track forecasts are performed. Although a first attempt to determine objectively the model prediction skill of TC rainfall in the U.S. was done by Tuleya et al. (2007), the authors concluded that there are still many unanswered research questions related to model verification of TC rainfall. Verification of TC rainfall and other weather parameters is needed to advance numerical modeling.

1.3 General Characteristics of ET

A large number of TCs undergo ET as they move poleward toward the midlatitudes. Complex structural changes associated with both the cyclone and surrounding environment occur during ET. The purpose of this section is to review the common characteristics associated with ET. After a basic definition is given, the rest of the section will describe some general indicators of ET and a brief climatology of Atlantic basin landfalling and transitioning TCs.

1.3.1 Basic Definition of ET

Although there is no universally recognized definition of ET among the scientific community (Jones et al. 2003), ET can be described as a process where a TC moves poleward into the midlatitudes and evolves into an extratropical cyclone. Accordingly, ET involves a complex process and is usually associated with interactions among several common features accompanying the transitioning TC. The circulation associated with a transitioning TC may enhance the background thermal gradient or interact with a midlatitude extratropical feature such as an upper-level trough. Furthermore, the thermal, cloud, wind, and precipitation fields evolve from a symmetric to a highly asymmetric structure as frontogenetical processes become significant (e.g., Klein et al. 2000). As ET commences, a considerable poleward expansion of the cloud and precipitation fields related to the storm-generated upper-level outflow has been documented (e.g., Bosart and Dean 1991; Harr and Elsberry 2000; Atallah and Bosart 2003). Therefore, heavy precipitation can occur much further away from the center of a transitioning storm when compared to a purely tropical storm.

1.3.2 Indicators of ET

Numerous methods have been constructed to delineate the onset of ET. For example, early studies have attempted to identify important features as indicators of ET such as a preexisting frontal boundary or an extratropical cyclone through detailed surface analyses (e.g., Matano 1958; Matano and Sekioka 1971). Foley and Hanstrum (1994) conducted a more recent study using mean sea level pressure (MSLP) analysis and explained that a key sign of ET was a significant meridional front/ridge couplet and a meridional cold front approximately 1700 km upstream of the cyclone.

The first attempt to define the stages of ET objectively was performed by Klein et al. (2000). Extratropical transition in the western North Pacific was classified as a two-stage process: 1) transformation and 2) reintensification. The transformation stage in ET was described as the evolution of the storm from tropical to baroclinic; while the reintensification stage was defined as the phase where the transitioning storm developed into an intensifying extratropical cyclone. Klein et al. (2000) constructed a three-step conceptual model of the transformation stage that illustrated the evolution of a transitioning TC in all of the 30 cases examined. The start and end of the transformation stage was determined objectively by taking into account the position of the storm in relation to the preexisting midlatitude baroclinic zone. The transformation stage ended when the storm center became entrenched in cold, descending air over the preexisting baroclinic zone. Conversely, transitioning TCs that did not become entrenched in the baroclinic zone typically could not complete the transformation stage and subsequently dissipated.

Another attempt to define the stages of ET objectively was performed by Evans and Hart (2003). They used a cyclone phase space (CPS) developed by Hart (2003) to characterize the evolution of ET. More specifically, thermal asymmetry across the transitioning TC was calculated from the difference between the right and left of storm-motion-relative 900–600-hPa thickness to determine the onset of ET; while lower-

(upper-) level thermal structure of the transitioning TC was calculated from the 900–600-hPa (600–300-hPa) thermal wind to determine the completion of ET. Evans and Hart (2003) used the CPS to identify objectively the onset and completion times of ET during recent Atlantic basin transitioning TCs such as Floyd (1999) and Erin (2001). Transition from a deep warm-core, symmetric TC to a deep cold-core, asymmetric extratropical cyclone were observed in both cases. Hart et al. (2006) constructed a CPS composite consisting of 34 TCs that experienced ET over the North Atlantic during 1998–2003, where the composite TC evolves from a symmetric warm core to an asymmetric cold core structure (Fig. 1.1.). The structural changes found in the 34-storm composite are similar to the structural changes found in the individual storms studied in Evans and Hart (2003).

Jones et al. (2003) proposed a generalized two-stage process to identify ET (Fig. 1.2). This classification scheme was developed by combining the results of Klein et al. (2000) and Evans and Hart (2003). As the TC moves poleward, onset of the transformation stage is marked by the start of cyclone response to environmental changes (e.g., increased thermal and moisture gradients, stronger vertical wind shears, frictional and orographic influences, and upper-level trough interactions). As a result of these environmental changes, the TC typically weakens, increases translation speed, loses its warm core structure, and develops appreciable thermal, wind, cloud, and precipitation asymmetries. Following completion of the transformation stage, the storm is classified as extratropical and may develop characteristic extratropical features such as an upstream tilt with height, a comma-shape cloud structure, and a warm front.

1.3.3 Climatology of Landfalling and Transitioning TCs in the Atlantic Basin

Previous studies have shown that named Atlantic basin TCs (i.e., tropical storms and hurricanes) develop most frequently in the months of August through October (e.g., Landsea 1993; Neumann et al. 1993). More specifically, approximately 95% of all major Atlantic basin hurricanes for 1886–1991, category 3 or higher on the Saffir–Simpson scale (Simpson 1974), occur during the months of August and September (Landsea 1993). Landsea (1993) also determined that, on average, U.S. landfalling major hurricanes affected Gulf Coast States earlier in the calendar year than East Coast states.

Extratropical transition in the Atlantic basin was investigated primarily through case study analysis until Hart and Evans (2001) conducted a detailed ET climatology for this region. The results from Hart and Evans (2001) showed that 46% of all Atlantic TCs identified by the National Hurricane Center (NHC) for 1950–96 experienced ET; while 50% of all Atlantic TCs that made landfall on the eastern coast of the U.S., Canada, or the western coast of Europe experienced ET. This study also established that both the number of Atlantic basin TCs and TCs that experienced ET occurred most frequently in the months of August through October (Fig 1.3). In particular, approximately 50% of TCs for 1899–1996 experience ET in the Atlantic basin during the months of September and October. The results from Hart and Evans (2001) agreed with those from Landsea (1993) and Neumann et al. (1993), where August through October represented the peak months for TC activity.

Hart and Evans (2001) also determined that ET of a TC is more likely to occur over land than over the Atlantic Ocean because troughs and strong frontal zones are more common over land. The majority of TCs that formed either at low latitudes (i.e., the deep tropics) or off the southeast U.S. coast over the Gulf Stream intensified after the completion of ET; while none of the TCs that formed over the Gulf of Mexico intensified after the completion of ET (Fig. 1.4a). Furthermore, the transition location for both strengthening (Fig. 1.4a) and weakening (Fig. 1.4b) storms primarily occurred between 37° and 50°N. Hart and Evans (2001) suggested that this latitude band might be the most conducive for ET because the greatest baroclinic instability occurs in this band during the late summer and fall months of August through October.

1.4 Synoptic-Scale Processes associated with Landfalling and Transitioning TCs

This section will incorporate both quasigeostrophic (QG) and potential vorticity (PV) approaches to understand key synoptic-scale dynamic and thermodynamic processes involved in landfalling and transitioning TCs such as TC- trough, ridge, and jet interactions. A historical literature review will be used to provide evidence for relevant dynamic and thermodynamic mechanisms found in previous cases.

1.4.1 Quasigeostrophic and Potential Vorticity Dynamics

Although QG theory would not apply to the smaller-scale processes found in landfalling and transitioning TC events, it can still be employed to obtain an understanding (i.e., situational awareness) of these events (e.g., Jones et al. 2003; Evans and Prater-Mayes 2004). It is possible to diagnose areas of synoptic-scale forcing for vertical motion through use of the QG omega equation (Bluestein 1992, section 5.6.2). Forcing for ascent can be attributed to an upward increase of cyclonic vorticity advection and/or a local maximum of the Laplacian of warm-air advection. When overlaid over a moisture-laden environment, tropospheric-deep ascent can provide favorable conditions for heavy rainfall accompanying a TC (Bosart and Carr 1978; DiMego and Bosart 1982a,b; Atallah and Bosart 2003).

The Q vector form of the QG omega equation (Hoskins et al. 1978; Hoskins and Pedder 1980) provides forecasters with a convenient method for diagnosing areas of QG forcing for ascent. The Q vector can be partitioned into two components: 1) cross-isentrope, where mesoscale banded regions of QG forcing for vertical motion exists within the frontal zones, and 2) along-isentrope, where synoptic-scale, cellular regions of QG forcing for vertical motion produce a wavelike pattern in the thermal field (Keyser et al. 1988, 1992; Kurz 1992). The results from these previous studies can be applied to understand the interaction between a TC vortex and a midlatitude baroclinic zone during ET.

Potential vorticity is an atmospheric variable that integrates both thermodynamic and dynamic properties. Potential vorticity can be defined as the product of absolute vorticity and static stability on an isentropic surface and is a conservative property for adiabatic and frictionless processes (Bluestein 1992, section 4.4.5). A positive PV anomaly on the dynamic tropopause implies upshear (downshear) ascent (descent) of air parcels along an isentropic surface (Hoskins et al. 1985, section 4).

The use of PV can provide forecasters with improved insight into the ET process (Jones 2003). Tropical cyclones are associated with a strong positive PV anomaly (cyclonic flow) throughout the troposphere except at upper-levels, where a weaker negative PV anomaly exists (anticyclonic flow) at larger radii; whereas extratropical cyclones are associated with a strong positive PV anomaly in the middle and upper troposphere at large radii (Jones et al. 2003). As a result, the interactions between the distinct tropical and extratropical features can be easily traced. Additionally, the non-conservation of PV is helpful to understand the impact of diabatically modified PV air from the TC on the midlatitude flow during ET.

1.4.2 Upstream Trough Interactions

The interaction between a midlatitude upper-level trough and a TC during ET has been shown to facilitate cyclone development in western North Pacific storms such as Opal and David in 1997 (Harr and Elsberry 2000; Klein et al. 2000), and in Atlantic storms such as Agnes in 1972 (DiMego and Bosart 1982a,b), Earl in 1998 (McTaggart Cowan et al. 2001), Floyd in 1999 (Atallah and Bosart 2003), and Irene in 1999 (Evans and Prater-Mayes 2004). Compositing studies have shown that the structure of a midlatitude upper-level trough is a principal factor for determining TC intensity during ET (Harr et al. 2000; Klein et al. 2000; Hanley et al. 2001; Sinclair 2002; Ritchie and Elsberry 2003, 2007; Atallah et al. 2007).

The reintensification process during ET has been characterized as a type-B development (Petterssen and Smeybe 1971) when the upper-level trough advances toward the remnant TC (e.g., DiMego and Bosart 1982a,b; Ritchie and Elsberry 2003, 2007). In general, type-B cyclogenesis occurs as upper-level divergence and midlevel cyclonic vorticity advection become superimposed over a preexisting low-level baroclinic zone. During ET in the Northern Hemisphere, conditions become favorable for redevelopment when the upper-level trough enhances cyclonic vorticity advection aloft over a region of warm advection to the east of the transitioning TC across the preexisting baroclinic zone.

Ritchie and Elsberry (2003, 2007) examined the impacts of phasing between the upper-level trough and TC during ET. Simulations from both studies revealed that while the initial strength of the trough had minimal influence on the peak intensity of the extratropical cyclone after the completion of ET, the reintensification of a transitioning cyclone was highly sensitive to the initial distance between the trough and TC. Accordingly, a proper phasing between the trough and TC during ET was important for extratropical cyclone reintensification.

A composite study by Harr et al. (2000) of 30 ET cases in the western north Pacific revealed two distinctive synoptic-scale trough patterns (Fig. 1.5). A northwest flow pattern was characterized by a midlatitude trough positioned to the northwest of a transitioning TC. The transitioning TC subsequently intensified as it moved northeastward. A northeast flow pattern occurred when the approaching TC moved in between a trough positioned to the northeast and a ridge positioned to the southeast. Accordingly, the transitioning TC entered a predominantly zonal confluent flow and did not intensify.

Hart et al. (2006) investigated the role of the upstream trough at the start of ET in both intensifying and weakening Atlantic basin TCs after the completion of ET. Composite results show that TCs that intensified (weakened) after the completion of ET were associated with a negatively (positively) tilted trough upstream at the start of ET. Also, the distance between the upstream trough and TC was less in intensifying cases than in weakening cases.

A PV perspective has been used to examine TC–trough interactions during ET. Key interactions between the PV anomalies associated with the TC and trough, respectively were identified during the ET of Floyd in 1999 (Atallah and Bosart 2003), Irene in 1999 (Evans and Prater-Mayes 2004), and in composite studies (e.g., Hanley et al. 2001; Atallah et al. 2007). Interactions between two distinct upper-level positive PV anomalies associated with the TC and the advancing trough created a tropospheric-deep baroclinic zone with isentropic ascent over the respective upper-level PV anomalies (Atallah and Bosart 2003; Atallah et al. 2007). Furthermore, the interactions between these PV anomalies led to a distinct shift from a positive to a neutral or negative tilt of the upper-level trough during ET.

1.4.3 Downstream Ridge Building and Jet Dynamics

Downstream ridge building and jet dynamics play a significant role during ET events (Hanley et al. 2001; Klein et al. 2002; Atallah and Bosart 2003; McTaggart-Cowan et al. 2003; Ritchie and Elsberry 2003; Atallah et al. 2007). These studies have revealed that upper-level (anticyclonically curved) outflow from a transitioning TC can lead to downstream ridging and ensuing jet streak enhancement in the equatorward entrance region. As a result, intensification of the implied thermally direct ageostrophic circulation in the entrance region can lead to vigorous upper-level divergence and ascent on the equatorward side of the entrance region. Kinetic energy budget diagnostics have also been used to investigate jet streak development during the ET of Hazel in 1954 (Palmén 1958), Candy in 1968 (Kornegay and Vincent 1976), Agnes in 1972 (DiMego and Bosart 1982b), and David in 1997 (Harr et al. 2000). During ET, the generation of kinetic energy in lower levels was due to diabatic processes and cross-contour flow towards lower heights; while the generation of kinetic energy in upper levels was due to cross-contour flow towards lower heights. Outflow from the transitioning TC resulted in a significant exportation of kinetic energy into the downstream midlatitude environment at upper levels. The conversion of available potential energy into kinetic energy was essentially manifested as a thermally direct vertical circulation when the transitioning TC and the midlatitude circulation (i.e., jet streak) became coupled.

Potential vorticity methods have been used to further understand the importance of TC-induced diabatic heating on downstream ridge building and jet enhancement during ET (e.g., Bosart and Lackmann 1995; Harr and Elsberry 2000; Harr et al. 2000; Atallah and Bosart 2003; Atallah et al. 2007). Diabatic processes such as latent heating associated with deep convection and precipitation can act to reduce the PV downstream of the TC at upper levels, subsequently leading to downstream ridge amplification and jet development.

1.5 Mesoscale Processes associated with Landfalling and Transitioning TCs

Mesoscale processes such as frontogenesis (including coastal frontogenesis) and orographic precipitation enhancement accompanying U.S. landfalling and/or transitioning TCs such as Camille in 1969 (Schwarz 1970), Agnes in 1972 (Bosart and Carr 1978; Bosart and Dean 1991), and Floyd in 1999 (Atallah and Bosart 2003; Colle 2003) often resulted in the formation of mesoscale precipitation structures. In particular, this section reviews the orographic effects of the Appalachians on rainfall over the eastern U.S. See

DeLuca (2004) and Srock (2005) for another detailed literature review on cool- and warm-season cold-air damming and coastal fronts.

1.5.1 Frontogenesis

The interaction between a TC vortex and a preexisting baroclinic zone can lead to the formation of frontal zones as a landfalling or transitioning TC approaches the midlatitudes. Asymmetries in the cloud, precipitation, and thermal structure accompanying the TC become evident as a result of frontogenesis (Bosart and Dean 1991; Klein et al. 2000; Harr and Elsberry 2000). Harr and Elsberry (2000) used vector frontogenesis diagnostics (Keyser et al. 1988) to examine patterns of frontogenesis in Typhoon David (1997) and Typhoon Opal (1997) as they experienced ET over the western North Pacific. Similar to the Q vector partition discussed in section 1.4.1, Keyser et al. (1988) separated the frontogenesis vector (F vector) into a cross-isentrope component (F_n), which is associated with changes in the magnitude of the potential temperature gradient, and an along-isentrope component (F_s), which is associated with changes in the direction of the potential temperature gradient. Harr and Elsberry (2000) found the largest values of frontogenesis associated with F_n and ascent to the north and east of David and Opal during ET. This area of warm frontogenesis, which was primarily due to horizontal deformation, was better defined than the area of cold frontogenesis in both transitioning typhoons. Frontogenesis associated with F_n to the north and east of the TC signified the evolution from a symmetric TC to an asymmetric extratropical cyclone. The pattern of F_s accompanying David during ET contributed to thermal wave amplification and provided dynamical support for the transition of David into a strong extratropical cyclone. Conversely, the pattern of F_s in the case of Opal did not contribute to significant thermal wave amplification so that reintensification did not occur.

1.5.2 Coastal Frontogenesis

The first refereed literature on coastal frontogenesis documented the existence of a shallow mesoscale boundary with frontogenesis along the New England coast during the winter, when land–sea temperature contrasts are greatest (Bosart et al. 1972). Enhanced precipitation often fell on the cold side of the mesoscale boundary, where a 5°–10°C temperature difference existed over a 5–10-km distance (Bosart et al. 1972; Bosart 1975). Differential friction within a baroclinic zone in the boundary layer produced deformation and convergence patterns favorable for coastal frontogenesis (Bosart 1975). Early studies (e.g., Bosart et al. 1972; Bosart 1975; Richwein 1980) showed that coastal fronts were regularly associated with an anticyclone to the north of the surface boundary, where northerly flow inland of the coast trapped a shallow layer of cold air against the mountains (i.e., cold-air damming). Orographically-induced coastal frontogenesis was shown to develop well inland and independent of the background thermal differences between the land and ocean with a maximum ascent of 2–3 m s^{-1} over the leading edge of the cold pool (Nielsen 1989; Nielsen and Neilley 1990). Coastal fronts have also been associated with a shallow thermally direct circulation (Bosart 1975; Marks and Austin 1979) and have acted as a baroclinic track for extratropical cyclones (e.g., Bosart 1981; Bosart and Lin 1984).

Numerical modeling of cool-season coastal fronts was done by Ballentine (1980) and Roebber et al. (1994). Simulations of a case documented previously by Bosart

(1975) showed that the primary physical mechanism responsible for coastal frontogenesis was heat fluxes from the ocean, while orography, differential friction, and latent heating played a secondary role (Ballentine 1980). A high-resolution model study by Roebber et al. (1994) found that the location of heaviest precipitation was dependent on both the inland penetration and orientation of the coastal front in New England.

Warm-season coastal frontogenesis has been documented along the Texas coast on 17–21 September 1979 (Bosart 1984) and on 16–19 September 1984 (Bosart et al. 1992). In both cases, tropical cyclogenesis occurred over a weak surface baroclinic zone along the coast. Heavy precipitation and deep convection was focused along the coastal front with over 500 mm of rainfall in a 4–5-day period.

Coastal fronts have also been documented in landfalling and transitioning TCs such as Agnes in 1972 (Bosart and Dean 1991), Floyd in 1999 (Atallah and Bosart 2003; Colle 2003), and Irene in 1999 (Evans and Prater-Mayes 2004) over the eastern U.S. Analogous to wintertime events, the heaviest rainfall accompanying Agnes was focused in a band along and on the cold side of the coastal front as revealed by 12-h accumulated precipitation analyses ending 0000 UTC 22 June 1972 (Fig. 1.6a), 1200 UTC 22 June 1972 (Fig. 1.6b), and 0000 UTC 23 June 1972 (Fig. 1.6c). For example, ~225 mm of rainfall was found in the 12-h period ending 1200 UTC 22 June 1972 along and just to the west of the mesoscale surface boundary that was located almost directly north of Agnes (Fig. 1.6b). The coastal front characterized by an average temperature contrast of ~3°C across the baroclinic zone was observed as Agnes moved northward and formed due to the cold-air damming setup east of the Appalachians (Bosart and Dean 1991).

1.5.3 Topographic Effects over the Eastern U.S.

Schwarz (1970) documented extreme rainfall over Virginia due to Hurricane Camille (1969). Rainfall amounts as high as 625 mm were measured over parts of central Virginia in the 36-h period ending 1800 UTC 20 August 1969 (Fig. 1.7). The persistent low-level southeasterly flow in advance of Camille transported moist tropical air toward the eastern sides of the central Appalachians. Consequently, the heaviest rainfall occurred over the southeast-facing slopes of the Blue Ridge Mountains, where conditions were favorable for orographic precipitation enhancement.

Climatological studies of rainfall accompanying TCs that crossed the Appalachian Mountains were conducted by Haggard et al. (1973) and Hudgins (2004). Haggard et al. (1973) required a TC to pass over an elevation of ~300 m in the Appalachians in order to be included in their study, thereby restricting the total number of storms in the dataset for 1900–69 to 36. While the heaviest rainfall usually occurred along the coast near landfall, there still was a 40% probability that a TC would be accompanied by a 24-h rainfall event greater than ~250 mm over the steepest slopes of the Appalachians. Hudgins (2004) observed that 150–250 mm of rainfall over the central Appalachians often accompanied inland-moving TCs for 1950–2003. In the central Appalachians, strong orographic precipitation enhancement occurred most frequently over the eastern sides of the Blue Ridge Mountains. Furthermore, Hudgins (2004) determined that southeast U.S. landfalling TCs produced heavier rainfall amounts in the study region than Gulf Coast landfalling TCs.

Passarelli and Boehme (1983) researched orographic precipitation enhancement in New England. Topographical effects were important for determining the distribution of pre-warm-frontal precipitation over southern New England. Numerical model results showed that a 20–60% precipitation enhancement occurred over upslope regions compared to downslope and coastal regions. The authors hypothesized that scavenging of water vapor in orographic clouds through forced orographic ascent, similar to the seeder–feeder mechanism discussed by Bergeron (1949), was important for orographic precipitation enhancement.

In a comprehensive climatological study on ET in the Atlantic basin, Hart and Evans (2001) examined the orographic impact on rainfall accompanying landfalling and/or transitioning TCs over the eastern U.S. The impact of orography on TC rainfall was quantified through an examination of the mean return periods for heavy (5-cm and 10-cm) rainfall events associated with TCs. The smallest mean return period (i.e., maximum frequency) for heavy rainfall events was found over the eastern slopes of the Appalachians, especially in eastern Pennsylvania and central North Carolina. The highest mean return period (i.e., minimum frequency) for heavy rainfall events was found over the western slopes of the Appalachians, especially in northwest Pennsylvania and eastern Tennessee and Kentucky. Since the majority of TCs tracked east of the Appalachians, low-level easterly flow ahead of the TCs generally favored orographic enhancement (reduction) of precipitation on the eastern (western) side of the Appalachians.

1.6 Distribution of Precipitation accompanying Landfalling and Transitioning TCs

This section relates the relevant dynamics discussed earlier in the chapter to both the synoptic and mesoscale distribution of rainfall accompanying landfalling and transitioning TCs. Precipitation asymmetries become more apparent as the TC advances into the midlatitudes at the onset of ET. Heavy precipitation often expands poleward of the TC center at the start of ET in association with upper-level outflow from the TC (Bosart and Dean 1991; Harr and Elsberry 2000; Atallah and Bosart 2003). Also, a shift in precipitation distribution to the left of the TC track often occurs during ET as the TC interacts with a lower-tropospheric baroclinic zone and an upstream trough (Harr and Elsberry 2000; Atallah and Bosart 2003; Atallah et al. 2007).

The precipitation distribution for a TC prior to the onset of ET is generally symmetric, although asymmetries due to storm motion have been documented in the literature (e.g., Marks 1985; Rodgers et al. 1994; Lonfat et al. 2004). For example, Marks (1985) examined the precipitation structure in Hurricane Allen (1980) and observed two distinct patterns: 1) spiral rainbands surrounding the eyewall, and 2) a narrow ring containing the heaviest rain inside the eyewall. Asymmetries in precipitation accompanying Allen were noted with relatively heavy rainfall on its front and right quadrants. These asymmetries were attributed to boundary-layer convergence (Shapiro 1983).

Chen et al. (2006) determined that two of the most important factors for determining precipitation asymmetries accompanying TCs are 850–200-hPa environmental vertical wind shear and storm motion. The environmental vertical wind shear was a dominant factor for determining rainfall asymmetry when the shear was greater than 7.5 m s^{-1}, with the greatest rainfall asymmetry found in the left downshear region of the TC (Figs. 1.8a,b). The storm motion became a leading factor for determining rainfall asymmetry when the shear was less than 5 m s^{-1}, with the greatest rainfall asymmetry found in the upshear region of the TC (Figs. 1.8c–f).

The locations of heavy precipitation associated with Agnes (1972) over the northeast U.S. were documented by Bosart and Carr (1978) and Carr and Bosart (1978). In particular, Bosart and Carr (1978) illustrated two preferred regions of possible heavy precipitation accompanying a landfalling and/or transitioning TC (Fig. 1.9). Region A is located to the northeast of an advancing TC in an area characterized by confluent flow downstream of an approaching midlatitude trough. The potential for flooding increases when heavy rainfall that is directly related to the TC (region B) tracks over the same areas previously affected by heavy rainfall from region A.

Atallah et al. (2007) studied the distribution of precipitation accompanying U.S. landfalling and/or transitioning TCs by comparing cases associated with a preferential left-of-track (LOT) precipitation distribution with those associated with a preferential right-of-track (ROT) precipitation distribution. The interaction between the TC and an upstream midlatitude trough (downstream ridge) was associated with the LOT (ROT) precipitation distribution composite shown in Fig. 1.10a (Fig. 1.10b). Tropical cyclone-induced diabatic ridge development downstream of the storm led to a significant increase of positive low-level thermal and upper-level PV advections in both composites. A LOT precipitation distribution was related to TCs undergoing ET. A reorientation of the upper-level trough from a positive to a negative tilt repositioned the heaviest rainfall to the northwest of the TC in the LOT precipitation distribution composite.

DeLuca (2004) and Srock (2005) examined heavy precipitation associated with TCs over the northeast and southeast U.S., respectively. The conceptual models produced in both studies illustrate the key dynamical ingredients for heavy precipitation events accompanying landfalling and/or transitioning TCs over the northeast U.S. (Fig. 1.11a) and landfalling TCs over the southeast U.S. (Fig. 1.11b). Enhanced upper-level divergence in the equatorward jet-entrance region, a coastal front, and heavy precipitation located to north of an advancing TC were present in both studies. DeLuca (2004) documented the presence of a cyclonically curved low-level jet on the eastern and northern side of the TC, which acted to transport tropical moisture into regions of the northeast U.S. Srock (2005) noted a cold-air damming setup east of the southern Appalachians and north of the advancing TC. The cold-air damming in the southeast U.S. helped strengthen the low-level thermal gradient over the coastal front.

1.7 Goals and Organization of the Thesis

The purpose of this thesis is to identify and document the primary synoptic-scale and mesoscale mechanisms responsible for heavy precipitation that routinely accompany landfalling and transitioning TCs in the northeast U.S. Three representative storms were selected for further study in order to highlight the different dynamical mechanisms involved in two LOT cases and a ROT case. Upon completion of this Collaborative Science Technology and Applied Research (CSTAR) study, it is anticipated that successful integration and communication of the results through effective technology transfer will assist National Weather Service (NWS) operational forecasters during similar weather events in future situations.

Chapter 2 will discuss the data sources and methodologies implemented in the construction of a 52-storm dataset and the selection of the three cases studied in further detail. Chapter 3 will present a brief climatology of landfalling and transitioning TCs and results from each of the three cases. Chapter 4 will discuss, compare, and contrast the results found in the case studies. Finally, chapter 5 will offer conclusions and suggestions for future research.

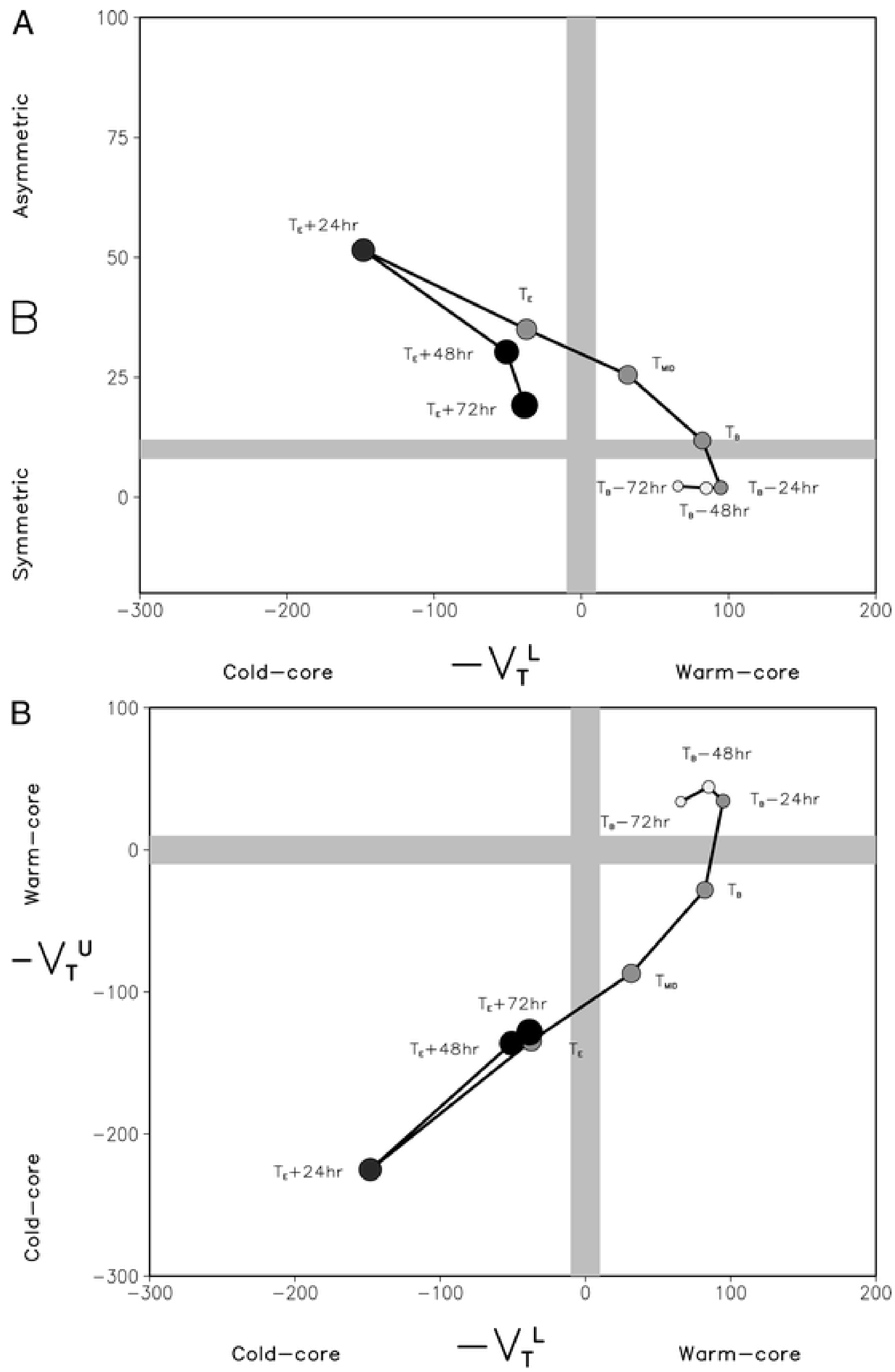

Fig. 1.1. A CPS composite consisting of 34 TCs that underwent ET over the North Atlantic for 1998–2003: (a) B (storm-motion-relative thermal asymmetry) versus $-V^{L}_{T}$ (900–600 hPa thermal wind) and (b) $-V^{U}_{T}$ (600–300 hPa thermal wind) versus $-V^{L}_{T}$ (900–600 hPa thermal wind). From Hart et al. (2006).

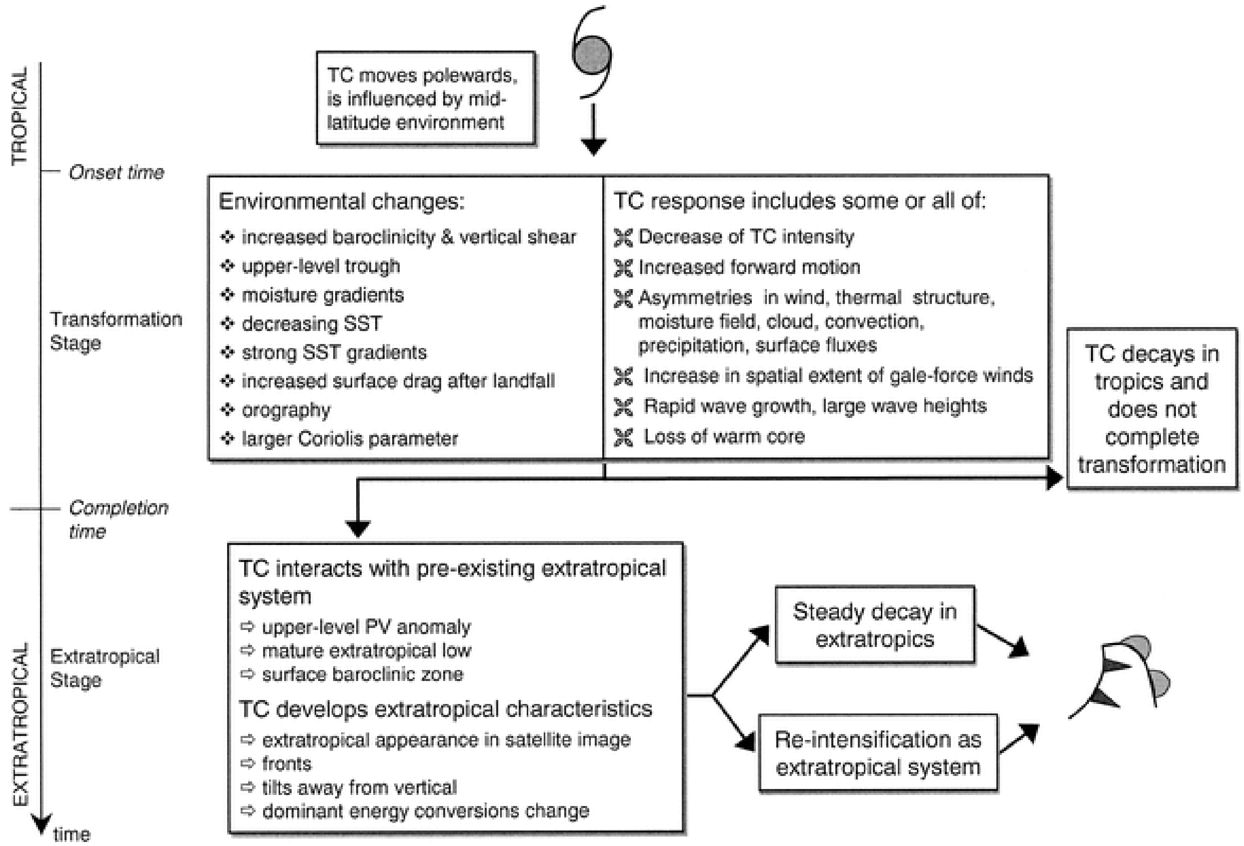

Fig. 1.2. A flow chart classifying the important processes during ET, starting with the poleward movement of the TC. From Jones et al. (2003).

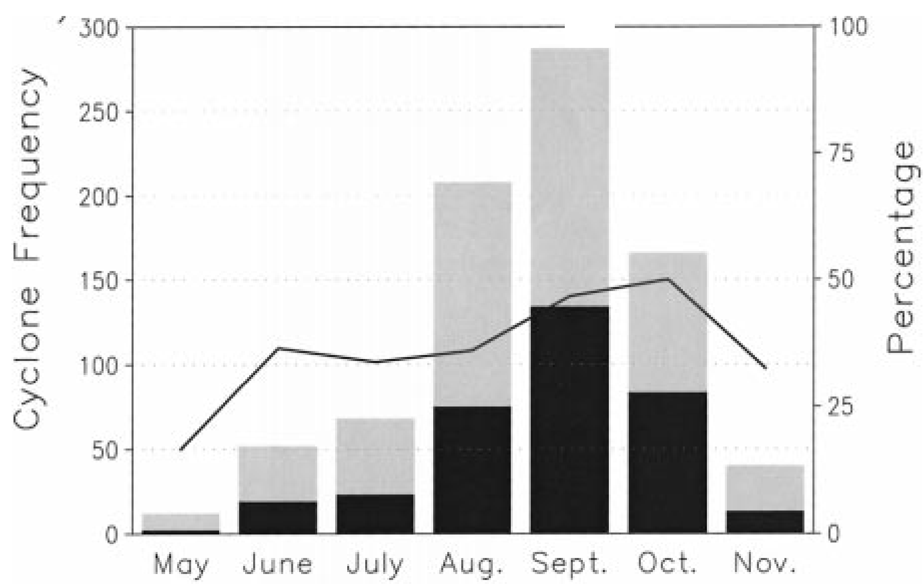

Fig. 1.3. Monthly frequency of Atlantic basin TCs (lighter shading) and TCs that experience ET (darker shading) for 1899–1996. From Hart and Evans (2001).

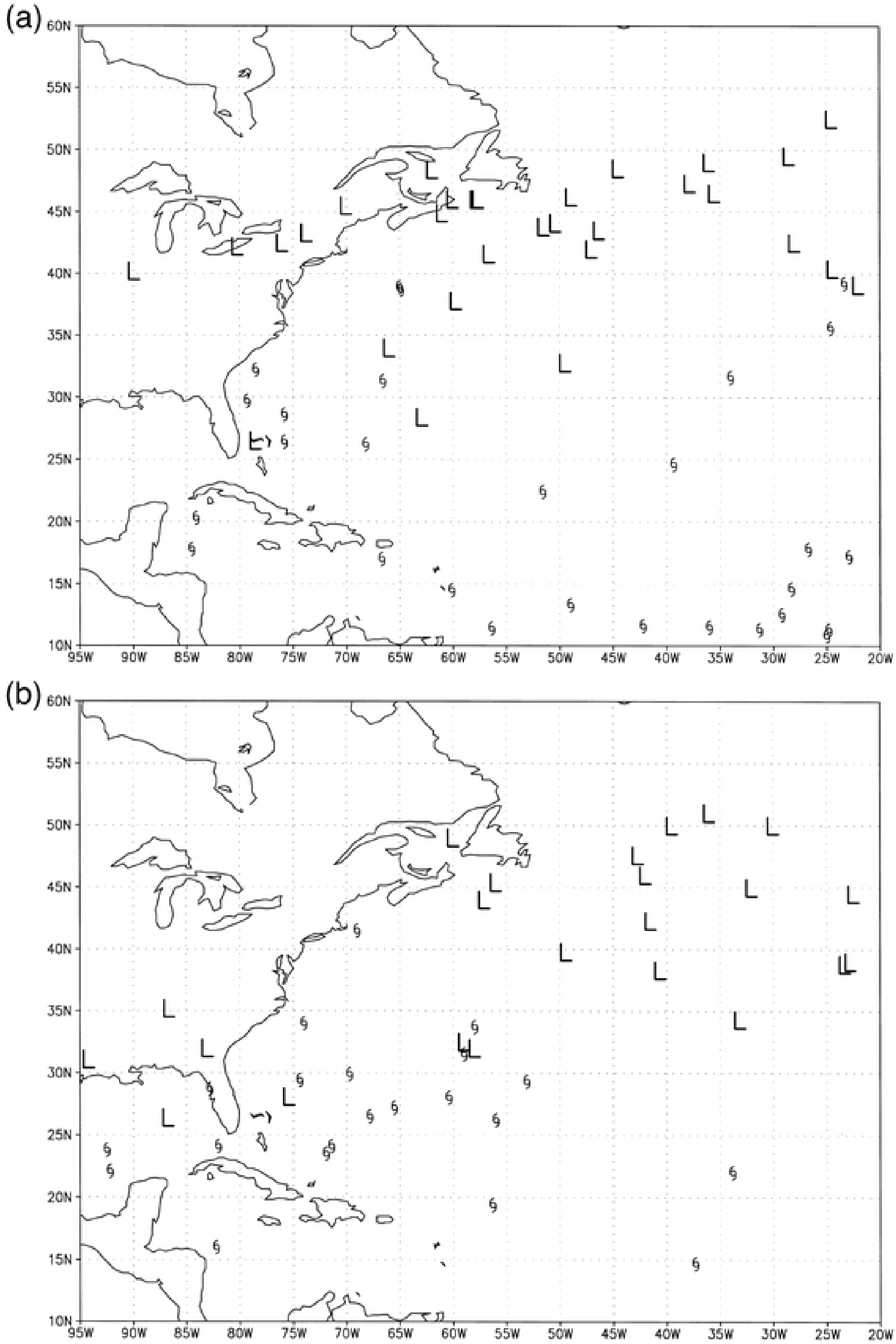

Fig. 1.4. Locations of TC formation (§) and ET onset (L) in the Atlantic basin for 1979–1993: (a) storms intensifying after ET concludes and (b) storms decaying after ET concludes. From Hart and Evans (2001).

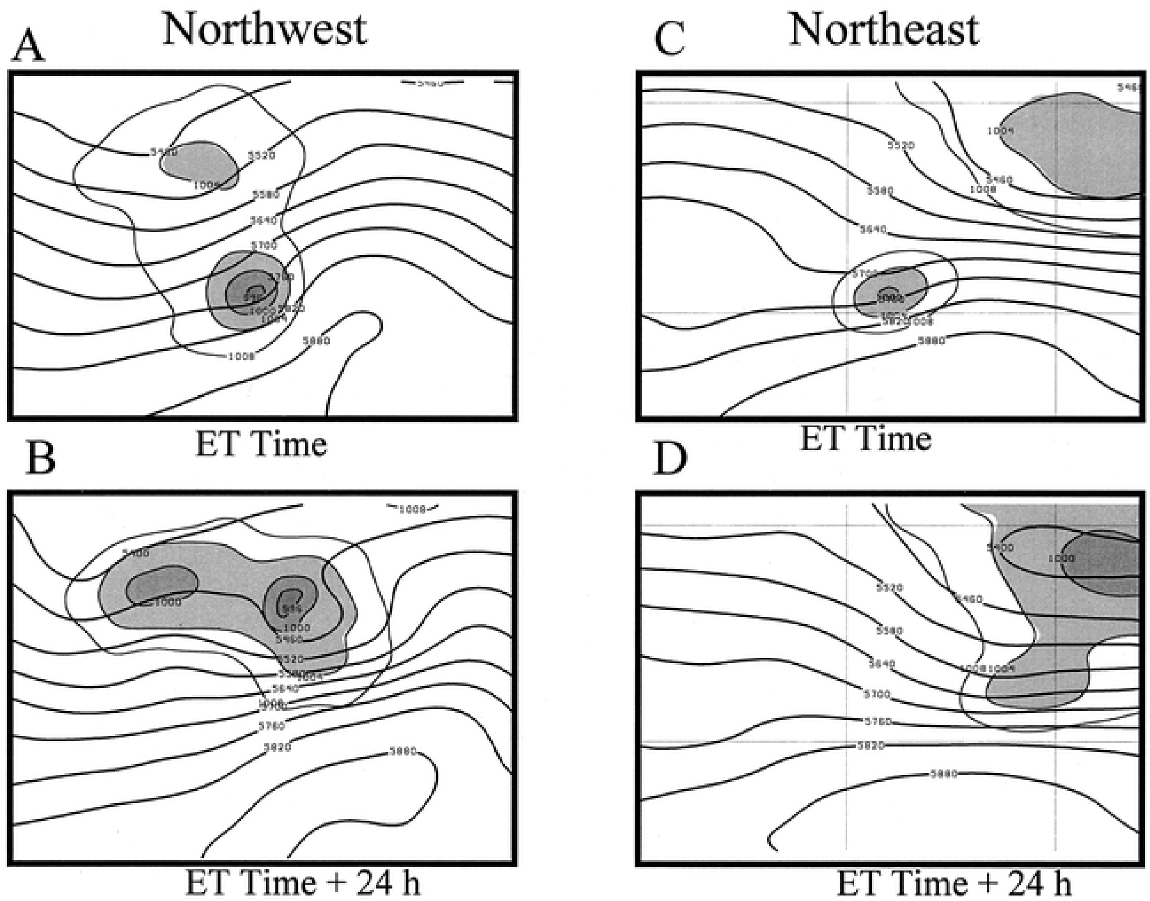

Fig. 1.5. A 17-case composite of 500 hPa geopotential height (m) and sea level pressure (shaded) in a northwest pattern corresponding to (a) onset of ET, (b) 24 h after onset of ET, and in a northeast pattern corresponding to (c) onset of ET and (d) 24 h after onset of ET. From Harr et al. (2000).

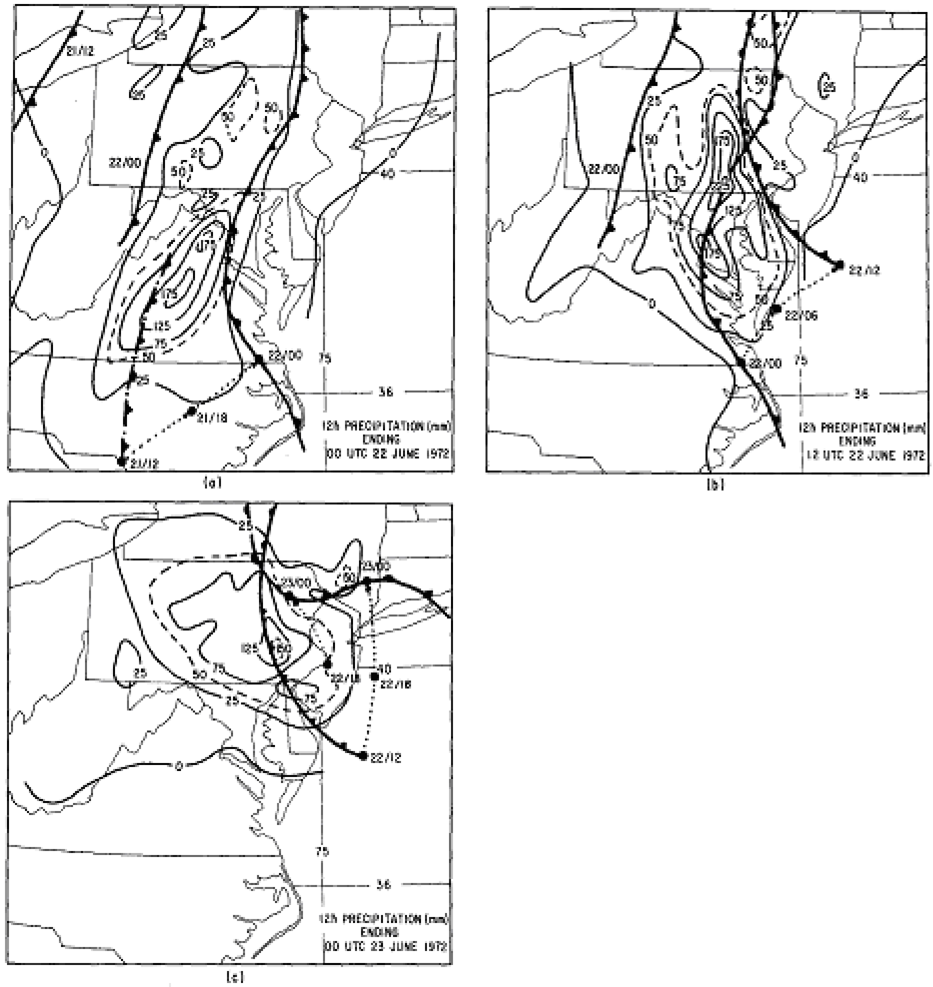

Fig. 1.6. 12-h precipitation totals (mm) showing mesoscale precipitation structures associated with Agnes: (a) 12-h period ending 0000 UTC 22 June 1972, (b) 12-h period ending 1200 UTC 22 June 1972, and (c) 12-h period ending 0000 UTC 23 June 1972. From Bosart and Dean (1991).

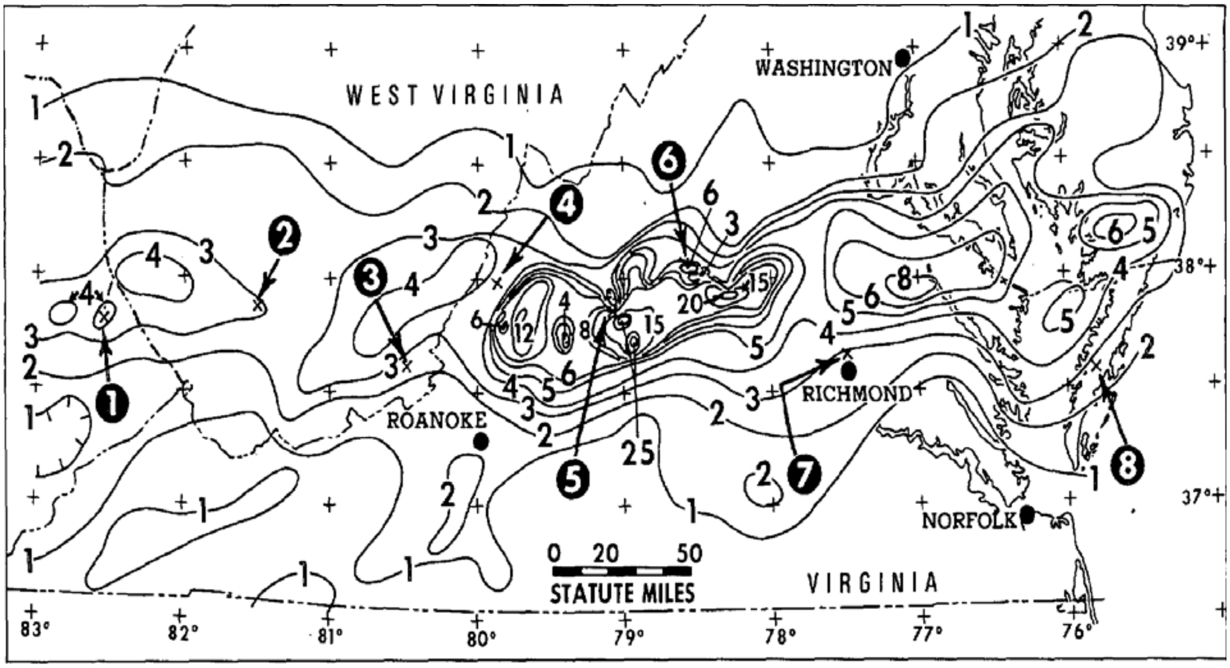

Fig. 1.7. 36-h precipitation totals (in.) associated with Camille (1969) ending 1800 UTC 20 August 1969. From Schwarz (1970).

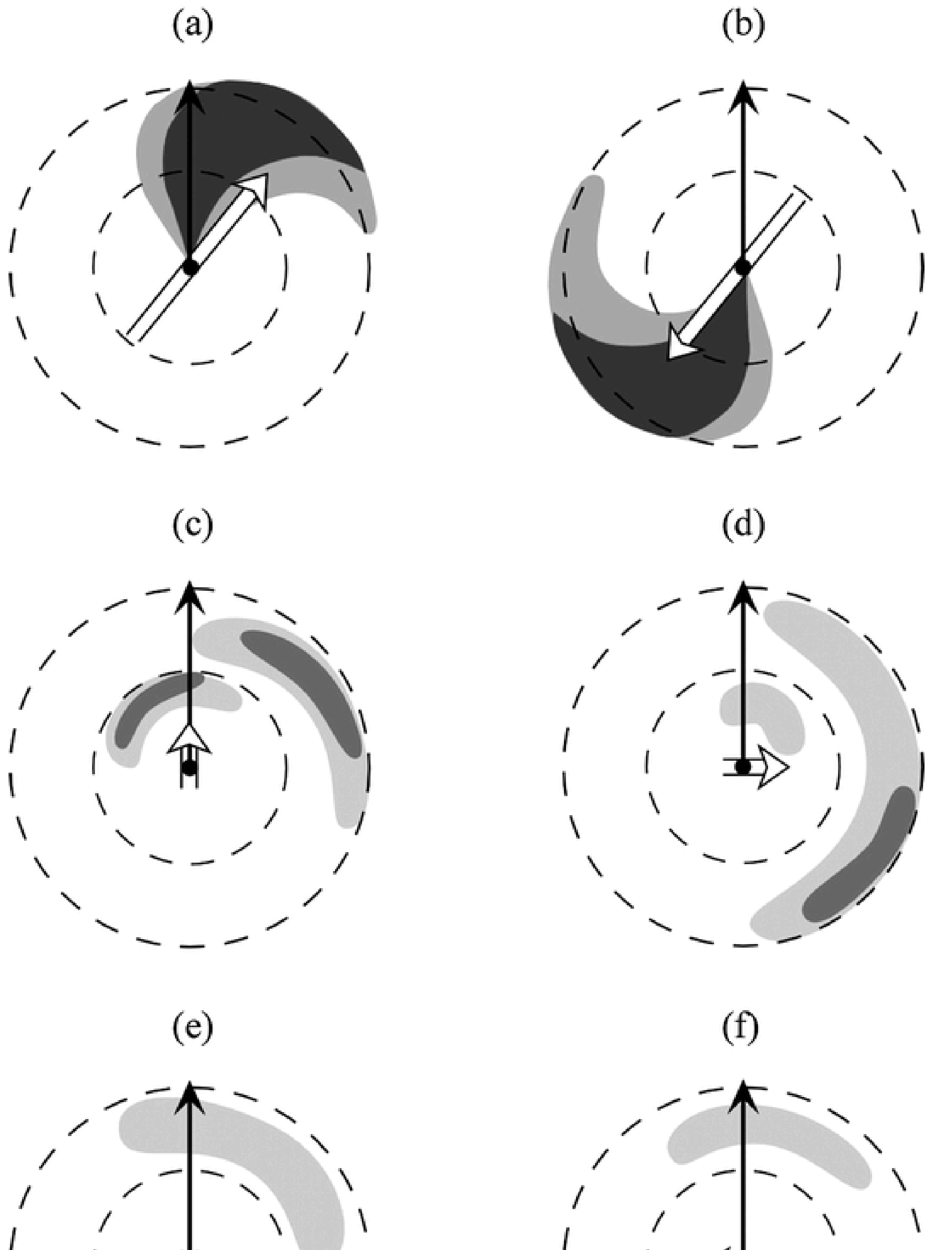

Fig. 1.8. Schematics showing TC rainfall asymmetry (gray shading with the largest rainfall asymmetry represented by the darkest shading) with respect to vertical wind shear (white arrow) and TC motion (black arrow): (a), (b) in a relatively strong shear environment and (c)–(f) in a relatively weak shear environment. From Chen et al. (2006).

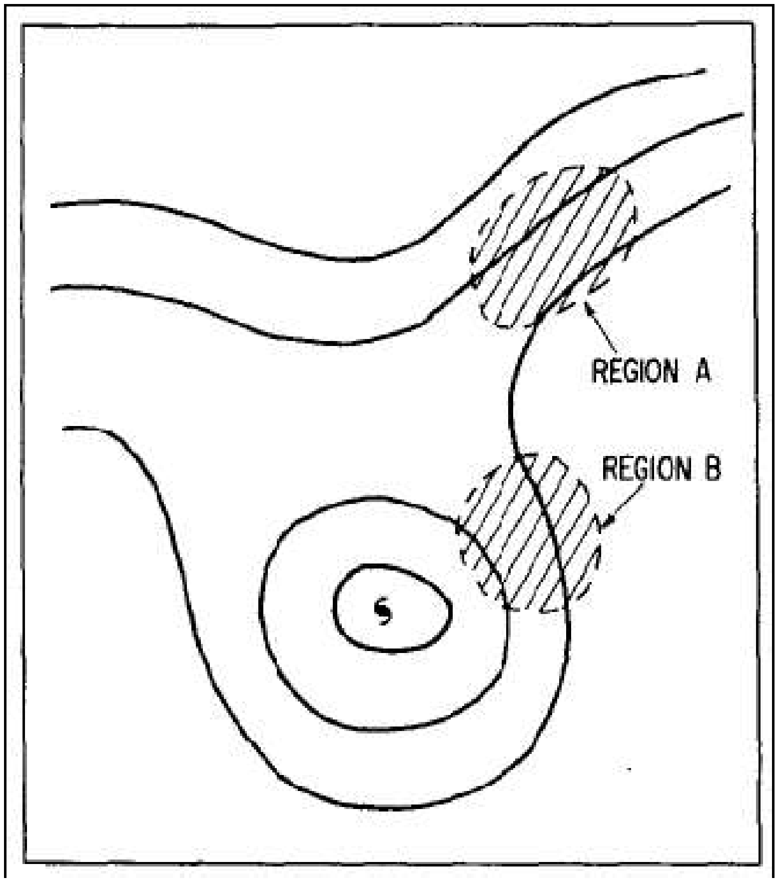

Fig. 1.9. Schematic of midtropospheric streamlines illustrating two regions of possible heavy precipitation accompanying a landfalling and/or transitioning TC. From Bosart and Carr (1978).

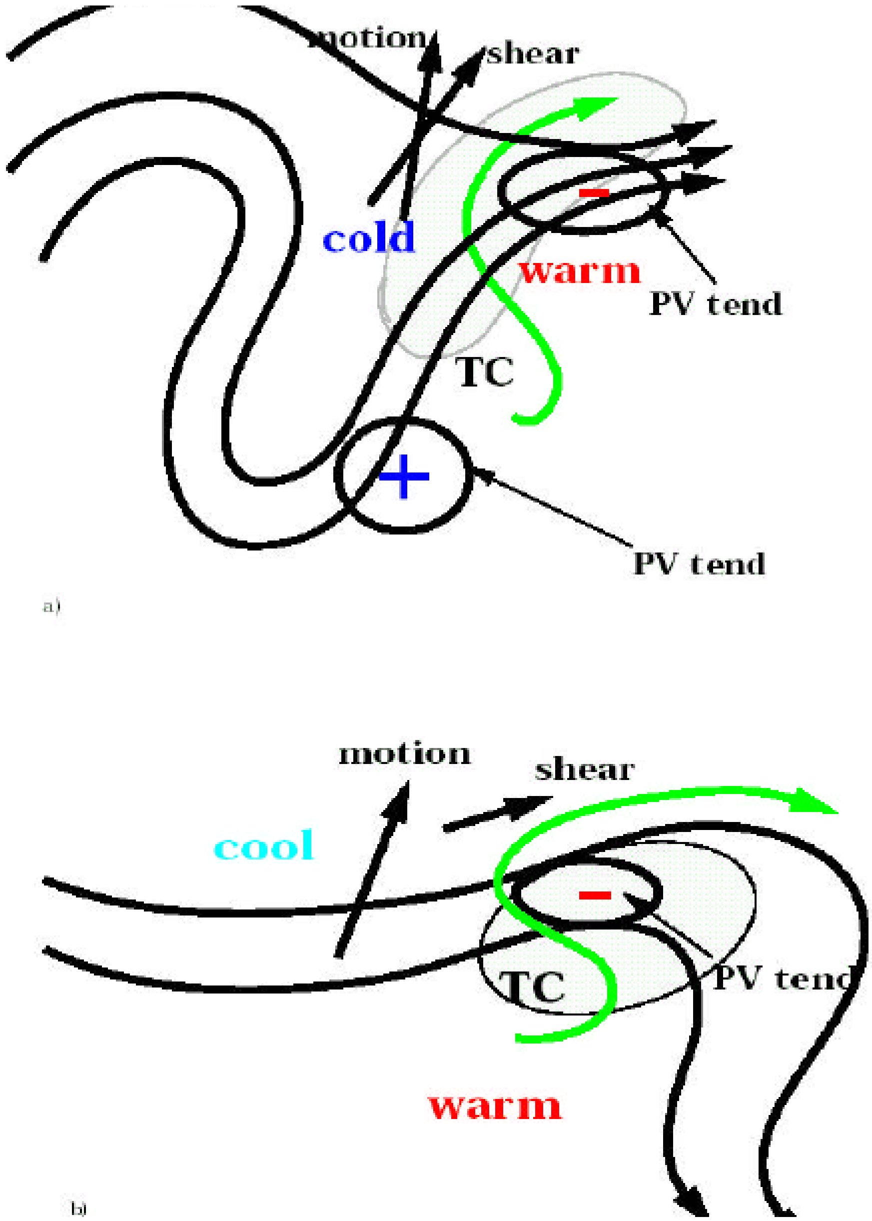

Fig. 1.10. Schematics of landfalling and transitioning TCs in the U.S. for (a) a LOT precipitation distribution composite and (b) a ROT precipitation distribution composite. From Atallah et al. (2007).

a)

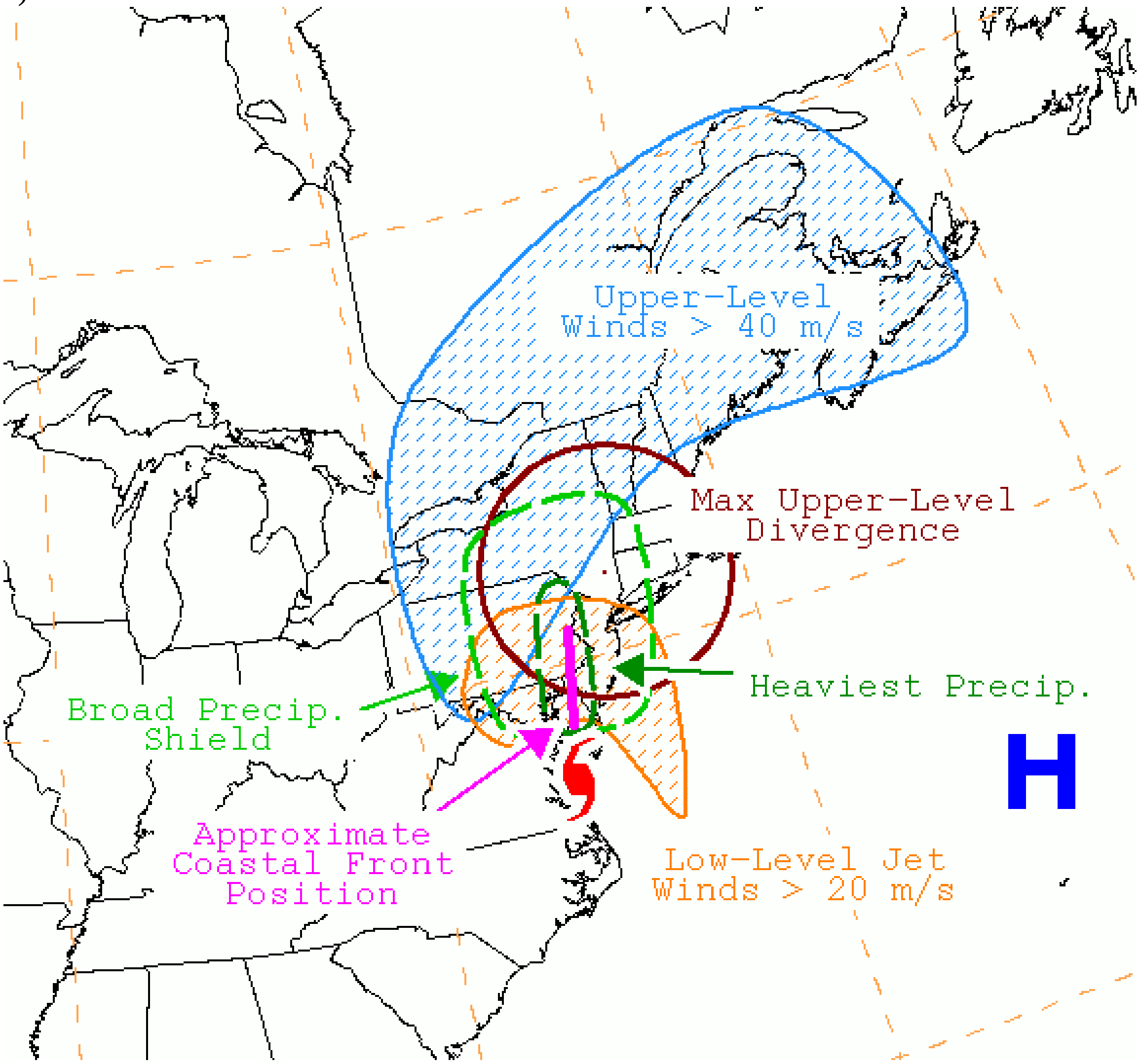

Fig. 1.11. Ingredients-based conceptual models for areas of heaviest rainfall associated with U.S. landfalling and transitioning TCs for the (a) northeast U.S. (DeLuca 2004) and (b) southeast U.S. (Srock 2005).

b)

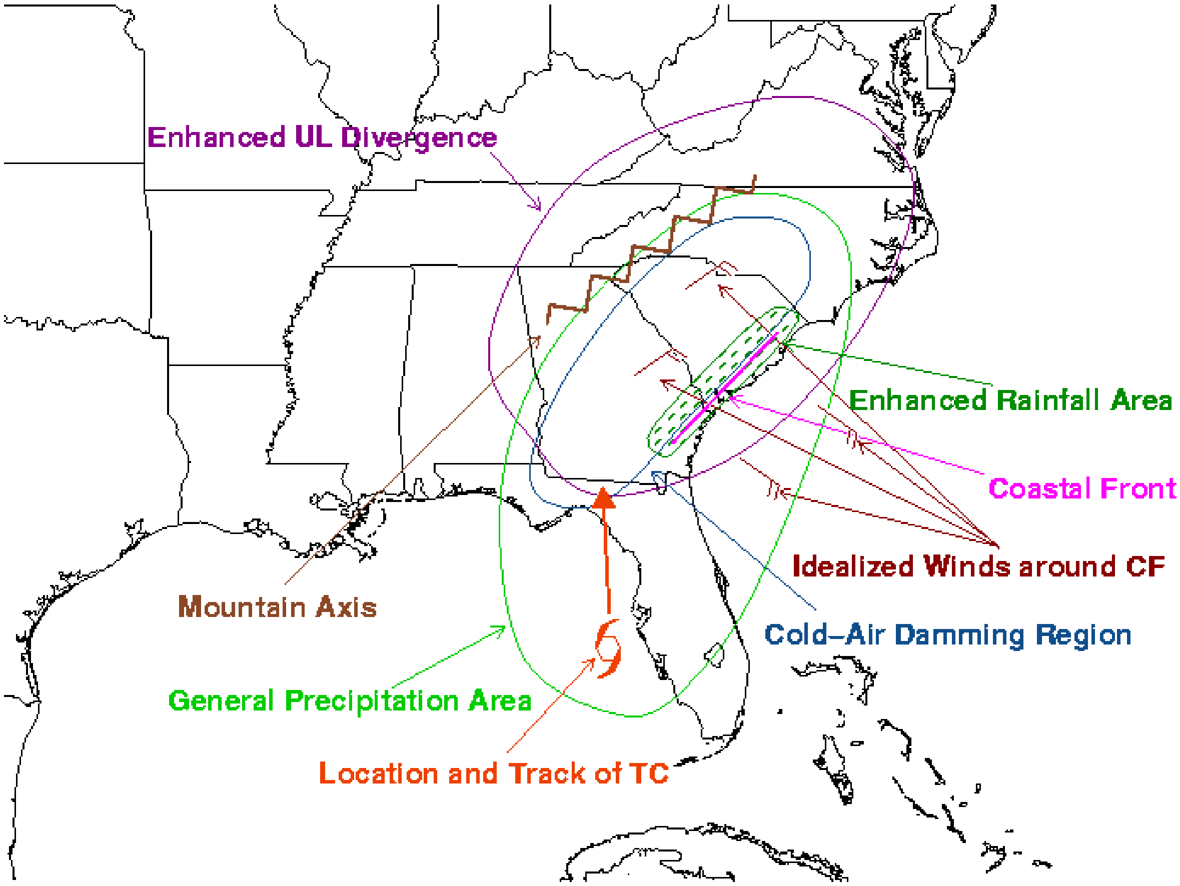

Fig. 1.11. *continued*.

2. Data and Methodology

2.1 Data Sources

Multiple data sources were used to investigate the synoptic and mesoscale dynamics associated with landfalling and transitioning TCs. Various datasets were also utilized to examine the large-scale distribution of rainfall and identify embedded mesoscale precipitation structures accompanying the TCs. The General Meteorology Package (GEMPAK; desJardins et al. 1991) was used for computation of selected diagnostics and display of the gridded datasets.

For the climatology study, synoptic analyses were performed using the 6-h National Centers for Environmental Prediction–National Center for Atmospheric Research (NCEP–NCAR) reanalysis dataset (Kalnay et al. 1996; Kistler et al. 2001). The coarse (2.5° × 2.5°) resolution of the NCEP–NCAR dataset was inadequate for mesoscale analyses. However, the dataset was adequate for the climatology study because it provides a comprehensive reanalysis back to 1948 and is consistently updated every few months.

The NCEP Global Forecast System (GFS; Kalnay et al. 1990; Kanamitsu et al. 1991) dataset (available at http://nomads.ncdc.noaa.gov/data.php for 2002–present) was employed for the case study analyses. After 2003, the 6-h GFS data were available on a global domain with 1° × 1° horizontal resolution and 64 vertical levels. The 1° × 1° resolution GFS dataset was used to investigate both synoptic and mesoscale processes associated with heavy precipitation for the three selected case studies discussed later in the chapter.

Precipitation data were obtained from multiple sources. The NCEP Unified Precipitation Dataset (UPD; available for 1948–2002) and Daily Precipitation Analysis dataset (DPA; available for 1996–present) (Higgins et al. 2000) were used for daily and storm-total precipitation analyses. Both datasets (available at http://www.cpc.ncep.noaa.gov/products/precip/realtime/GIS/retro.shtm) consist of quality-controlled daily (1200–1200 UTC) precipitation observations from sources including the Climate Prediction Center (CPC) precipitation data and National Climatic Data Center (NCDC) daily cooperative observer stations. An underestimation of maximum TC rainfall by the UPD was observed in the present study and previous studies (e.g., DeLuca 2004; Atallah et al. 2007). The relatively coarse (0.25° × 0.25°) resolution of the UPD and DPA datasets was inadequate for mesoscale precipitation substructures. Therefore, the high-resolution (10-km grid spacing) NWS River Forecast Center (RFC) quantitative precipitation estimate (QPE) dataset (available at http://www.hpc.ncep.noaa.gov/npvu/archive/rfc.shtml) was obtained from the National Precipitation Verification Unit (NPVU) to construct finer-scale precipitation analyses. The RFC QPE data are derived from a multisensor stage III analysis incorporating rain gauge and radar-estimated precipitation measurements for 2001–present.

The National Hurricane Center (NHC) best track dataset (available at http://www.nhc.noaa.gov/pastall.shtml) was used to identify TC tracks. The best track dataset contains information including 6-h (0000, 0600, 1200 and 1800 UTC) TC positions for 1851–present. The best track dataset is restricted to storms that are tropical in nature and therefore does not apply to TCs after the onset of ET.

Additional datasets were employed for surface and radar analyses. Surface data were obtained from hourly surface observations archived at the University at Albany, State University of New York. The WSI Corporation radar data were acquired from the University Corporation for Atmospheric Research (UCAR, available at http://locust.mmm.ucar.edu/). This dataset contains national reflectivity composites from the NWS Weather Surveillance Radar-1988 Doppler (WSR-88D) and is available for 1996–present.

2.2 Methodology

2.2.1 Compilation of a Dataset containing 52 TCs

A preliminary dataset consisting of 67 landfalling and transitioning TCs producing at least 100 mm of rainfall over the northeast U.S. from 1950 through 2006 was provided by David Vallee of the NWS Northeast River Forecast Center (NERFC) in Taunton, Massachusetts. A comprehensive examination of the preliminary dataset was performed to verify that each TC met the minimum 100-mm storm-total rainfall criterion. The 67-storm dataset was subsequently condensed to 52 storms following the verification of storm-total rainfall for each case. The maximum accumulated rainfall and dates of each TC event, also provided by David Vallee, were verified by reference to: 1) a prior dataset of 41 TCs (1950–2001) that produced greater than 100 mm of rain in the northeast U.S. (DeLuca 2004), 2) NCEP Hydrometeorological Prediction Center (HPC) storm-total precipitation analyses for TCs (1976–present) by David Roth, and 3) NWS NERFC storm-total precipitation analyses for TCs (1950–2002) by Ron Horwood.

2.2.2 Climatology Methodology

A climatology based on the 52-storm dataset was constructed to generate statistics by month, decade and precipitation distribution versus TC track, and to document dynamical processes common to the TCs. Storm-total precipitation (UPD and DPA data) and TC track (NHC best track data) were analyzed to determine the precipitation distribution for each storm. A finer-scale precipitation examination of the 16 most recent storms from 2001 to 2006 was performed to identify mesoscale structures of enhanced rainfall and preferred regions of possible orographic precipitation enhancement via analyses constructed from the RFC QPE dataset.

For the climatology, an upper-air examination using the NCEP–NCAR reanalysis dataset was performed to identify the dynamical mechanisms responsible for heavy precipitation accompanying the TCs. In particular, analyses at 925 and 850 hPa were used to resolve low-level jet structures, baroclinic zones, and thermal advection patterns. Analyses at 700 hPa and 500 hPa were used, respectively, to diagnose ascent and midlevel vorticity advection patterns. Analyses at 300 hPa were used to depict upper-level jet structures and divergence patterns.

2.2.3 Case Study Methodology

A comprehensive examination was conducted for the three selected cases: Ivan (2004), Jeanne (2004), and Ernesto (2006). Each case featured distinct precipitation distributions and embedded mesoscale precipitation structures as revealed by the RFC QPE data. Spatial and temporal patterns of TC rainfall were determined from WSI radar reflectivity analyses, while atmospheric moisture patterns were diagnosed through precipitable water analyses. Q and F vector diagnostics were constructed to isolate key synoptic and mesoscale forcings for vertical motion accompanying the TCs. The remainder of this chapter will discuss the Q and F vector methodology implemented in the case studies.

2.2.4 Upper-air Q Vector Diagnostics

Q vector diagnostics were utilized in each case study to determine where QG forcing for ascent could provide a favorable environment for heavy rainfall. The Q vector, which was used to examine the low-level horizontal and vertical ageostrophic motion, is defined as

$$\mathbf{Q} = -\left(\frac{\partial \mathbf{V}_g}{\partial x} \bullet \nabla\theta\right)\hat{\mathbf{i}} - \left(\frac{\partial \mathbf{V}_g}{\partial y} \bullet \nabla\theta\right)\hat{\mathbf{j}}, \tag{1}$$

where $\nabla\theta$ is the horizontal potential temperature gradient on a pressure surface and $\mathbf{V}_g$ is the geostrophic wind. In this study, the divergence of the Q vector ($\nabla \bullet \mathbf{Q}$) was calculated on pressure surfaces to identify patterns of QG forcing for vertical motion. Quasigeostrophic forcing for descent (ascent) was diagnosed in terms of the divergence (convergence) of the Q vector through the relationship expressed in the adiabatic, frictionless form of the QG omega equation in pressure coordinates [e.g., Keyser et al. (1992), Eq. (2.1)].

A natural ($\hat{\mathbf{s}}, \hat{\mathbf{n}}$) coordinate partitioning of the Q vector into along-isentrope (Q_s) and cross-isentrope (Q_n) components (Fig. 2.1) was implemented to help distinguish the respective dynamical forcings for vertical motion of each component. In this local coordinate system, $\hat{\mathbf{n}}$ is the cross-isentrope unit vector that points toward cold air and $\hat{\mathbf{s}}$

is the along-isentrope unit vector that lies 90° clockwise from $\hat{\mathbf{n}}$ (i.e., $\hat{\mathbf{n}} = -|\nabla\theta|^{-1}\nabla\theta$ and $\hat{\mathbf{s}} = \hat{\mathbf{n}} \times \hat{\mathbf{k}}$). The Q_s and Q_n components of the Q vector are defined, respectively, as

$$\mathbf{Q_s} = \left(\frac{\mathbf{Q} \bullet (\hat{\mathbf{k}} \times \nabla\theta)}{|\nabla\theta|^2}\right)(\hat{\mathbf{k}} \times \nabla\theta) \quad \text{or} \quad \mathbf{Q_s} = \left(\frac{\mathbf{Q} \bullet (\hat{\mathbf{k}} \times \nabla\theta)}{|\nabla\theta|}\right)\hat{\mathbf{s}}, \tag{2}$$

and

$$\mathbf{Q_n} = \left(\frac{\mathbf{Q} \bullet \nabla\theta}{|\nabla\theta|^2}\right)\nabla\theta \quad \text{or} \quad \mathbf{Q_n} = -\left(\frac{\mathbf{Q} \bullet \nabla\theta}{|\nabla\theta|}\right)\hat{\mathbf{n}}. \tag{3}$$

For the three selected cases, Q_s diagnostics were used for a synoptic-scale examination of QG forcing for vertical motion in relation to TC–thermal trough and ridge interactions, while Q_n diagnostics were used for a mesoscale examination of QG forcing for vertical motion in relation to frontogenesis patterns.

The aforementioned 1° × 1° GFS dataset was used to compute the Q, Q_n, and Q_s vectors and associated divergence fields on pressure surfaces from 1000 to 900 hPa at 25 hPa-intervals and from 900 to 200 hPa at 50-hPa intervals for the three selected cases. Although Q vector plots were constructed at several pressure levels, only 925- and 300-hPa plots will be shown to illustrate lower- and upper-tropospheric structures. A nine-point smoother was applied to the potential temperature and geostrophic wind fields for the Q vector calculations in order to lessen the noise found in the high-resolution 1° × 1° GFS dataset. Also, a Gaussian filter with a weight of 10 (4) was used for smoothing the Q vectors (divergence of Q vectors). The aforementioned smoothing techniques did not appear to significantly smooth out the small-scale structures found in the Q vector diagnostics.

2.2.5 Surface and Cross-Sectional F Vector Diagnostics

A Barnes objective analysis (Barnes 1964) was performed with GEMPAK to interpolate the archived surface observations onto a grid with 0.6° spacing. The 0.6° gridded dataset was utilized for calculations of F vectors (Keyser et al. 1988) at the surface by using the total horizontal wind form of (1):

$$\mathbf{F} = -\left(\frac{\partial \mathbf{V}}{\partial x} \bullet \nabla\theta\right)\hat{\mathbf{i}} - \left(\frac{\partial \mathbf{V}}{\partial y} \bullet \nabla\theta\right)\hat{\mathbf{j}}. \tag{4}$$

The F vectors were then partitioned into $\hat{\mathbf{s}}$ and $\hat{\mathbf{n}}$ components by substituting F for Q in (2) and (3). Surface diagnostics included the cross-isentrope component of the F vector, F_n, to determine patterns of frontogenesis and the divergence of the F_n vector ($\nabla \bullet \mathbf{F_n}$) to identify structures of mesoscale forcing for vertical motion along and within surface frontal zones. The smoothing techniques performed on F vectors were identical to those used for Q vectors.

Cross sections were constructed using the 1° × 1° GFS dataset to examine the vertical structure of a warm-frontal boundary that was found in each case. The cross sections were taken quasi-parallel to the 925–500-hPa layer-averaged potential temperature gradient. Analyses of the magnitude of the F_n vector (i.e., two-dimensional frontogenesis), relative humidity, potential temperature, upward vertical velocity, and wind were used to reveal the vertical structure across the frontal boundary.

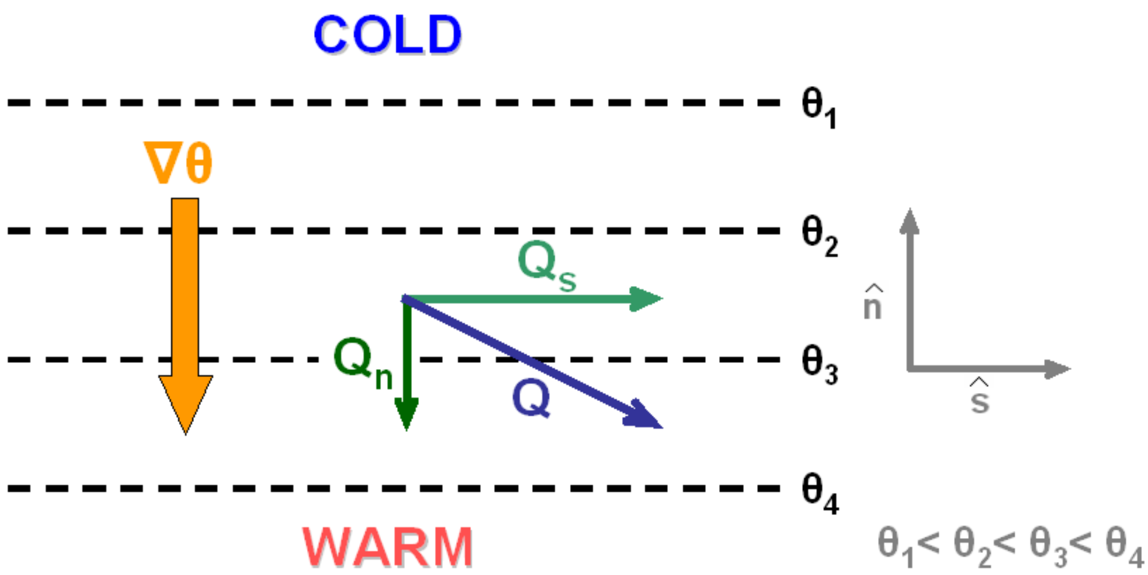

Fig. 2.1. Schematic illustrating the natural ($\hat{\mathbf{s}},\hat{\mathbf{n}}$) coordinate partitioning of the Q vector into along-isentrope (Q_s) and cross-isentrope (Q_n) components. Dashed lines are isentropes on a pressure surface and the thick arrow represents the potential temperature gradient vector. Adapted from Martin (1999).

3. Results

Section 3.1 of this chapter will document the results from the climatology study. Section 3.2 will present the results from the case studies of Ivan (2004), Jeanne (2004), and Ernesto (2006). Each case study will be divided into the following subsections: overview and storm-total precipitation versus TC track analysis; upper-air analysis; vertical cross-section analysis; and mesoscale precipitation and surface analysis.

3.1 A 52-TC Climatology

The dataset of 52 landfalling and transitioning TCs that produced at least 100 mm of rainfall over the northeast U.S. for 1950–2006 is shown in Table I. Table I includes the year, date, and maximum storm-total rainfall for all 52 cases. On average, approximately one TC per year affects the northeastern U.S. with ≥ 100 mm of rainfall.

Climatology statistics from the 52-TC dataset are presented as a function of decade in Fig. 3.1a. The present decade (2000–2006), which contained 16 (31% of the 52) landfalling and transitioning TCs that impacted the northeast U.S. with at least 100 mm of rainfall, also contained the largest number of cases in any decade of this study. The majority (10/16) of the TC events in the 2000s occurred in 2004–2005 (see Table I). The 1950s was the second most active decade for these TC events with 14 (27% of the 52) TCs, while the 1980s was associated with the smallest number of TC events with only two (4% of the 52) TCs.

Climatology statistics from the 52-TC dataset are shown as a function of precipitation distribution versus TC track in Fig. 3.1b. A LOT precipitation distribution was associated with 39 TCs and was by far the most common precipitation distribution

(75% of the 52 TCs) accompanying these TC events. Only three (6% of the 52) cases exhibited a ROT precipitation distribution, while 10 (19% of the 52) TCs did not exhibit a preferential-precipitation distribution.

Climatology statistics from the 52-TC dataset are presented as a function of month in Fig. 3.1c. The majority of these TC events occurred in the months of August and September, with a total of 18 (35% of the 52) TCs identified in August and 22 (42% of the 52) TCs identified in September. During the months of June, July, and October, the TC events were not seen as often as in August and September, with only two (4% of the 52), six (12% of the 52), and four (8% of the 52) TCs occurring in these months, respectively.

The total accumulated precipitation and tracks from all 16 landfalling and transitioning TCs that occurred during 2001 to 2006 (see Table I) are presented in Fig. 3.2. This figure illustrates the recent impact of heavy rainfall from the 16 TCs in the northeastern U.S. Overall, the entire eastern U.S. that is situated east of 82°W has experienced significant hydrological impacts including rainfall amounts totaling at least 18 cm (excluding a small section in southern Maine) from all of the 16 TCs. Precipitation amounts >30 cm are generally found over the mid-Atlantic region and southern northeast U.S., while the mid-Atlantic corridor, from South Carolina northward through the Pennsylvania–New York border, is the region that is impacted the most by TC rainfall with >48 cm of precipitation. The rainfall maxima (>90 mm) found over eastern North Carolina and Virginia are located where the TCs tracked most frequently, while another local maximum of rainfall (78–84 cm) is apparent farther north over eastern Pennsylvania. Possible orographic precipitation enhancement is seen in western

North Carolina and northwestern Virginia, where several TCs tracked far enough inland so that low-level easterly flow ahead of the storm was upslope along the eastern slopes of the Appalachians. Although not as evident as in the abovementioned areas, possible orographic precipitation enhancement is also seen along the eastern slopes of the Poconos in northeast Pennsylvania, the Berkshires in western Massachusetts, and the Catskills in southeast New York. Conversely, relatively lower rainfall amounts are found along the western slopes of the Appalachians.

3.2 Case Studies

3.2.1 TC Ivan (2004)

3.2.1.1 Overview and Storm-Total Precipitation Analysis

Ivan was a Cape Verde TC that made U.S. landfall as a category 3 hurricane on the Saffir–Simpson scale near Gulf Shores, Alabama, early on 16 September 2004. Ivan then moved northeastward through Alabama on 17 September and into Virginia by 18 September (Fig. 3.3). Ivan underwent ET while interacting with a frontal boundary over the eastern U.S. and was classified as extratropical near the mid-Atlantic coast by 1800 UTC 18 September. In the U.S., Ivan was responsible for 25 deaths and over 14 billion dollars in damage (Franklin et al. 2006).

Analysis of storm-total precipitation versus TC track for 1200 UTC 16–1200 UTC 19 September shows that the heavy rainfall associated with Ivan occurred across parts of the eastern U.S. (Fig. 3.3). An initial along-track-precipitation distribution accompanying Ivan is found over the southeast U.S., with possible orographic enhancement of rainfall located over the upslope regions of the Blue Ridge Mountains in western North Carolina. A shift to a LOT precipitation distribution is evident over the northeastern U.S., with the heaviest precipitation located to the north of the TC track. The LOT precipitation distribution contains rainfall amounts of 100–160 mm within a band stretching from eastern Kentucky northeastward through most of Pennsylvania and into southern New York. In the northeastern U.S., the heaviest precipitation totals, exceeding 200 mm, are found over southern Pennsylvania.

3.2.1.2 Upper-Air Analysis

Analyses of 300-hPa geopotential height and wind speed are overlaid onto precipitable water analyses to show upper-level features (e.g., jet streaks, troughs, and ridges) and atmospheric moisture patterns. Shortly after Ivan makes landfall along the Alabama coast, a strong upper-level jet streak in the eastern U.S. and western Atlantic is positioned over the top of a broad upper-level (i.e., 300-hPa) ridge at 1200 UTC 16 September (Fig. 3.4). Another jet streak near the Great Lakes region is positioned along the base of a midlatitude trough that is located over the central U.S. and Canada, while an area of upper-level divergence from the TC-induced outflow is evident over the southeast U.S. A plume of precipitable water values >30 mm is situated downstream of the aforementioned midlatitude trough and over the eastern half of the U.S., with maximum precipitable water values >70 mm centered near the TC.

By 1200 UTC 17 September, modifications to the upper-level flow pattern have become evident as Ivan has moved into the Tennessee Valley (Fig. 3.5). The southeastward progressing trough has acquired a neutral tilt and has sharpened as Ivan becomes embedded in cyclonic flow. A region of confluent flow has developed poleward of Ivan between the southerly flow associated with the trough to the south and the main westerly flow to the north. Maximum winds within the southwest–northeast-oriented jet streak have increased from the previous 12-h analysis to 50 m s^{-1} over eastern Canada. A band of upper-level divergence located near Ohio has formed due to the juxtaposition of the divergence that is associated with the upper-level outflow from Ivan and the divergence that is typically found in the right entrance region of the upper-level jet. At this time, maximum precipitable water values >50 mm are situated along and to the east of Ivan.

As Ivan moves toward the mid-Atlantic coast, the upper-level jet streak located over eastern Canada continues to strengthen to 60 m s^{-1} by 0000 UTC 18 September (Fig. 3.6). Significant upper-level divergence is located in the equatorward entrance region of this jet streak. The precipitable water analysis at this time shows a moisture-laden environment situated over parts of the northeastern U.S.

Analyses containing equivalent potential temperature (θ_e) and wind at 925 hPa overlaid onto radar reflectivity analyses will be used to identify the structure of key low-level features (e.g., jets and θ_e trough–ridge axes) in relation to the precipitation field. At 1200 UTC 16 September, a relatively symmetric precipitation field is associated with Ivan as it is positioned far away from the midlatitude θ_e boundary that is located over the midwestern U.S. (Fig. 3.7).

The precipitation field associated with Ivan has become asymmetric by 1200 UTC 17 September, with precipitation extending northeastward along the midlatitude θ_e boundary that is located to the north of Ivan (Fig. 3.8). At this time, a cyclonically curved low-level (i.e., 925-hPa) jet with maximum wind speeds around 20 m s^{-1} is enhancing the northward transport of high θ_e air on the eastern side of Ivan.

By 0000 UTC 18 September, Ivan has become entrenched in the midlatitude θ_e boundary as it undergoes ET (Fig. 3.9). Heavy precipitation is found along a line of convection extending from eastern North Carolina to northern Virginia and is embedded within the low-level jet and θ_e-ridge axis. Another area of heavy precipitation is found over central Pennsylvania, where the nose of the low-level jet and θ_e-ridge axis on the eastern side of Ivan intersect the θ_e boundary. Maximum wind speeds around 25 m s^{-1} are identified in the low-level jet by 1200 UTC 18 September (Fig. 3.10), while southerly flow associated with this jet is highly confluent with the northerly flow on the cool side of the θ_e boundary.

Diagnostics of 925-hPa Q, Q_n, and Q_s vectors are presented in the remainder of this subsection to identify patterns of QG forcing for ascent corresponding to each respective divergence field. The 925-hPa Q vector analysis at 0000 UTC 17 September shows an area of QG forcing for ascent located just to the east of Ivan over northern Georgia (Fig. 3.11a). A midlatitude baroclinic zone (which is correlated to the aforementioned midlatitude θ_e boundary) over the Midwest is positioned far to the north of Ivan. Accordingly, there is negligible evidence for QG frontogenesis (i.e., Q_n vectors directed towards warmer air) and Q_n convergence near Ivan at this time (Fig. 3.11b). The Q vector convergence (Fig. 3.11a) is predominantly associated with the Q_s component (Fig. 3.11c). At 300 hPa, weak QG frontogenesis and Q_n convergence over the southern Midwest U.S. is evident as the upper-level outflow from Ivan interacts with a midlatitude baroclinic zone to the north and west of Ivan (Fig. 3.11d). The highest potential temperature air is centered over Ivan at both lower and upper levels, giving evidence that Ivan still has a tropospheric-deep warm-core structure.

By 1200 UTC 17 September, Ivan is accompanied by changes in the 925-hPa Q vector pattern (Fig. 3.12a). The strongest QG forcing for ascent is positioned northeastward of Ivan and near the heaviest precipitation at this time (see Fig. 3.8). The Q_n analysis provides evidence for the formation of a warm-frontal boundary on the northern side of Ivan as it interacts with the midlatitude baroclinic zone (Fig. 3.12b). The QG frontogenesis present along the warm-frontal boundary corresponds to a thermally direct transverse ageostrophic circulation with a band of Q_n divergence (convergence) positioned on the cool (warm) side of the boundary. Q_s divergence (convergence) is found within the thermal trough (ridge) immediately upshear (downshear) of Ivan (Fig. 3.12c). At 300 hPa, strong QG frontogenesis and a distinct banded Q_n divergence–convergence structure that is situated ahead of the thermal trough and to the northwest of Ivan (Fig. 3.12d), is revealed as a thermally direct transverse ageostrophic circulation in the entrance region of the upper-level jet (see Fig. 3.5). An apparent northwest tilt with height in the banded Q_n structure is seen in Figs. 3.12b,d.

The strongest QG forcing for ascent has shifted into the central mid-Atlantic region by 0000 UTC 18 September (Fig. 3.13a) and is in close proximity to the heaviest precipitation seen in Fig. 3.9. The Q_n divergence–convergence banded structure situated over the northern mid-Atlantic region has strengthened since the prior analysis (Fig. 3.13b). At this time, maximum frontogenesis values exceeding 4 K $(100\ \mathrm{km})^{-1}$ $(3\ \mathrm{h})^{-1}$ are found over central Pennsylvania (not shown). The Q_s divergence–convergence dipole pattern is located in the thermal trough–ridge with Q_s convergence over central

Pennsylvania (Fig. 3.13c). The 300-hPa Q_n divergence–convergence banded structure has progressed eastward ahead of thermal trough near the Great Lakes region (Fig. 3.13d).

By 1200 UTC 18 September, robust QG forcing for ascent has moved eastward, with maximum values located over the northern mid-Atlantic region (Fig. 3.14a). The Q vector pattern (Fig. 3.14a) is associated with contributions from both the Q_n (Fig. 3.14b) and Q_s (Fig. 3.14c) components. At this time, a band of strong frontogenesis >8 K (100 km)$^{-1}$ (3 h)$^{-1}$ (not shown) is found in between and parallel to the Q_n divergence–convergence band seen in Fig. 3.14b. The Q_s pattern accompanying Ivan has not only contributed to dynamical forcing for ascent over the eastern U.S., but it has contributed to a cyclonic rotation of the potential temperature gradient from the eastern side of the thermal trough to the western side of the thermal ridge (Figs. 3.13c, 3.14c, and 3.15c). The 300-hPa Q_n banded structure has progressed eastward, as the strongest QG frontogenesis is maintained from the interaction between the thermal trough over Canada and the TC-induced thermal ridge over the eastern U.S. (Fig. 3.14d).

3.2.1.3 Vertical Cross-Section Analysis

Cross sections presented in this subsection will examine the vertical structure of two-dimensional frontogenesis, relative humidity, potential temperature, upward vertical velocity, and wind across the warm-frontal boundary accompanying Ivan. The cross-sections are taken quasi-parallel to the 925–500-hPa layer-averaged potential temperature gradient (not shown) with warmer air oriented toward the right side of the cross section. The cross-section analyses shown at 1200 UTC 17 September (Fig. 3.15, orientation shown in Fig. 3.12b), 0000 UTC 18 September (Fig. 3.16, orientation shown in Fig. 3.13b), and 1200 UTC 18 September (Fig. 3.17, orientation shown in Fig. 3.14b) correspond to the times when the strongest 925–500-hPa layer-averaged frontogenesis (not shown) and heaviest precipitation occurred.

A tropospheric-deep pattern of frontogenesis tilting toward cooler air with height is illustrated in all three cross sections (Figs. 3.15–3.17). This area of frontogenesis is located in an environment with relative humidity values >90%. At 1200 UTC 17 September, weak frontogenesis [≤2.0 K $(100\ km)^{-1}$ $(3\ h)^{-1}$] is seen below 400 hPa while moderate frontogenesis [>2.5 K $(100\ km)^{-1}$ $(3\ h)^{-1}$] is seen at upper levels and near the 300-hPa jet streak (Fig. 3.15). An increasingly well-defined vertically tilted frontogenesis pattern is apparent by 0000 UTC 18 September with maximum frontogenesis values around 3.0 K $(100\ km)^{-1}$ $(3\ h)^{-1}$ near the surface and >4.5 K $(100\ km)^{-1}$ $(3\ h)^{-1}$ near 350 hPa (Fig. 3.16). By 1200 UTC 18 September, maximum frontogenesis values have increased to >7.0 K $(100\ km)^{-1}$ $(3\ h)^{-1}$ near the surface and 6.0 K $(100\ km)^{-1}$ $(3\ h)^{-1}$ around 300 hPa (Fig. 3.17). The strongest frontogenesis is found in the lower (below 800 hPa) and upper (in the 500–250-hPa layer) troposphere at 0000 and 1200 UTC 18 September (Figs. 3.16 and 3.17).

In all three cross sections, the ascent pattern tilts toward cooler air with height and is located on the warm side of the frontogenesis maximum (Figs. 3.15–3.17). The tilt toward cooler air with height seen in vertical ascent structure at 1200 UTC 17 September (Fig. 3.15) becomes more evident by 0000 UTC 18 September. Ascent is maximized in the midtroposphere above and on the warm side of the frontogenesis region (Figs. 3.15–3.17). The largest value of ascent ($\leq -32\ \mu b\ s^{-1}$) is observed at 1200 UTC 18 September and in the 600–500-hPa layer (Fig. 3.17). The low-level convergence that is indicated by $\partial\omega/\partial p > 0$ in the boundary layer provides support for enhanced lift over the frontal boundary.

The flow is confluent in the boundary layer, with southeasterly (northeasterly) winds found on the warm (cool) side of the frontal boundary (Figs. 3.15–3.17). The deep southerly flow associated with the circulation of Ivan is established above the boundary layer, and along and on the warm side of the frontal boundary. Warm (cold) air advection on the warm (cool) side of the boundary is implied by a veering (backing) of the winds with height and is producing frontogenesis along the frontal boundary.

3.2.1.4 Mesoscale Precipitation and Surface Analysis

Mesoscale precipitation structures are discussed in relation to 6-h surface F_n vector analyses during the time period of heaviest precipitation. Surface analyses include F_n vectors and associated divergence fields, potential temperature, and streamlines to illustrate the warm-frontal boundary accompanying Ivan.

The formation of the low-level warm-frontal boundary (see Fig. 3.12b) is coincident with the formation of the surface frontal boundary to the north of Ivan at 1200 UTC 17 September (Fig. 3.18a). At this time, frontogenesis, which is implied by the F_n vectors pointing toward the warmer air, becomes evident along the surface boundary near West Virginia. A weak southwest–northeast-oriented F_n divergence–convergence pattern that has a quasi-banded configuration is seen along this region of frontogenesis. By 1800 UTC 17 September, the surface boundary, which is positioned from eastern Kentucky to the West Virginia–Pennsylvania border, has become increasingly evident as implied by the tightening of the isentropes and the enhancement of the banded F_n divergence–convergence pattern (Fig. 3.18b). Surface streamlines reveal a confluent flow along the along the surface boundary, with northerly (southeasterly) flow found on the cool (warm) side of the boundary. This southeasterly flow, which is induced by the circulation of Ivan, is feeding tropical air from the Atlantic into the surface boundary. The heaviest 6-h precipitation ending 1800 UTC 17 September is found along and on the cool side of the surface boundary seen in Figs. 3.18a,b, with maximum rainfall amounts near 90 mm in eastern Ohio (Fig. 3.18c).

By 0000 UTC 18 September, the strong frontogenesis and banded F_n divergence–convergence pattern along the mesoscale boundary have stretched northeastward across Pennsylvania (Fig. 3.19a). The band of enhanced rainfall seen in the 6-h precipitation analysis ending 0000 UTC 18 September (Fig. 3.19b) occurs along and on the cool side of the mesoscale boundary seen in Figs. 3.18b and 3.19a.

Both Ivan and the surface boundary have progressed eastward by 0600 UTC 18 September (Fig. 3.20a) and 1200 UTC 18 September (Fig. 3.21a). Once again, the highest 6-h precipitation accumulations ending 0600 UTC 18 September (Fig. 3.20b) are found along the aforementioned mesoscale boundary. By 1200 UTC 18 September, rainfall amounts exceeding 135 mm can be seen along the Pennsylvania–New Jersey border (Fig. 3.21b).

3.2.2 TC Jeanne (2004)

3.2.2.1 Overview and Storm-Total Precipitation Analysis

Jeanne, which formed from an African easterly wave, made landfall near Stuart, Florida, early on 26 September 2004 as a category 3 hurricane. After landfall, Jeanne moved northward through the southeast U.S. on 27–28 September and then northeastward toward the mid-Atlantic coast on 28–29 September (Fig. 3.22). Jeanne underwent ET while interacting with a frontal boundary over the eastern U.S. and became extratropical at 0000 UTC 29 September. In the U.S., Jeanne was responsible for six deaths and caused almost seven billion dollars in damage (Franklin et al. 2006).

Examination of storm-total precipitation distribution versus TC track for 1200 UTC 26–1200 UTC 29 September reveals that Jeanne was associated with a shift from a ROT precipitation distribution over the southeast U.S. to a LOT precipitation distribution from Virginia northeastward into southern New England (Fig. 3.22). The heaviest precipitation is located in a southwest–northeast-oriented band from Virginia through southeastern Pennsylvania into coastal sections of southern New England. Maximum rainfall amounts exceeding 180 mm are found north of the TC track in a narrow band over southeast Pennsylvania.

3.2.2.2 Upper-Air Analysis

Precipitable water and 300-hPa analyses for 1200 UTC 27 September show a plume of moist tropical air (precipitable water values >30 mm) situated under a broad ridge over the southeastern U.S. and western Atlantic, with maximum precipitable water values >60 mm found near Jeanne (Fig. 3.23). Cyclonic flow around a positively tilted midlatitude trough is evident over central Canada, while a zonally oriented upper-level (i.e., 300-hPa) jet streak is embedded within the midlatitude westerly flow over the northern U.S. and southern Canada. An area of divergence, which is associated with the TC-induced upper-level outflow from Jeanne, is apparent over the southeast U.S.

Interactions between Jeanne and its midlatitude environment have led to an amplification of the upper-level flow pattern 18 h later (0600 UTC 28 September; Fig. 3.24). In response to the TC-induced ridge building, a tightening of the geopotential height gradient is seen between the midlatitude trough that is located to the northwest of Jeanne and the ridge that is located downstream of Jeanne. Subsequent intensification of the upper-level jet streak (maximum winds >50 m s^{-1}) occurs over eastern Canada, while it acquires a more meridional orientation than in the prior analysis as the midlatitude trough has sharpened.

By 1800 UTC 28 September, the upper-level jet streak continues to advance downstream into the northeastern U.S and eastern Canada as the midlatitude trough digs southeastward (Fig. 3.25). A band of upper-level divergence has formed across Virginia northeastward through southern New England due to the juxtaposition of the divergence that is associated with the upper-level outflow from Jeanne and the divergence that is characteristically found in the right entrance region of the upper-level jet streak. Underneath the upper-level ridge, the moisture-rich environment (maximum precipitable water around 50–60 mm) continues to advance northward as Jeanne moves toward the mid-Atlantic coast (Figs. 3.24 and 3.25).

Radar reflectivity and 925-hPa analyses at 0600 UTC 28 September reveal a midlatitude θ_e boundary, and an area of precipitation is located along the periphery of a distinct θ_e ridge over the southeastern U.S. (Fig. 3.26). On the eastern side of Jeanne, a line of convection is embedded within the θ_e ridge and along a south–north-oriented low-level (i.e., 925-hPa) jet. Heavy precipitation seen to the north of Jeanne is collocated with the nose of the low-level jet, where tropical air is transported poleward and inland from the Atlantic.

By 1800 UTC 28 September, a northeastward expansion of the precipitation field from northern Virginia through southern New England is evident along the midlatitude θ_e boundary (Fig. 3.27). The south–north-oriented low-level jet is enhancing the poleward transport of tropical (i.e., high θ_e) air from the Atlantic into the θ_e boundary, while the southerly flow that is associated with this jet on the warm side of the θ_e boundary is confluent with the northerly flow on the cool side of the boundary.

Six hours later (0000 UTC 29 September), a distinct band of heavy precipitation that stretches from eastern Maryland into central New Jersey is embedded in the broad shield of precipitation (Fig. 3.28). This band is found just to the northeast of Jeanne, where the nose of the low-level jet and θ_e-ridge axis intersects the midlatitude θ_e boundary. The heavy precipitation associated with Jeanne quickly weakens and moves offshore by 0600 UTC 29 September (not shown).

Q vector diagnostics at 925 hPa for 0600 UTC 28 September reveal a distinct Q vector divergence–convergence couplet located near Jeanne (Fig. 3.29a). The Q_n component does not have a marked contribution (Fig. 3.29b) toward the total QG forcing for vertical motion seen in Fig. 3.29a as the midlatitude baroclinic zone over the mid-Atlantic region (which is associated with the aforementioned midlatitude θ_e boundary) is situated far away from Jeanne. However, the total QG forcing for ascent (descent) is primarily related to a Q_s couplet pattern that contains Q_s convergence (divergence) to the northeast (southwest) of Jeanne (Fig. 3.29c). At 300 hPa, Q_n vector diagnostics (Fig. 3.29d) show strong QG frontogenesis with a Q_n divergence–convergence banded pattern that is associated with a thermally direct transverse ageostrophic circulation in the entrance region of the upper-level jet streak (see Fig. 3.24). Also, a weak frontal circulation that is located to the west of Jeanne has formed from the interaction between the TC-induced upper-level outflow and the midlatitude environment (Fig. 3.29d).

Diagnostics 12 h later (1800 UTC 28 September; Fig. 3.30a) show that the Q vector divergence–convergence couplet associated with Jeanne has moved northeastward. At this time, the strongest QG forcing for ascent to the northeast of Jeanne is centered over the northern Chesapeake Bay and is collocated with the heaviest precipitation (see Fig. 3.27). To the northeast of Jeanne, a southwest–northeast-oriented warm-frontal boundary, which was not present 6 h earlier (not shown), has formed as Jeanne interacts with the midlatitude baroclinic zone (Fig. 3.30b). This warm-frontal boundary, which is marked by a region of QG frontogenesis, corresponds to a thermally direct transverse ageostrophic circulation with a Q_n divergence–convergence band that is positioned in between Jeanne and the downshear thermal ridge. The Q_s pattern is still predominantly characterized by a divergence–convergence couplet with Q_s divergence (convergence) located to the southwest (northeast) of Jeanne (Fig. 3.30c). The 300-hPa divergence–convergence banded structure that is positioned in the entrance region of the upper-level jet streak has progressed eastward into the upper Midwest and eastern Canada (Fig. 3.30d).

The Q vector diagnostics at 0000 UTC 29 September (Figs. 3.31a–d) and 0600 UTC 29 September (Figs. 3.32a–d) illustrate overall patterns similar to those seen in prior analyses. The strongest QG forcing for ascent, centered over southern New Jersey at 0000 UTC 29 September (Fig. 3.31a) and off the New Jersey coast at 0600 UTC 29 September (Fig. 3.32a), is once again collocated with the heaviest precipitation observed at each respective time (see Fig. 3.28; not shown for 0600 UTC 29 September). The QG frontogenesis in the vicinity of the thermal ridge is still evident as the warm-frontal boundary slowly progresses toward the mid-Atlantic coast by 0000 UTC 29 September (Fig. 3.31b) and offshore by 0600 UTC 29 September (Fig. 3.32b). The strongest 925-hPa frontogenesis observed during the Jeanne study is identified at 0000 UTC 29 September, with maximum frontogenesis values >3 K (100 km)$^{-1}$ (3 h)$^{-1}$ found over New Jersey (not shown). The Q_s divergence–convergence couplet seen at 0000 UTC 29 September (Fig. 3.31c) and at 0600 UTC 29 September (Fig. 3.32c) still contains Q_s divergence (convergence) to the southwest (northeast) of Jeanne. This Q_s pattern contributes to a cyclonic rotation of the potential temperature gradient from the eastern side of the thermal trough to the western side of the thermal ridge. To the northeast of Jeanne, the 300-hPa Q_n divergence–convergence banded structure associated with upper-level jet streak (not shown) has progressed eastward into Maine and eastern Canada by 0000 UTC 29 September (Fig. 3.31d) and 0600 UTC 29 September (Fig. 3.32d).

3.2.2.3 Vertical Cross-Section Analysis

Cross sections will be presented to illustrate the vertical structure of the warm-frontal boundary accompanying Jeanne. Cross-section analyses at 1800 UTC 28

September (Fig. 3.33, orientation shown in Fig. 3.30b) and 0000 UTC 29 September (Fig. 3.34, orientation shown in Fig. 3.31b) are illustrated during the time of the strongest 925–500-hPa layer-averaged frontogenesis (not shown) and heaviest precipitation.

At 1800 UTC 28 September, the heaviest precipitation accompanying Jeanne (see Fig. 3.27) is found over an area where weak frontogenesis [≤2.5 K $(100\ \mathrm{km})^{-1}$ $(3\ \mathrm{h})^{-1}$] is present in the boundary layer (Fig. 3.33). Weak-to-moderate frontogenesis located in the entrance region of the upper-level jet streak (see Fig. 3.25) is evident in the 500–200-hPa layer, with maximum frontogenesis values [>3.0 K $(100\ \mathrm{km})^{-1}$ $(3\ \mathrm{h})^{-1}$] centered around 325 hPa. Although there is negligible frontogenesis present at midlevels, an apparent tilt toward the cooler air with height is seen among the lower- and upper-level frontogenesis features. The region of lower-level frontogenesis is situated within an area of tropospheric-deep relative humidity values >90%. Ascent is present above and on the warm side of the lower-level frontogenesis maximum, with ascent ($\leq -12\ \mu\mathrm{b\ s}^{-1}$) maximized in the 700–450-hPa layer. In the boundary layer, the southerly flow on the warm side of the frontal boundary is confluent with the northerly flow on the cool side of the boundary. Above the boundary layer, a predominant southwesterly flow associated with the circulation of Jeanne is observed along and on the warm side of the boundary.

At 0000 UTC 29 September, maximum low-level frontogenesis values have noticeably increased since the previous analysis to >2.5 K $(100\ \mathrm{km})^{-1}$ $(3\ \mathrm{h})^{-1}$ (Fig. 3.34). Both the frontogenesis and ascent pattern tilts toward the cooler air with height. In the 800–700-hPa layer, maximum ascent values $\leq -16\ \mu\mathrm{b\ s}^{-1}$ are present directly above the low-level frontogenesis maximum. Figure 3.34 provides evidence for coupling between the lower- and upper-level frontogenesis patterns as the ascent pattern tilts noticeably with height from the lower-level frontogenesis maximum towards the upper-level frontogenesis maximum.

3.2.2.4 Mesoscale Precipitation and Surface Analysis

Surface analyses at 1800 UTC 28 September reveal that a surface frontal boundary, which is not evident in the analysis at 1200 UTC 28 September (not shown), is marked by frontogenesis with a banded F_n divergence–convergence pattern to the northeast of Jeanne (Fig. 3.35a). The formation of this surface frontal boundary is coincident with the formation of the 925-hPa warm-frontal boundary (see Figs. 3.30b and 3.33). The cyclonic flow associated with the circulation of Jeanne encompasses the entire mid-Atlantic region, resulting in a southeasterly influx of tropical air from the Atlantic into the surface boundary. Confluent flow characterizes the southwest–northeast-oriented surface boundary stretching from northern Virginia to coastal New England.

Six hours later (0000 UTC 29 September), the F_n divergence–convergence band has become better defined than in the previous analysis along the surface potential temperature ridge (Fig. 3.35b). A mesoscale precipitation structure is evident in Fig. 3.35c, with the heaviest 6-h precipitation ending at 0000 UTC 29 September occurring along the aforementioned surface boundary. Rainfall amounts of at least 60 mm are located along a narrow band stretching from eastern Maryland to central New Jersey, while heavy rainfall (>150 mm) is found within this band over parts of southeast Pennsylvania.

By 0600 UTC 29 September, Jeanne and the accompanying surface boundary have quickly exited off the Delaware coast (Fig. 3.36a). Additional rainfall accumulations are observed from the northern mid-Atlantic to southern New England coast, with maximum 6-h amounts >60 mm located along the Delaware–New Jersey border (Fig. 3.36a).

3.2.3 TC Ernesto (2006)

3.2.3.1 Overview and Storm-Total Precipitation Analysis

Ernesto developed from an African easterly wave and eventually made U.S. landfall in extreme southern Florida on 30 August 2006. After tracking northward off the southeastern U.S. coast, Ernesto made a second landfall near Wilmington, North Carolina, on 1 September (Fig. 3.37). Following landfall, Ernesto continued to track northward through the eastern mid-Atlantic region and into western New York during 1–3 September. Ernesto underwent ET as it interacted with a frontal boundary and was classified as extratropical at 1800 UTC 1 September (Knabb and Mainelli 2006).

Ernesto exhibited a ROT precipitation distribution over the mid-Atlantic region (Fig. 3.37). Storm-total rainfall amounts in excess of 140 mm are found in a band from eastern North Carolina extending northward into the southern Delmarva Peninsula, with maximum precipitation accumulations >420 mm observed over the southern Chesapeake Bay.

3.2.3.2 Upper-Air Analysis

Analyses at 300 hPa for 1200 UTC 31 August reveal a blocking pattern, with an upper-level (i.e., 300-hPa) ridge situated over central Canada and a weak upper-level trough over the central U.S. (Fig. 3.38). Downstream of the blocking region, an area of confluent flow created by the intersection of cyclonic flow around a closed low over eastern Canada and anticyclonic flow over the western Atlantic results in a primary upper-level jet streak that is positioned well off the northeast U.S. coast. This primary jet streak, which is oriented zonally, contains maximum winds exceeding 65 m s^{-1} near Nova Scotia. A secondary jet streak on the order of 35 m s^{-1} is located south of Lake Erie in between the weak trough that is over the central U.S. and the TC-induced ridge over the southeast U.S., while an area of divergence is found in between Ernesto and the secondary jet streak. The precipitable water analysis at this time reveals a broad plume with values >40 mm situated underneath the southeast U.S. ridge, and maximum values >60 mm located near Ernesto. A sharp north to south precipitable water boundary is situated across the mid-Atlantic region.

Subsequent 300-hPa analyses illustrate little movement in the weak trough over the Midwest at 0000 UTC 1 September (Fig. 3.39) and 1200 UTC 1 September (Fig. 3.40). The TC-induced ridge that has amplified over the eastern U.S. has not led to a strengthening of the geopotential height gradient due to the absence of a significant midlatitude trough upstream of Ernesto. Accordingly, the secondary upper-level jet streak over the Ohio Valley has weakened over the 24-h period ending at 1200 UTC 1 September. As Ernesto nears landfall by 0000 UTC 1 September, high precipitable water values (>60 mm) associated with Ernesto are located along the Carolina coast, while the well-defined precipitable water boundary over the mid-Atlantic region has pushed slightly southward (Fig. 3.39). By 1200 UTC 1 September, a band of divergence has formed on the northern and eastern sides of Ernesto as a result of the coupling between the divergence from the upper-level outflow of Ernesto and the divergence that is typically found in the right entrance region of the primary upper-level jet streak that surrounds the closed low (Fig. 3.40).

Radar reflectivity and 925-hPa analyses near the time of landfall (0000 UTC 1 September) reveal a broad shield of precipitation accompanying Ernesto that is centered over eastern North Carolina, while a smaller area of precipitation associated with a weak midlatitude disturbance is located across Ohio and West Virginia (Fig. 3.41). Ernesto is located just to the south of a zonally oriented midlatitude θ_e boundary over the mid-Atlantic region. A southerly low-level (i.e., 925-hPa) jet (maximum wind speeds of 25 m s^{-1}) is located on the eastern side of Ernesto and in a region characterized by strong cyclonic flow. This low-level jet is acting to transport tropical (i.e., high θ_e) air from the Atlantic into the southern part of the midlatitude θ_e boundary that is oriented along the North Carolina coast. The heaviest precipitation at this time is focused along this θ_e boundary.

Subsequent analyses at 1200 UTC 1 September (Fig. 3.42) and 0000 UTC 2 September (Fig. 3.43) show an amplification of the θ_e pattern as Ernesto becomes embedded in the midlatitude θ_e boundary, with θ_e trough (ridge) development occurring on the western (eastern) side of Ernesto. The low-level jet, which has become cyclonically curved, is associated with southerly flow just to the east of Ernesto and easterly flow along the θ_e boundary to the north of Ernesto. The ~30 m s^{-1} easterly wind maximum that is found over southeast Virginia at 1200 UTC 1 September (Fig. 3.42) has increased to ~35 m s^{-1} over Delaware by 0000 UTC 2 September (Fig. 3.43). A broad shield of moderate to heavy precipitation is positioned within the θ_e boundary on the northern side of Ernesto. The heaviest precipitation that is embedded in the θ_e boundary is coincident with the onshore (i.e., easterly) wind maximum at the nose of the jet, where tropical air is still being transported inland from the Atlantic (Figs. 3.42 and 3.43).

The 925-hPa Q vector diagnostics at 0000 UTC 1 September reveal a distinct Q vector divergence–convergence couplet surrounding Ernesto with strong QG forcing for descent (ascent) located in between Ernesto and a thermal trough (ridge) (Fig. 3.44a). The QG forcing for ascent to the northeast of Ernesto is located in the vicinity of the heaviest precipitation (see Fig. 3.41). A warm-frontal boundary, which is not evident in the previous 6-h analysis (not shown), has formed on the northeastern side of Ernesto (Fig. 3.44b). This warm-frontal boundary is marked by an area of QG frontogenesis and a southwest–northeast-oriented Q_n divergence–convergence band that formed parallel to the southeastern U.S. coastline and in between the thermal trough and ridge. The QG forcing pattern for ascent (descent) (Fig. 3.44a) is dominated by the Q_s component (Fig. 3.44c). The Q_n vector diagnostics at 300 hPa show an upper-level thermal ridge associated with Ernesto over the southeast U.S., while strong QG frontogenesis is located along a zonally oriented Q_n divergence–convergence banded pattern that extends from New England eastward into the western Atlantic (Fig. 3.44d). The Q_n divergence–convergence structure, which corresponds to a thermally direct transverse ageostrophic circulation in the entrance region of the primary upper-level jet streak (see Fig. 3.39), is positioned far to the northeast of Ernesto since the upper-level thermal trough that is associated with the closed low (see Fig. 3.39) is located near Newfoundland.

The Q vector divergence–convergence couplet surrounding Ernesto has expanded northward by 1200 UTC 1 September as the center of Ernesto has become embedded within the midlatitude baroclinic zone (Fig. 3.45a). At this time, the strongest QG forcing for ascent and heaviest precipitation (see Fig. 3.42) are collocated over eastern Virginia. The banded Q_n divergence–convergence structure associated with the warm-frontal boundary has increased in size and intensity during the previous 12 h, as strong QG frontogenesis and Q_n convergence are seen along the eastern side of the thermal ridge (Fig. 3.45b). The strongest 925-hPa frontogenesis seen during the Ernesto study is identified at this time, with maximum frontogenesis values exceeding >6 K (100 km)$^{-1}$ (3 h)$^{-1}$ found over southeast Virginia (not shown). The Q_s analysis (Fig. 3.45c) reveals a similar configuration as seen 12 h earlier, with the Q_s divergence–convergence pattern dominating the QG forcing pattern for vertical motion seen in Fig. 3.45a. The robust Q_s pattern surrounding Ernesto contributes to a cyclonic rotation of the potential temperature gradient from the eastern side of the thermal trough to the western side of the thermal ridge. At 300 hPa, the strongest QG frontogenesis and associated Q_n divergence–convergence band is still far to the northeast of Ernesto (Fig. 3.45d).

By 0000 UTC 2 September, a noticeable weakening in the Q vector divergence–convergence couplet (Fig. 3.46a) during the past 12 h is primarily associated with a weakening in the Q_s forcing (Fig. 3.46c). The strongest QG forcing for ascent, which is now focused around the Delmarva Peninsula, is in close proximity to the heavy precipitation evident in Fig. 3.43. A slight weakening in the banded Q_n divergence–

convergence structure that is associated with the warm-frontal boundary is apparent in Fig. 3.46b, while the strongest QG frontogenesis has moved off the mid-Atlantic coast. The Q_s pattern near Ernesto continues to contribute towards a cyclonic rotation of the thermal wave pattern from the eastern side of the thermal trough to the western side of the thermal ridge (Fig. 3.46c). The 300-hPa Q_n banded structure has progressed slowly eastward as the upper-level thermal ridge associated with Ernesto builds over the eastern U.S. during the past 24 h (Fig. 3.46d).

3.2.3.3 Vertical Cross-Section Analysis

Cross sections will be presented in this subsection to reveal the vertical structure of the warm-frontal boundary associated with Ernesto. Cross-section analyses at 0000 UTC 1 September (Fig. 3.47, orientation shown in Fig. 3.44b), 1200 UTC 1 September (Fig. 3.48, orientation shown in Fig. 3.45b), and 0000 UTC 2 September (Fig. 3.49, orientation shown in Fig. 3.46b) are illustrated during the period of the strongest 925–500-hPa layer-averaged frontogenesis (not shown) and heaviest precipitation.

At 0000 UTC 1 September, a region of weak to moderate frontogenesis [>2.5 K $(100\ \mathrm{km})^{-1}$ $(3\ \mathrm{h})^{-1}$] in the boundary layer (Fig. 3.47), which is associated with the warm-frontal boundary, has formed along the North Carolina coastline and is coincident with the heavy precipitation seen in Fig. 3.41. This region of frontogenesis is located beneath upright tropospheric-deep ascent and within a region of >90% relative humidity throughout the troposphere. At this time, significant upper-level frontogenesis is absent as the primary upper-level jet streak (see Fig. 3.39) is situated far east of the cross section. Confluent flow is established in the boundary layer, with southerly (easterly) flow occurring on the warm (cool) side of the warm-frontal boundary. Above the boundary layer, the predominantly southerly flow associated with the circulation of Ernesto is evident over the warm-frontal boundary.

Significant changes in the vertical structure are observed by 1200 UTC 1 September (Fig. 3.48). The frontogenesis focused in the boundary layer has become much stronger than 12 h earlier (see Fig. 3.47), with maximum values >5.0 K $(100\ \text{km})^{-1}$ $(3\ \text{h})^{-1}$. Strong, upright ascent is located over and on the warm side of the frontal boundary, with maximum values ≤ -32 μb s^{-1} present in the 700–500-hPa layer. The vigorous low-level convergence that is implied by large values of $\partial\omega/\partial p > 0$ in the boundary layer provides evidence for enhanced lift over the frontal boundary.

On the equatorward side of the jet-entrance region, the upper-level frontogenesis has strengthened since the previous analysis to around 2.5–3.0 K $(100\ \text{km})^{-1}$ $(3\ \text{h})^{-1}$ by 0000 UTC 2 September (Fig. 3.49). A tilt toward cooler air with height in both the frontogenesis and ascent patterns is evident at this time. Two ascent maxima are observed in Fig. 3.49, with one located around 850 hPa just above and on the warm side of lower-level frontogenesis maximum and the other located around 550 hPa in between the lower- and upper-level frontogenesis maxima.

3.2.3.4 Mesoscale Precipitation and Surface Analysis

Surface analyses at 0000 UTC 1 September show no evidence of a surface frontal boundary as Ernesto nears landfall (Fig. 3.50a). However, a surface frontal boundary, which is associated with the previously discussed upper-level warm-frontal boundary, has emerged on the northeastern side of Ernesto along the North Carolina coast by 0600 UTC

1 September (Fig. 3.50b). The surface boundary is identified by an area of strong frontogenesis with a southwest–northeast-oriented F_n divergence–convergence band. The onshore (i.e., southeasterly) flow on the warm side of the boundary is confluent with the northeasterly flow on the cool side of the boundary. The precipitation analysis for the 6-h time period ending 0600 UTC 1 September (Fig. 3.50c) reveals a band of rainfall that is oriented along the surface boundary seen in Figs. 3.50a,b. Heavier precipitation amounts >75 mm are observed closer to the coast, with maximum accumulations of ~150 mm located over southern coastal sections of North Carolina.

By 1200 UTC 1 September, the mesoscale boundary has progressed farther north to the eastern North Carolina–Virginia border (Fig. 3.51a). Strong confluent flow along the surface boundary is coincident with the intense ascent seen in Fig. 3.48. Strong frontogenesis is focused along the surface boundary, while easterly flow acts to transport tropical moisture from the Atlantic into the surface boundary. In the 6-h precipitation analysis ending 1200 UTC 1 September (Fig. 3.51b), an area of heavy rainfall is observed along the surface boundary seen in Figs. 3.50b and 3.51a. The heaviest precipitation is located in a band from eastern North Carolina to the southeast Virginia border, with maximum rainfall amounts of ~135 mm over parts of eastern North Carolina and coastal Virginia.

Along the surface boundary, the frontogenesis and well-defined F_n divergence–convergence band is near its maximum intensity by 1800 UTC 1 September (Fig. 3.52a). Once again, onshore (i.e., easterly) flow is transporting copious amounts of tropical Atlantic moisture into the highly confluent frontal zone. In the 6-h precipitation analysis ending 1800 UTC 1 September, excessive amounts of rainfall are found along the aforementioned surface boundary, with the heaviest 6-h precipitation exceeding 180 mm over southeastern Virginia (Fig. 3.52b).

The surface frontogenesis and associated F_n divergence–convergence band weaken by 0000 UTC 2 September (Fig. 3.53a). The heaviest 6-h precipitation ending at 0000 UTC 2 September occurs once again along the aforementioned surface boundary, with maximum rainfall amounts of ~165 mm seen around the southern Chesapeake region (Fig. 3.53b). Nearly all of the 6-h accumulated precipitation is observed in the beginning part of the 6-h period (not shown), when the surface and upper-level dynamics accompanying Ernesto are maximized.

Table I. A 52-storm dataset of landfalling or transitioning TCs that produced ≥ 100 mm of rainfall in the northeast U.S. for 1950–2006.

Year	Name	Date	Max Rainfall (mm)
1950	Able	19–21 Aug	100–125
1950	Dog	11–13 Sep	100–125
1952	Able	31 Aug–2 Sep	150–175
1953	Barbara	13–16 Aug	100–125
1953	Carol	5–8 Sep	—
1954	Carol	30 Aug–1 Sep	125
1954	Edna	9–12 Sep	200
1954	Hazel	14–16 Oct	250+
1955	Connie	11–14 Aug	175–200
1955	Diane	17–20 Aug	500+
1955	Ione	19–21 Sep	—
1958	Helene	26–29 Aug	—
1959	Cindy	8–11 Jul	—
1959	Gracie	29 Sep–2 Oct	—
1960	Brenda	28–31 Jul	150–175
1960	Donna	11–13 Sep	200
1961	Esther	20–26 Sep	200
1962	Alma	27–30 Aug	150
1962	Daisy	5–8 Oct	350
1963	Ginny	28–30 Oct	100–125
1969	Gerda	8–10 Sep	100–125
1971	Doria	26–29 Aug	250
1971	Heidi	12–15 Sep	125
1972	Agnes	20–23 Jun	250+
1972	Carrie	1–5 Sep	300
1976	Belle	8–11 Aug	125
1979	David	4–7 Sep	375+
1979	Frederic	13–14 Sep	150–175
1985	Gloria	26–28 Sep	200
1988	Chris	28–30 Aug	125+
1991	Bob	17–20 Aug	225
1996	Bertha	12–14 Jul	175
1996	Edouard	1–3 Sep	150
1996	Fran	7–9 Sep	250+
1997	Danny	25–26 Jul	150–175
1999	Floyd	15–18 Sep	300+
2001	Allison	15–17 Jun	125–150
2002	Isidore	27–29 Sep	75–100
2002	Kyle	11–13 Oct	150+

2003	Bill	2–4 Jul	125+
2003	Isabel	18–20 Sep	500+
2004	Alex	1–4 Aug	175+
2004	Bonnie	13–15 Aug	150+
2004	Charley	14–16 Aug	(see Bonnie)
2004	Frances	8–10 Sep	200–225
2004	Gaston	29 Aug–1 Sep	250+
2004	Ivan	17–19 Sep	175–200
2004	Jeanne	28–30 Sep	175–200
2005	Cindy	7–10 Jul	175–200
2005	Katrina	30 Aug–1 Sep	125–150
2005	Ophelia	15–17 Sep	125–150
2006	Ernesto	31 Aug–2 Sep	250+

a)

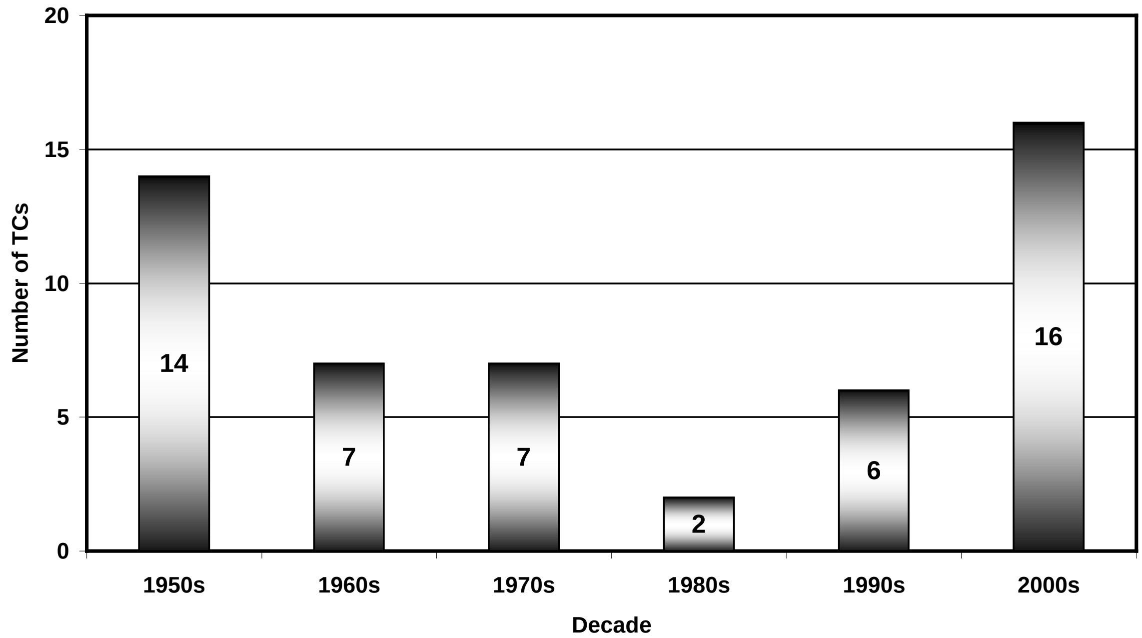

b)

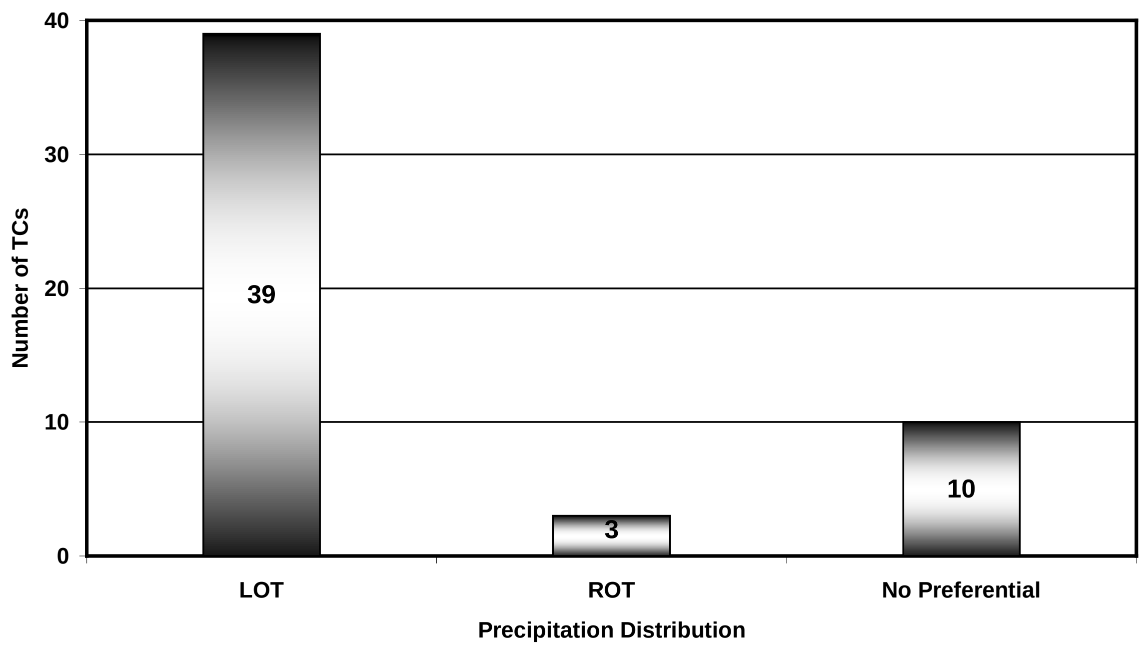

Fig. 3.1. Climatology statistics from the 52-TC dataset (1950–2006) shown in Table I by: (a) decade, (b) precipitation distribution versus TC track, and (c) month.

c)

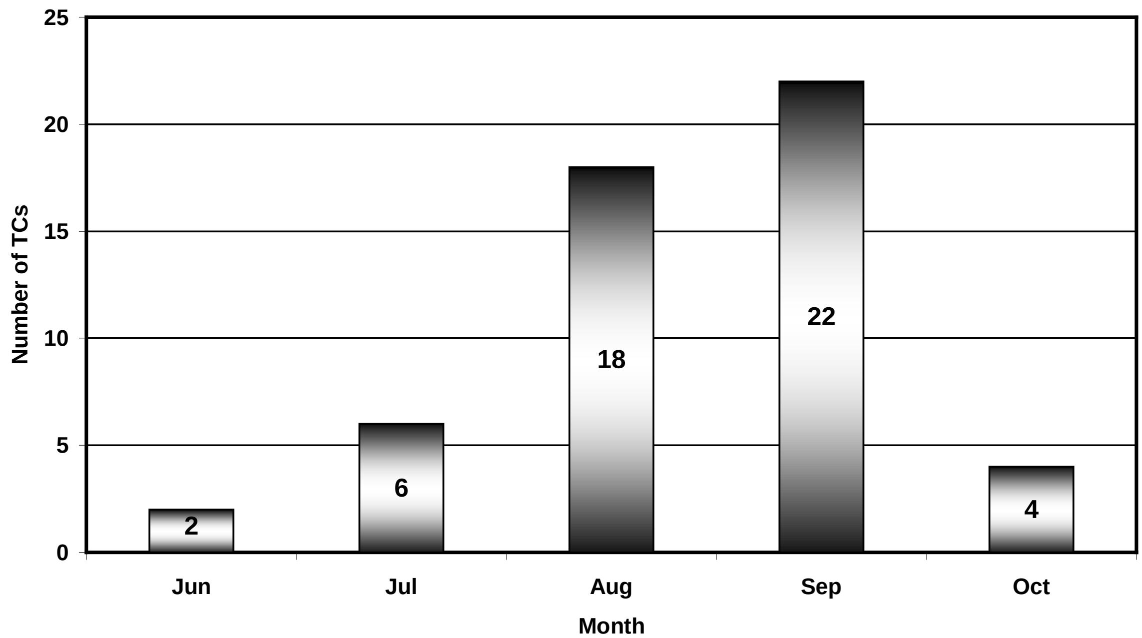

Fig. 3.1. *continued*.

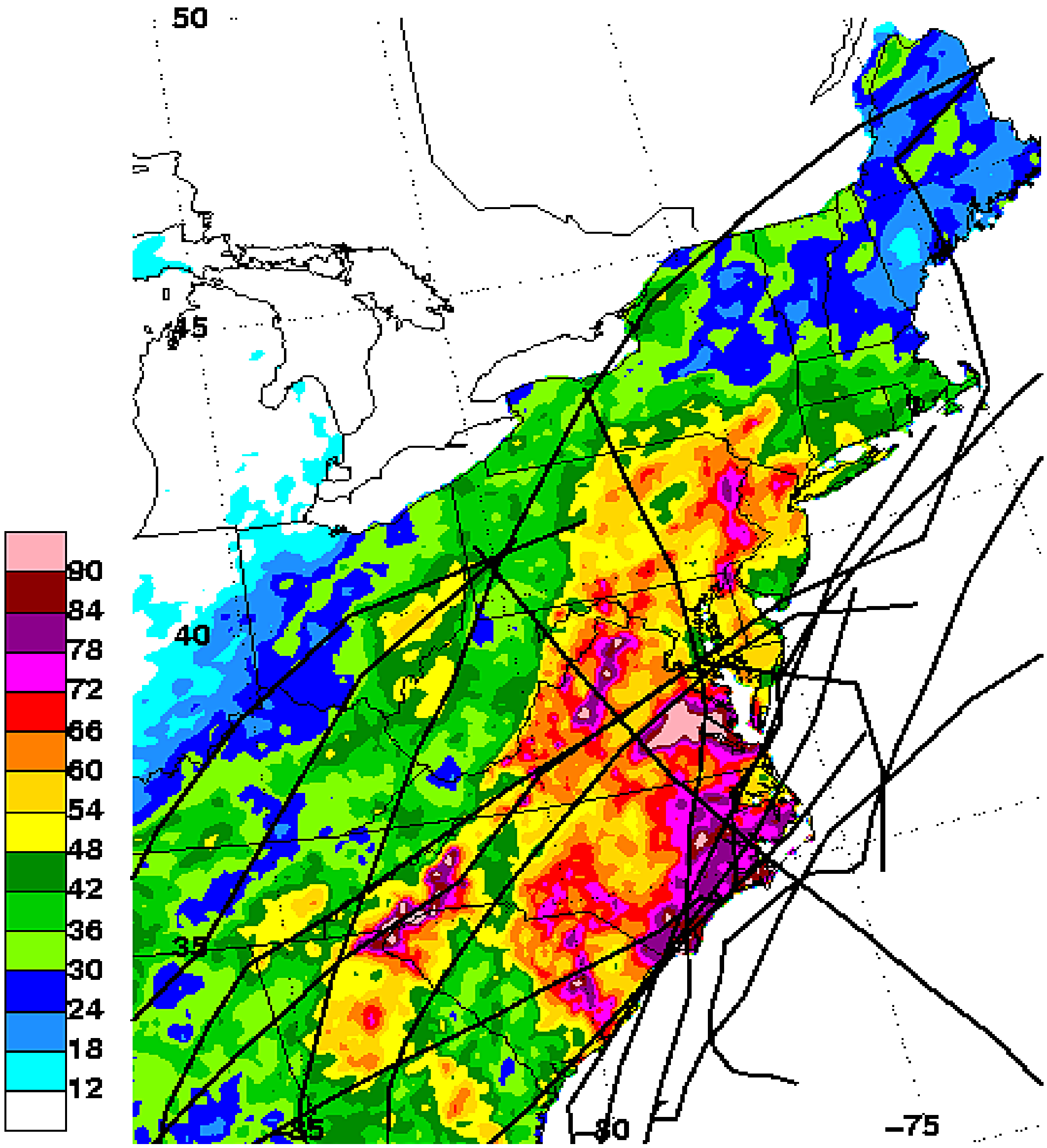

Fig. 3.2. Total accumulated precipitation (shaded every 6 cm) and tracks from the 16 TCs for 2001–2006 (see Table I). Precipitation data are calculated using RFC QPE data while tracks are derived from NHC best track data.

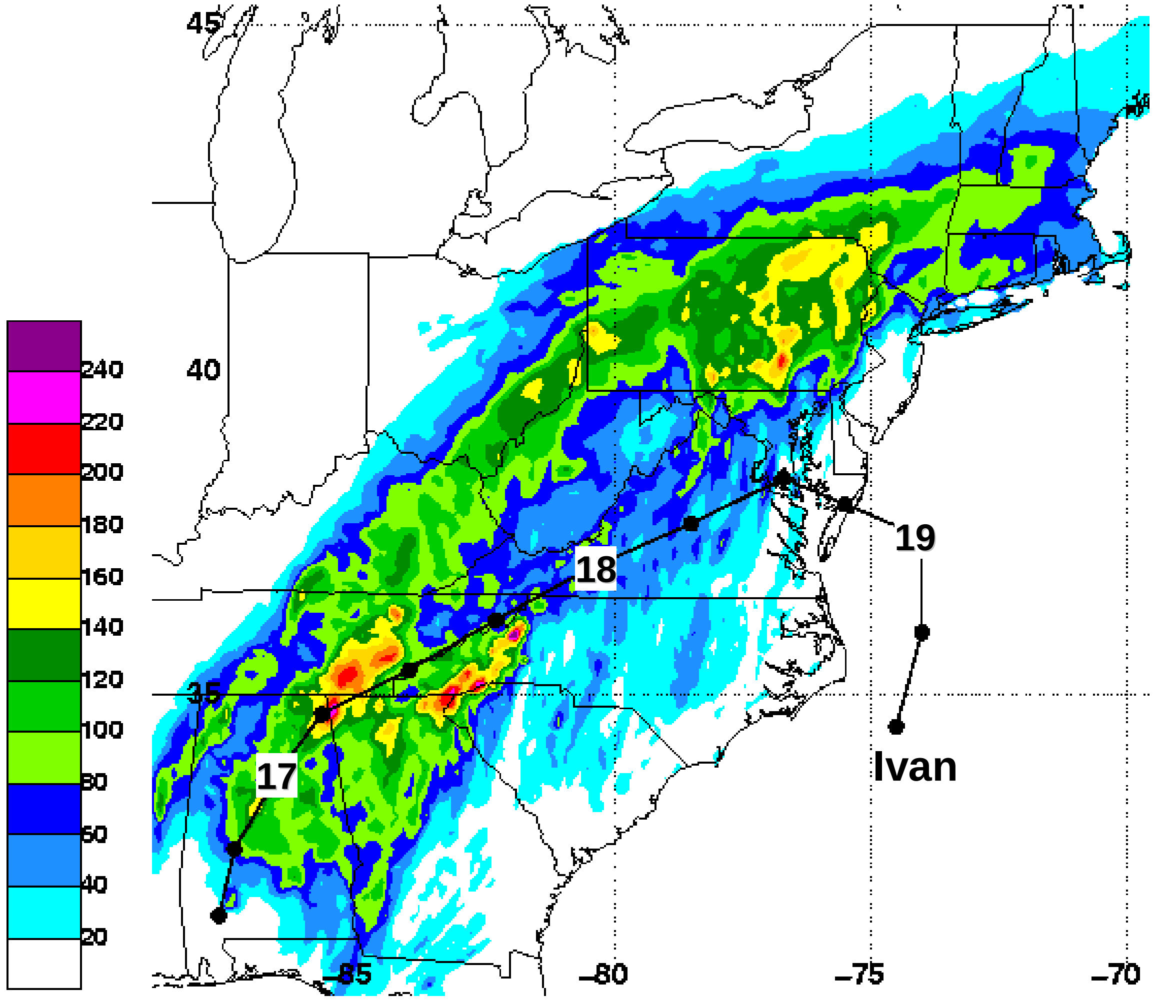

Fig. 3.3. Storm-total precipitation (shaded every 20 mm) versus TC track associated with Ivan for 1200 UTC 16–1200 UTC 19 September 2004. The black dots represent 6-h TC positions with dates denoting the 0000 UTC TC position.

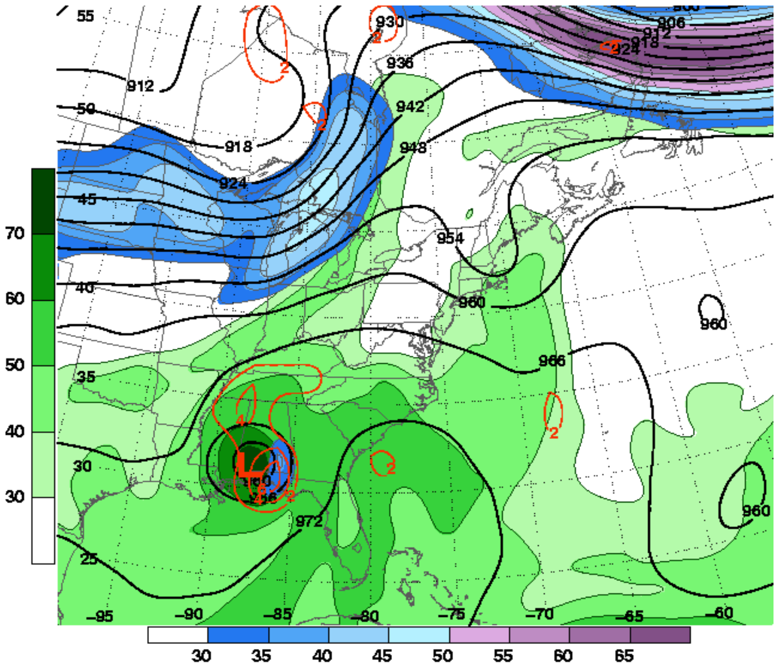

Fig. 3.4. Precipitable water shaded every 10 mm starting at 30 mm (color scale on the left) and 300-hPa analysis of geopotential height contoured in black every 6 dam, wind speed shaded every 5 m s^{-1} starting at 30 m s^{-1} (color scale on the bottom), divergence contoured in red every 2×10^{-5} s^{-1}, and NHC best track TC position denoted by a red "L" at 1200 UTC 16 September 2004.

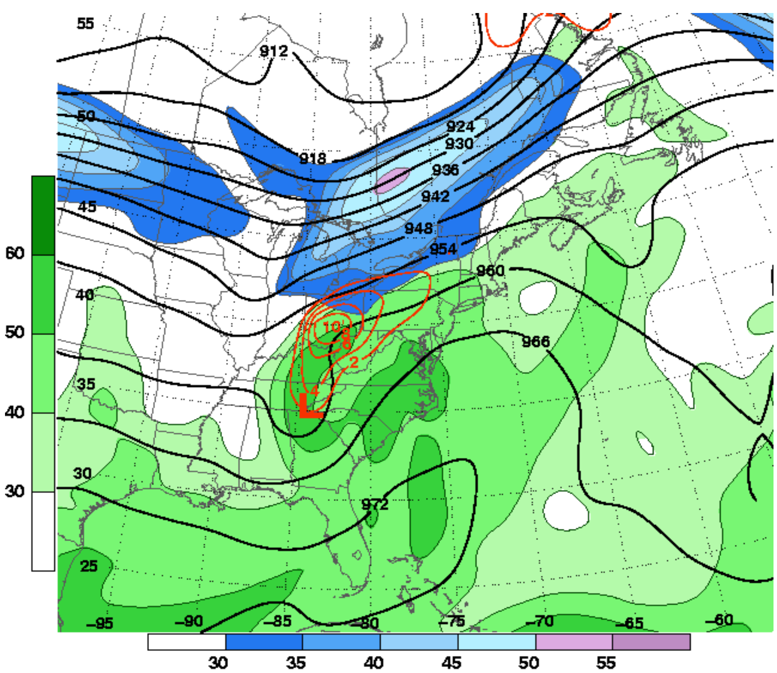

Fig. 3.5. Same as in Fig. 3.4 except at 1200 UTC 17 September 2004.

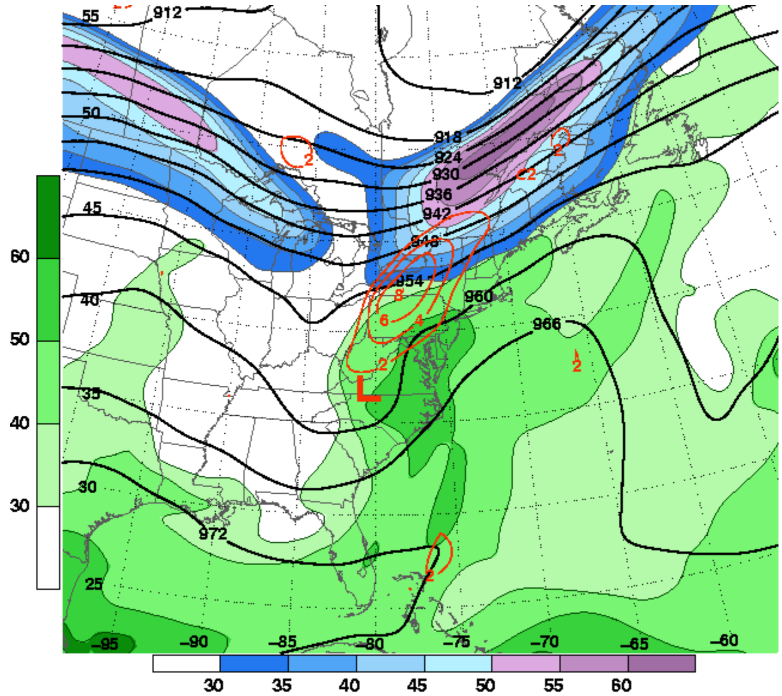

Fig. 3.6. Same as in Fig. 3.4 except at 0000 UTC 18 September 2004.

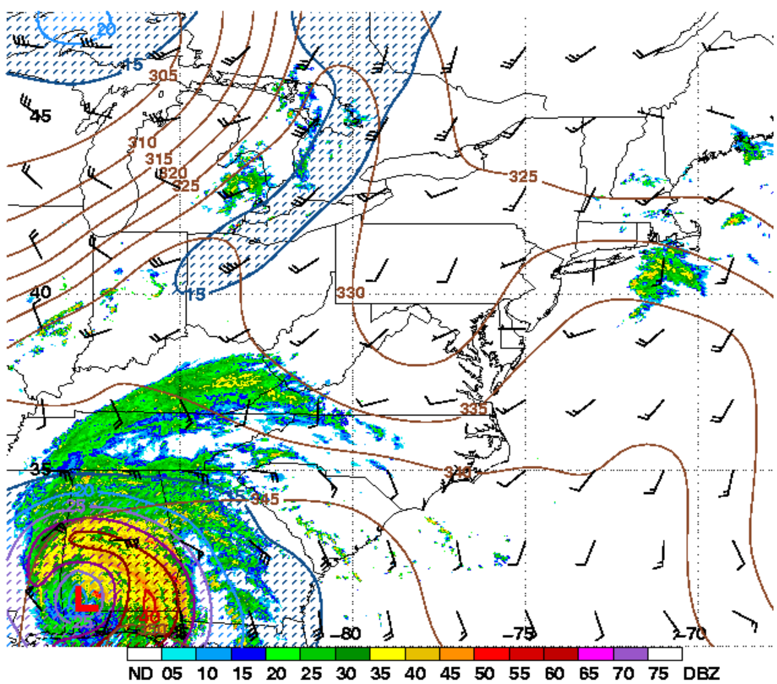

Fig. 3.7. Radar reflectivity shaded every 5 dBZ (color scale on the bottom) and 925-hPa wind speed stippled and contoured every 5 m s^{-1} starting at 15 m s^{-1}, wind barbs (1 pennant = 25 m s^{-1}, 1 full wind barb = 5 m s^{-1}, 1 half wind barb = 2.5 m s^{-1}), and θ_e contoured in brown every 5 K at 1200 UTC 16 September 2004.

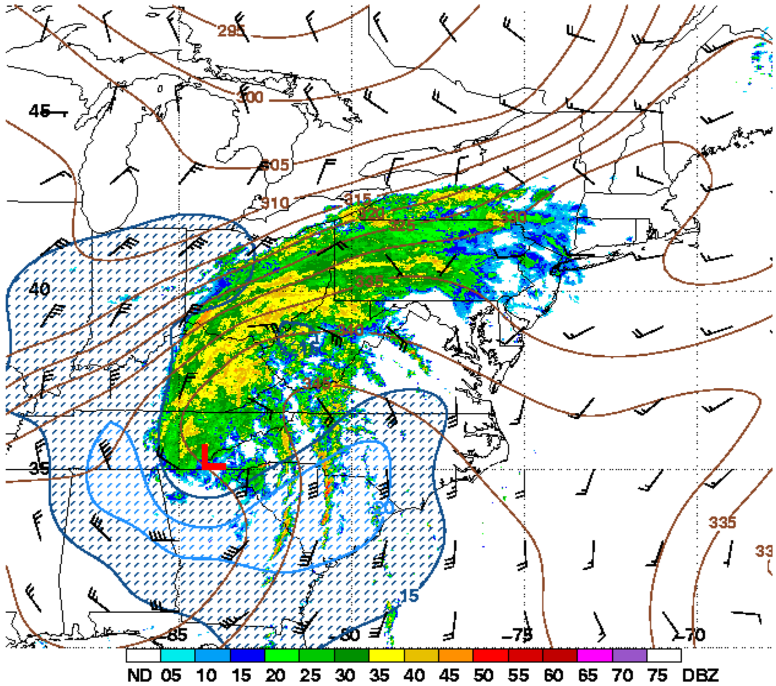

Fig. 3.8. Same as in Fig. 3.7 except at 1200 UTC 17 September 2004.

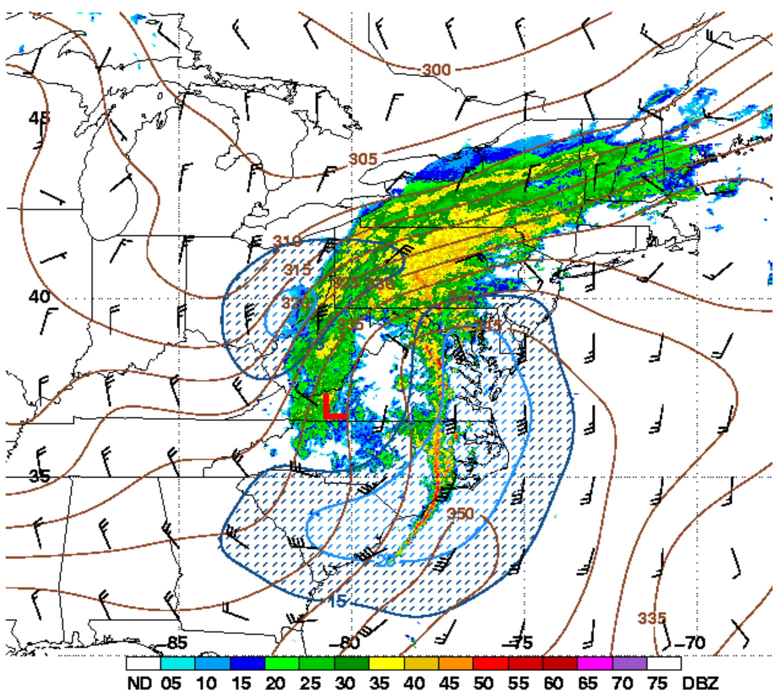

Fig. 3.9. Same as in Fig. 3.7 except at 0000 UTC 18 September 2004.

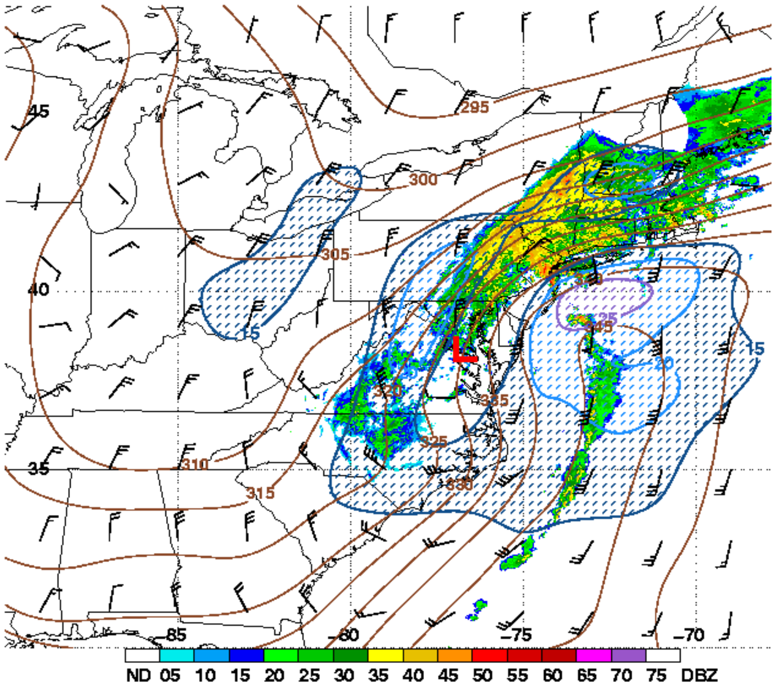

Fig. 3.10. Same as in Fig. 3.7 except at 1200 UTC 18 September 2004.

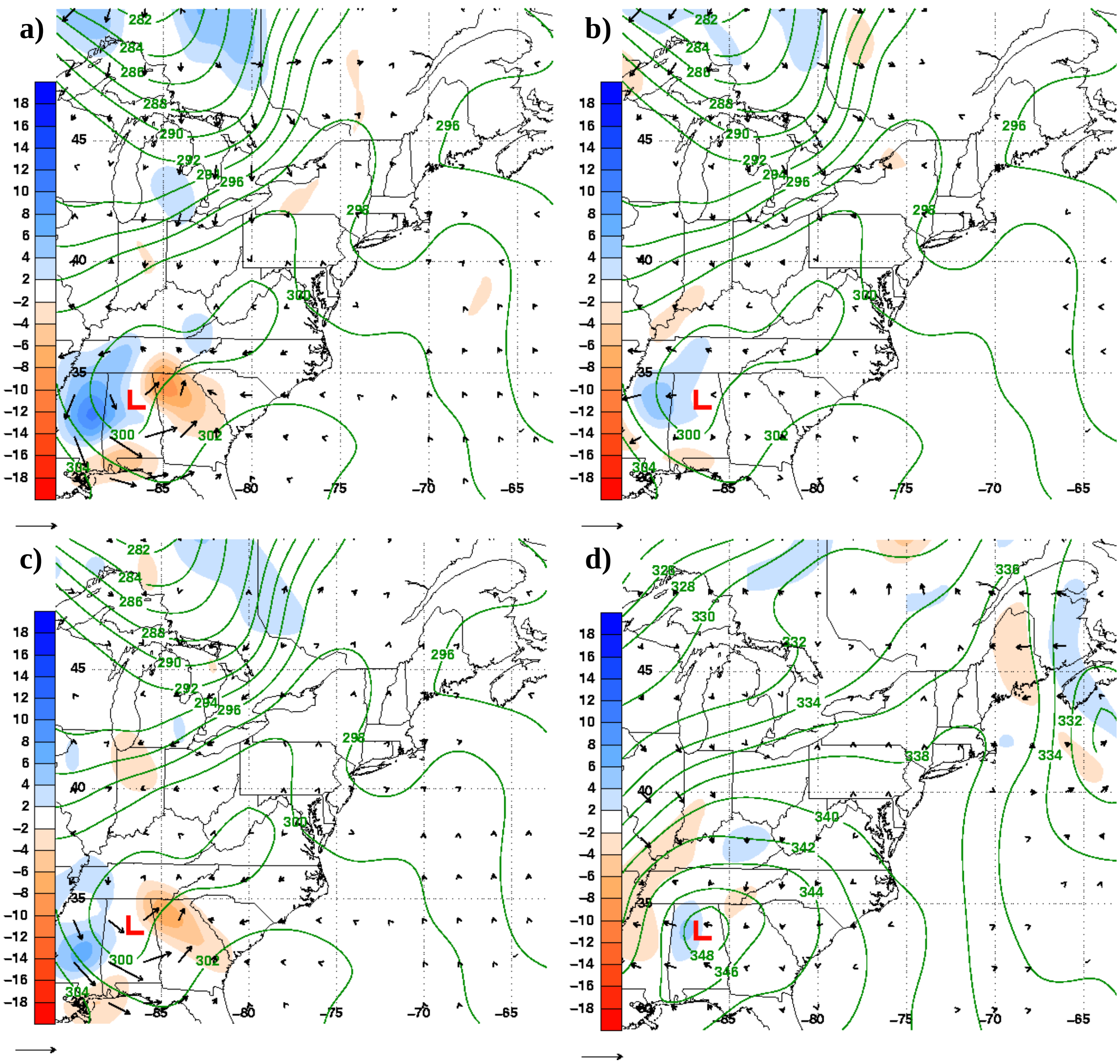

Fig. 3.11. Q vector diagnostics at 0000 UTC 17 September 2004. (a) 925-hPa Q vectors in units of K m^{-1} s^{-1} beginning at 2.5×10^{-11} K m^{-1} s^{-1}, Q vector divergence–convergence shaded in cool–warm colors every 2×10^{-15} K m^{-2} s^{-1}, and isentropes contoured in green every 2 K. The magnitude of the reference Q vector is 1×10^{-9} K m^{-1} s^{-1}. (b) Same as in (a) except for Q_n. (c) Same as in (a) except for Q_s. (d) Same as in (a) except for Q_n with analysis at 300 hPa.

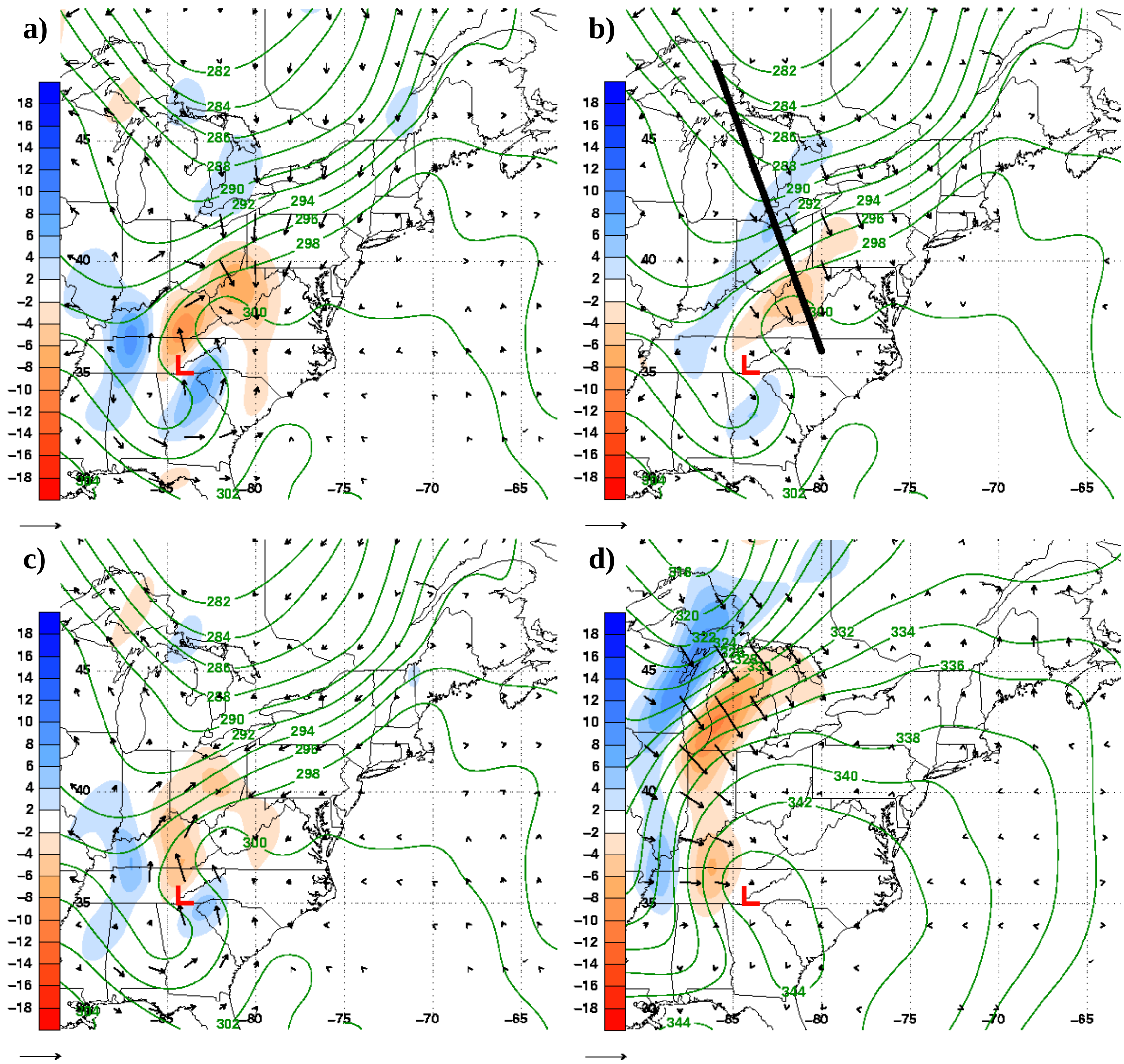

Fig. 3.12. Same as in Fig. 3.11 except at 1200 UTC 17 September 2004 with cross-section orientation for Fig. 3.15 shown in (b).

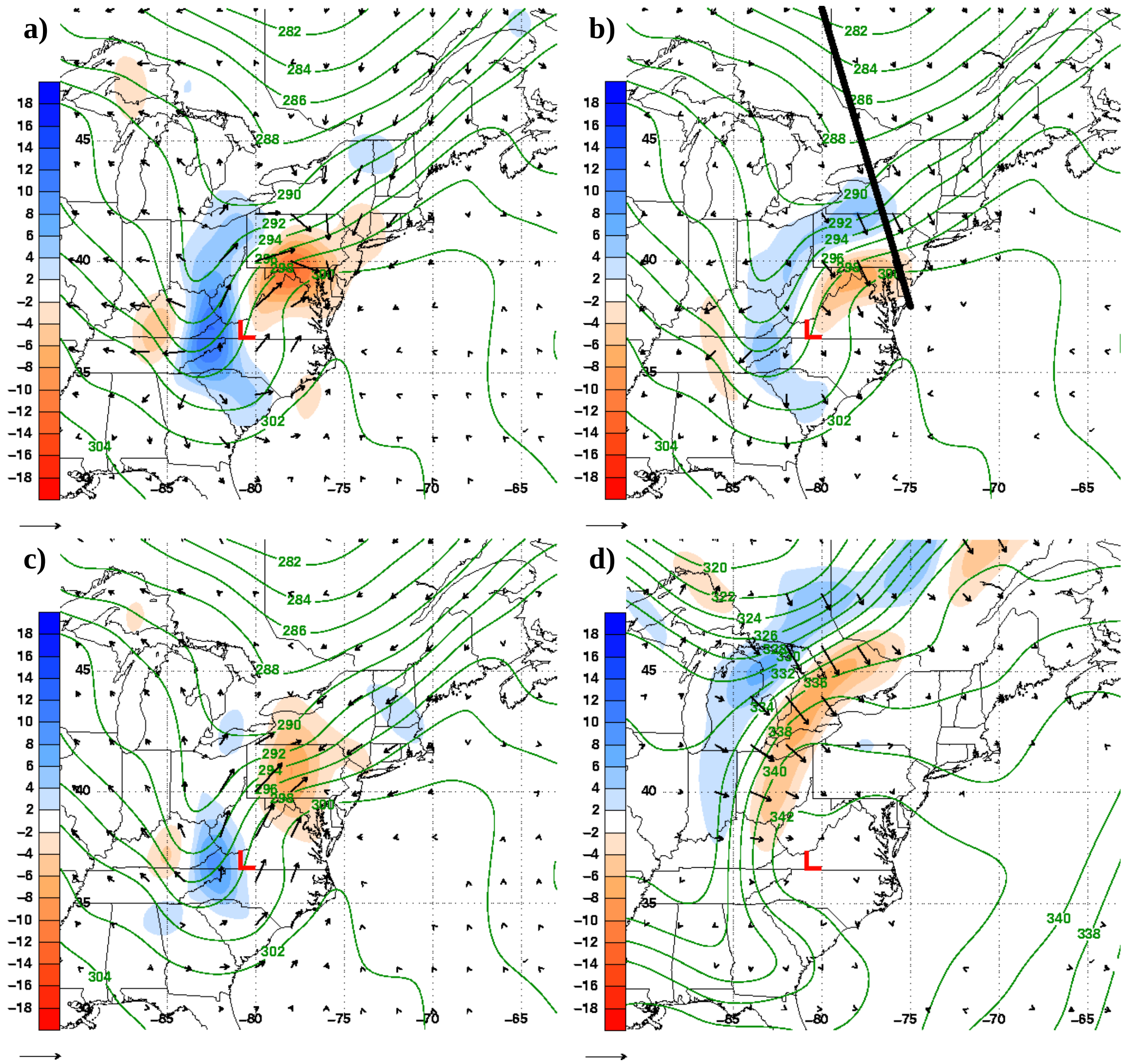

Fig. 3.13. Same as in Fig. 3.11 except at 0000 UTC 18 September 2004 with cross-section orientation for Fig. 3.16 shown in (b).

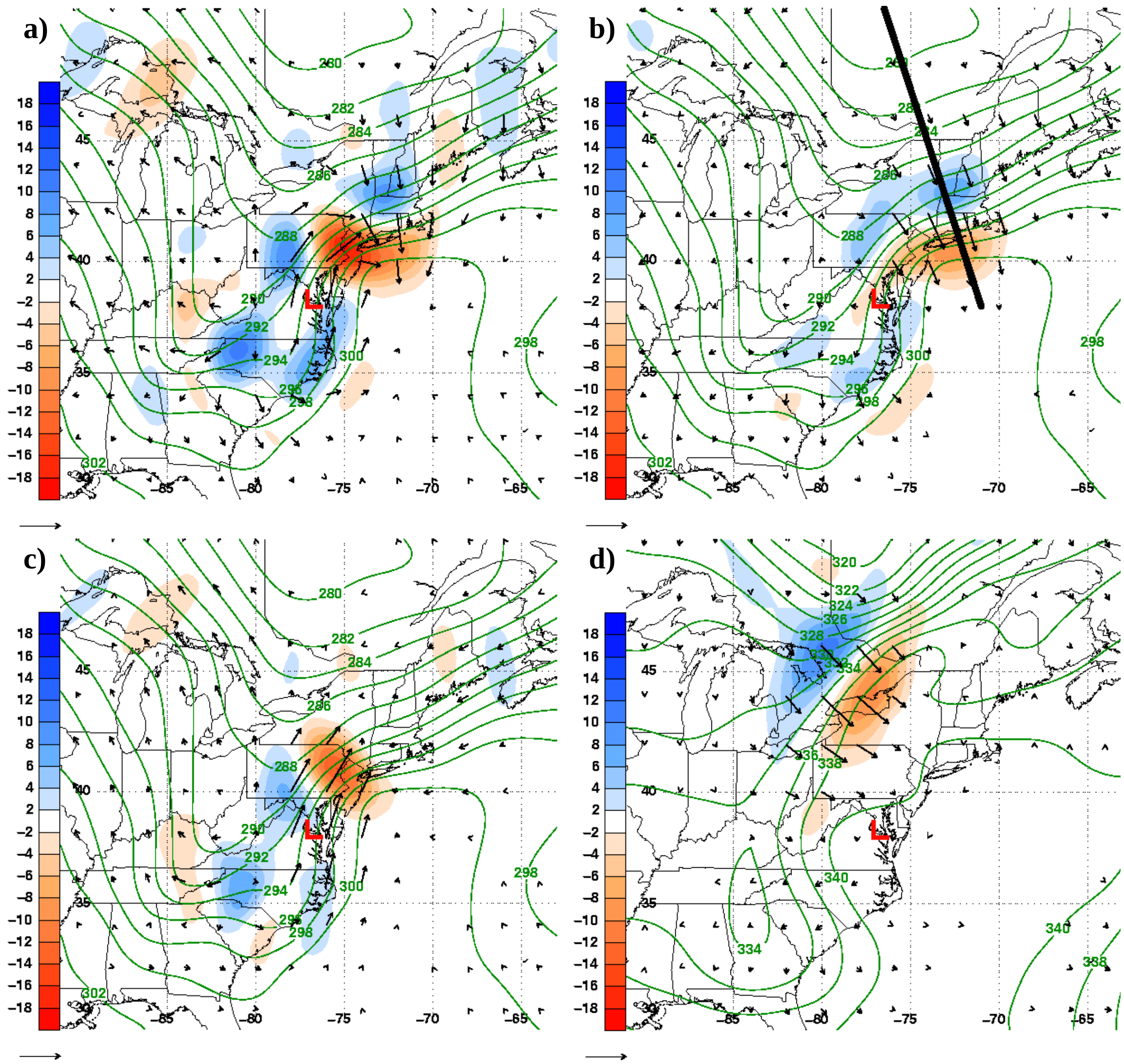

Fig. 3.14. Same as in Fig. 3.11 except at 1200 UTC 18 September 2004 with cross-section orientation for Fig. 3.17 shown in (b).

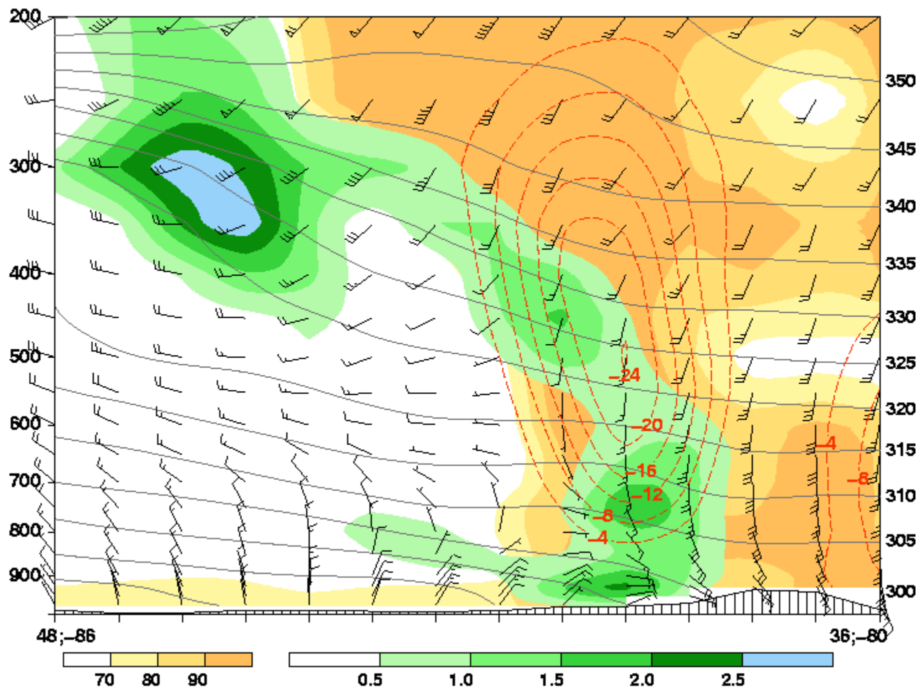

Fig. 3.15. Cross section taken quasi-parallel to the 925–500-hPa layer-averaged potential temperature gradient at 1200 UTC 17 September 2004 with cross-section orientation shown in Fig. 3.12b. Cross section includes relative humidity shaded every 10% above 70% (color scale on the lower left), two-dimensional frontogenesis shaded every 0.5 K $(100\ \mathrm{km})^{-1}$ $(3\ \mathrm{h})^{-1}$ (color scale on the lower right), wind barbs (1 pennant = 25 m s^{-1}, 1 full wind barb = 5 m s^{-1}, 1 half wind barb = 2.5 m s^{-1}), isentropes contoured in gray every 5 K, and vertical velocity dashed contoured in red every −4 μb s^{-1} starting at −4 μb s^{-1}.

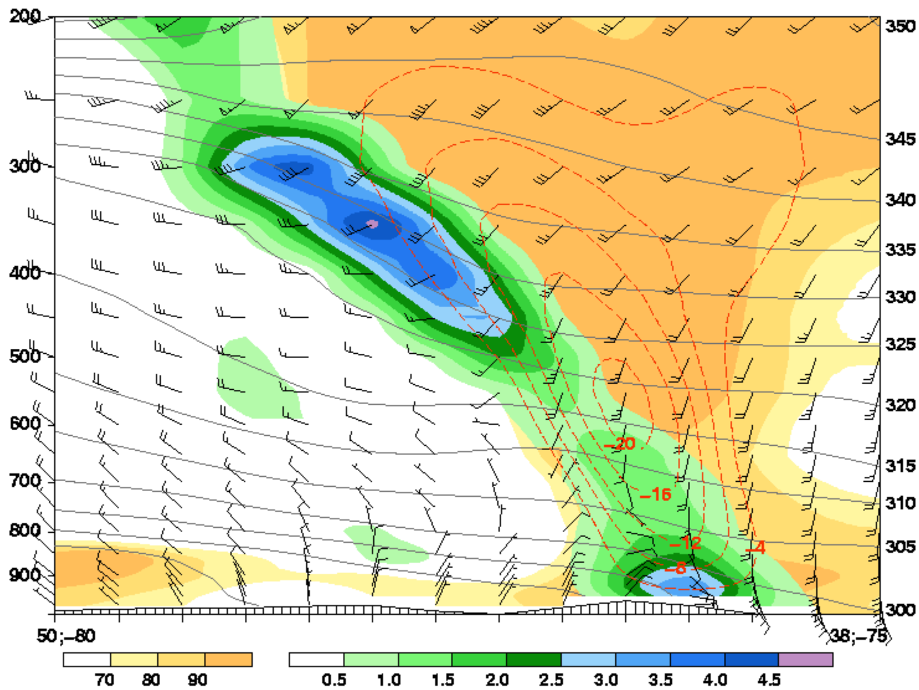

Fig. 3.16. Same as in Fig. 3.15 except at 0000 UTC 18 September 2004 with cross-section orientation shown in Fig. 3.13b.

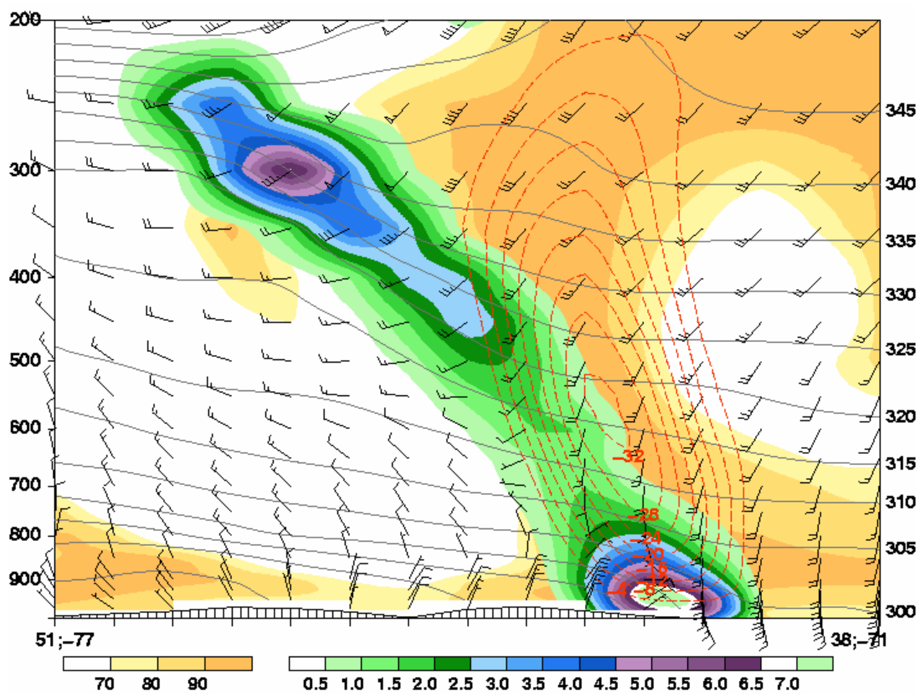

Fig. 3.17. Same as in Fig. 3.15 except at 1200 UTC 18 September 2004 with cross-section orientation shown in Fig. 3.14b.

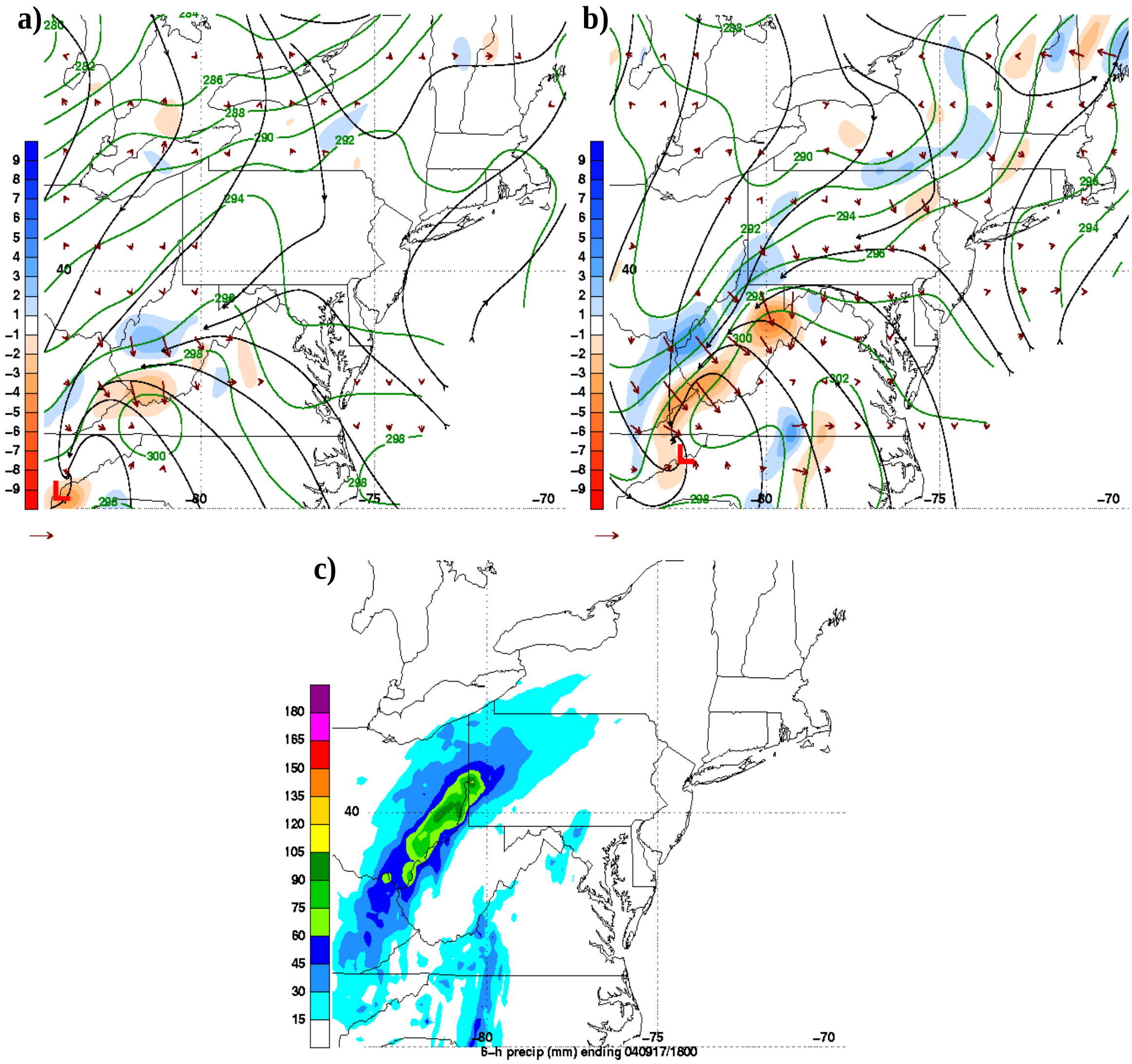

Fig. 3.18. (a) Surface analyses at 1200 UTC 17 September 2004 of F_n vectors in units of K m^{-1} s^{-1} beginning at 1×10^{-10} K m^{-1} s^{-1}, F_n vector divergence–convergence shaded in cool–warm colors every 1×10^{-14} K m^{-2} s^{-1}, isentropes contoured in green every 2 K, and streamlines contoured in black. (b) Same as in (a) except at 1800 UTC 17 September 2004. (c) Accumulated precipitation (shaded every 15 mm) from the NPVU QPE dataset for the 6-h period ending 1800 UTC 17 September 2004.

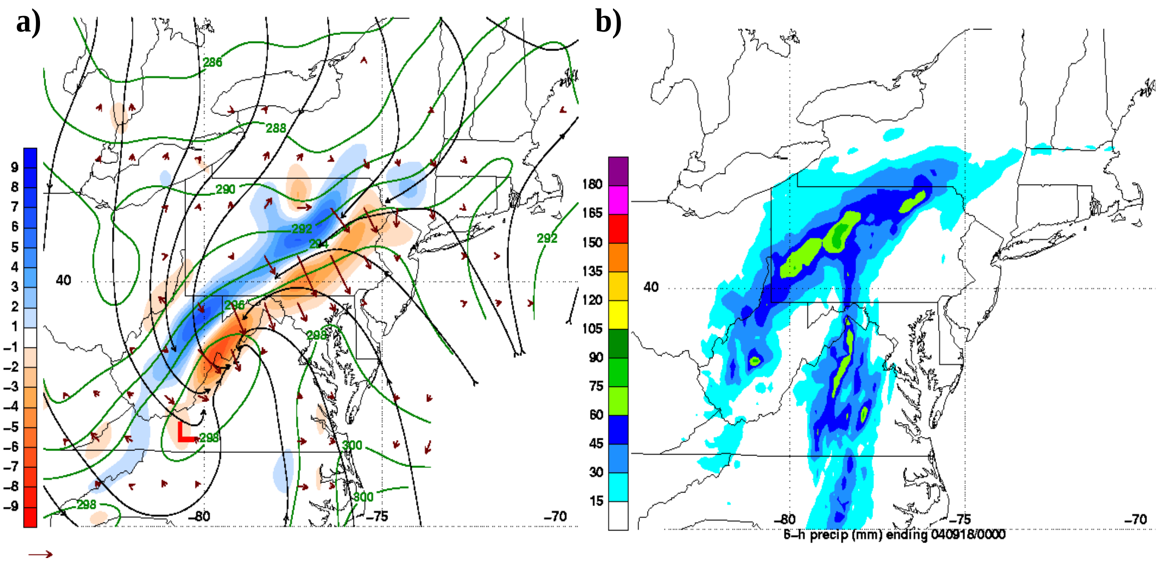

Fig. 3.19. (a) Same as in Fig. 3.18a except at 0000 UTC 18 September 2004. (b) Same as in Fig. 3.18c except ending at 0000 UTC 18 September 2004.

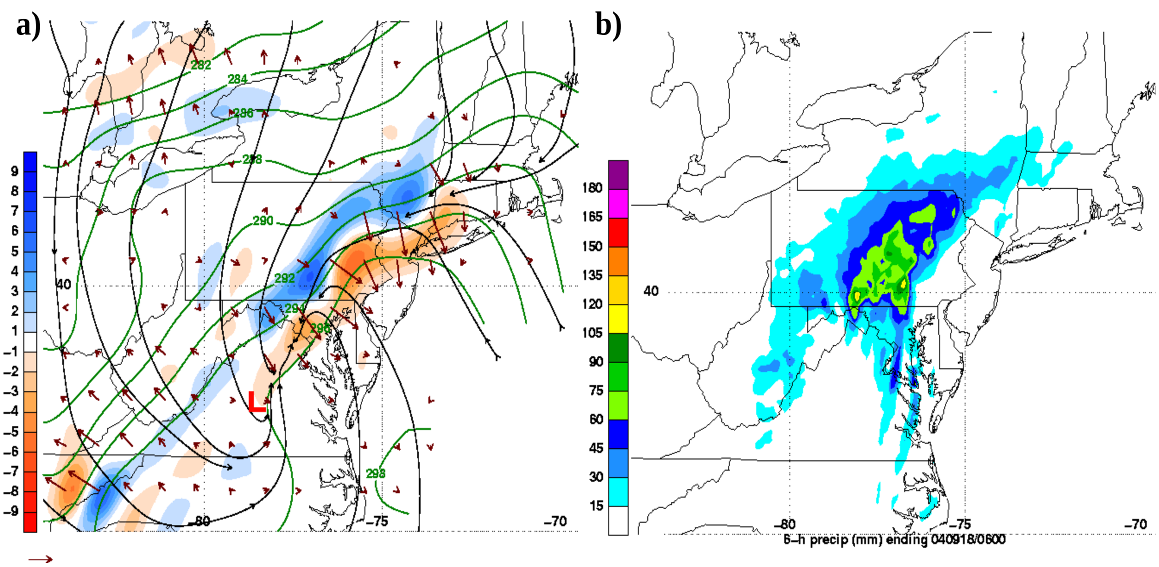

Fig. 3.20. (a) Same as in Fig. 3.18a except at 0600 UTC 18 September 2004. (b) Same as in Fig. 3.18c except ending at 0600 UTC 18 September 2004.

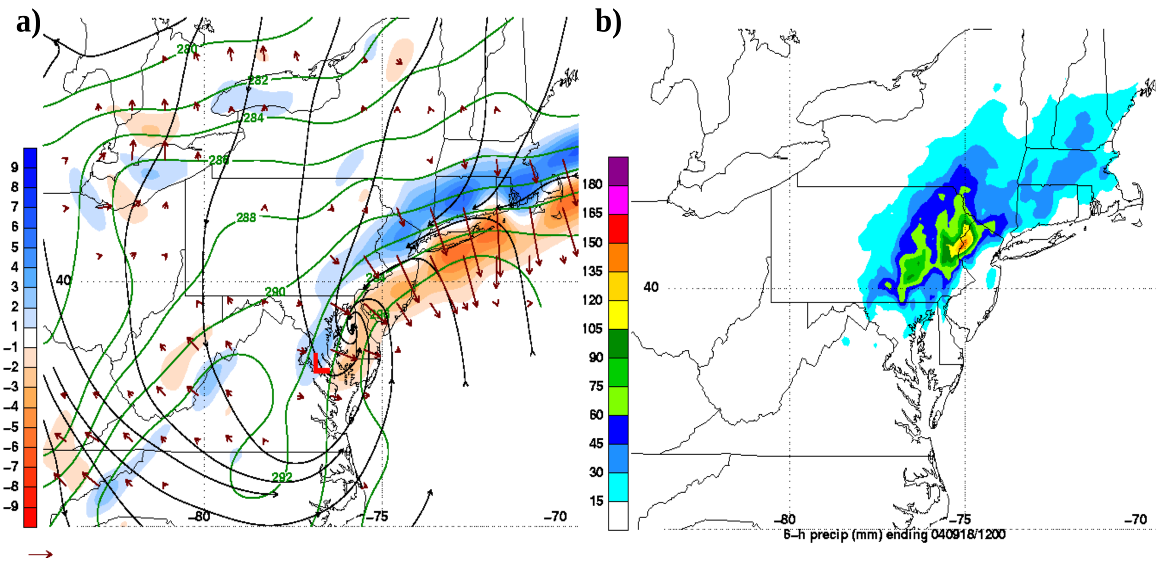

Fig. 3.21. (a) Same as in Fig. 3.18a except at 1200 UTC 18 September 2004. (b) Same as in Fig. 3.18c except ending at 1200 UTC 18 September 2004.

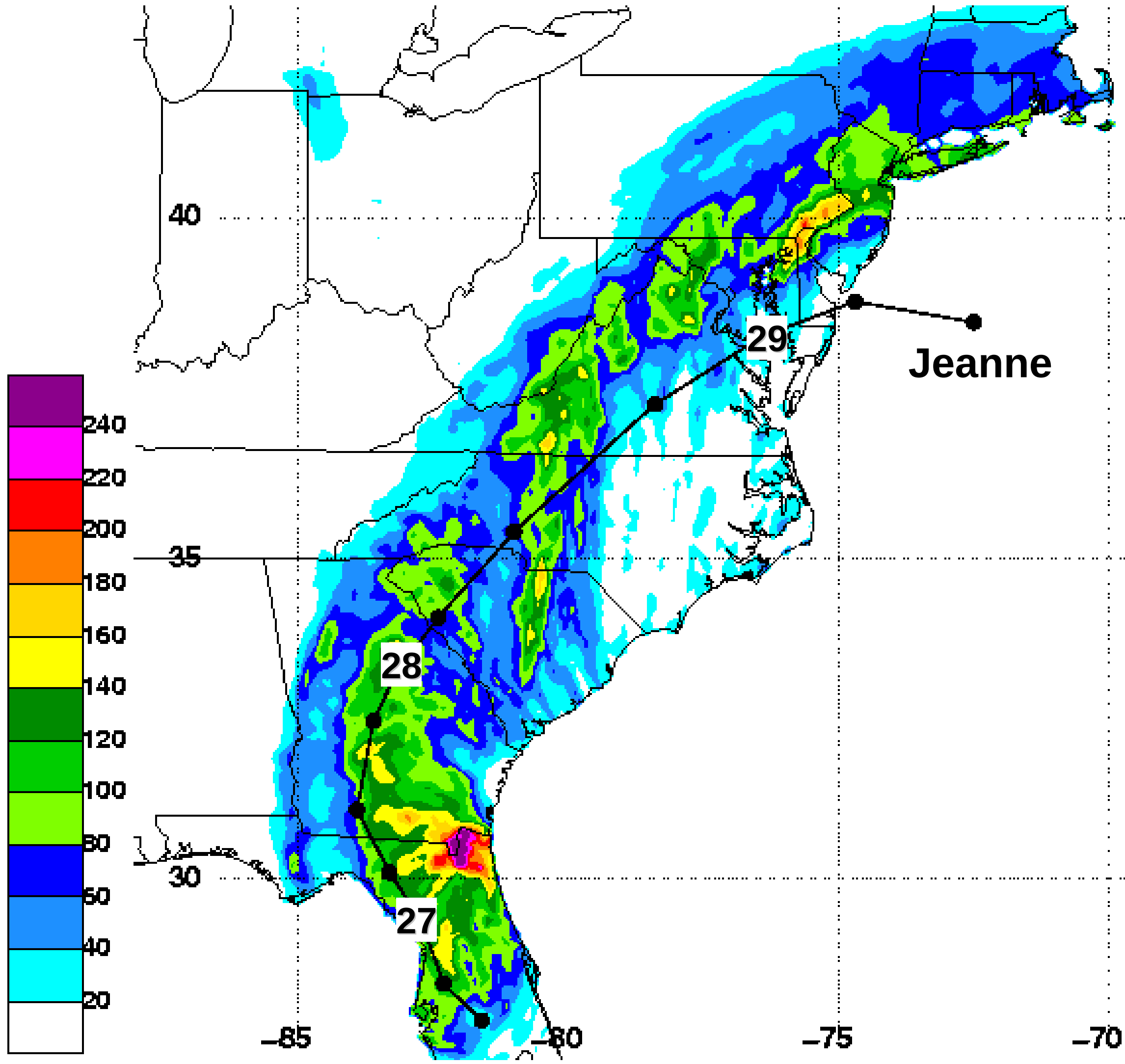

Fig. 3.22. Same as in Fig. 3.3 except from Jeanne for 1200 UTC 26–1200 UTC 29 September 2004.

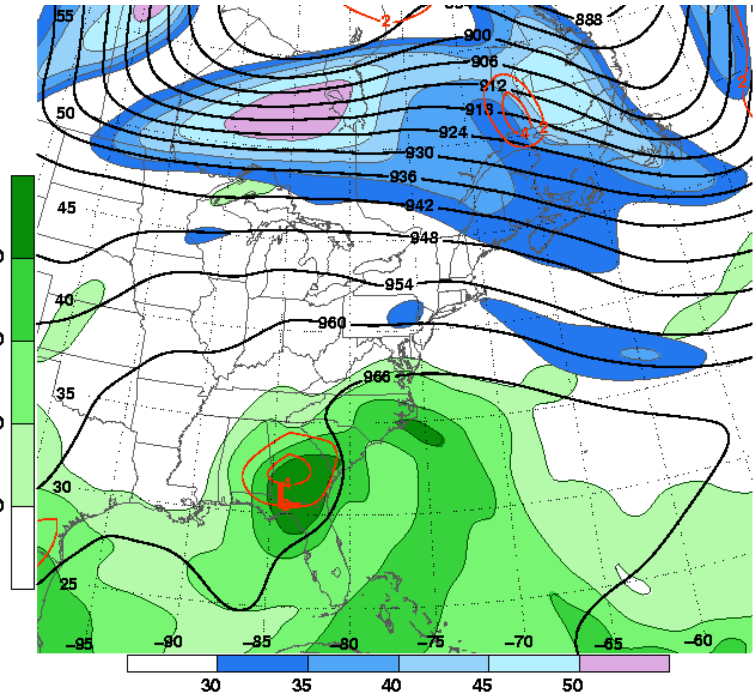

Fig. 3.23. Same as in Fig. 3.4 except at 1200 UTC 27 September 2004.

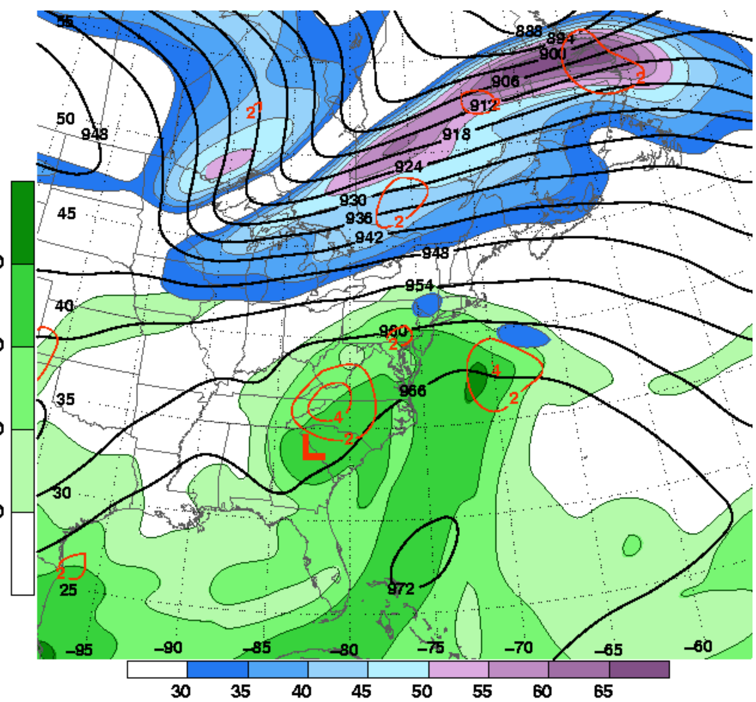

Fig. 3.24. Same as in Fig. 3.4 except at 0600 UTC 28 September 2004.

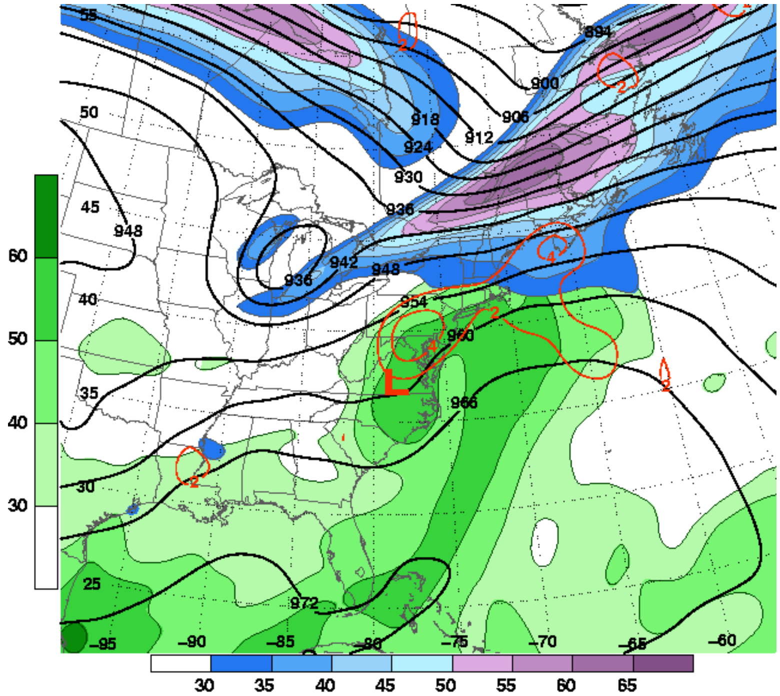

Fig. 3.25. Same as in Fig. 3.4 except at 1800 UTC 28 September 2004.

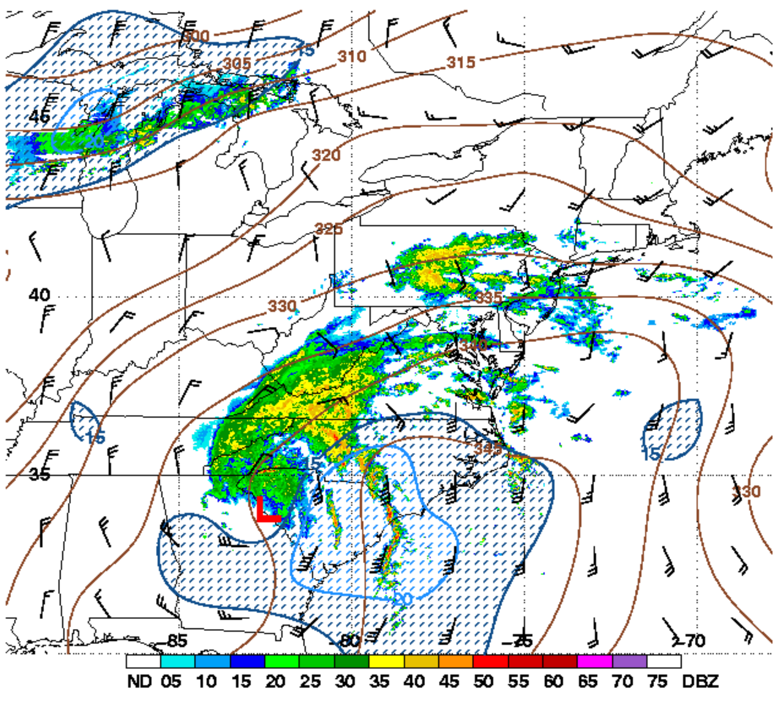

Fig. 3.26. Same as in Fig. 3.7 except at 0600 UTC 28 September 2004.

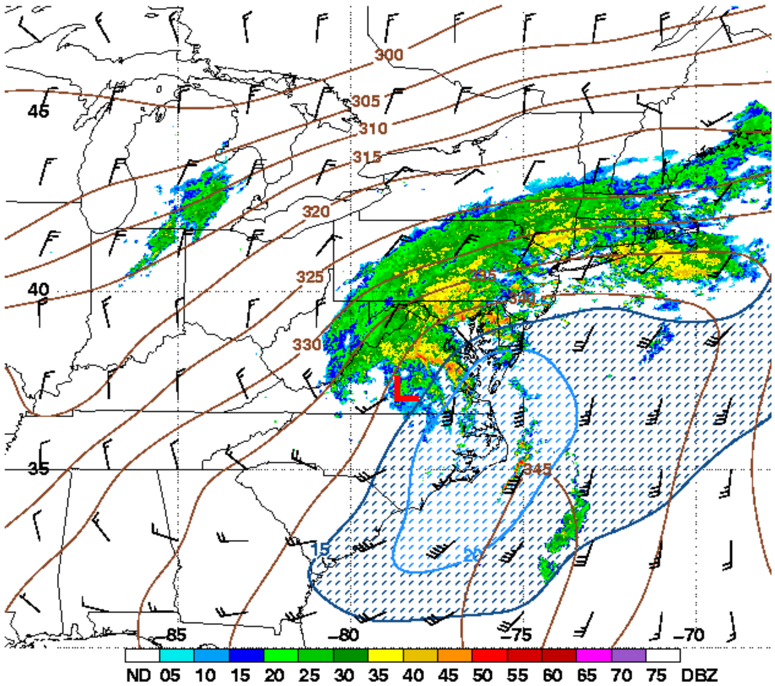

Fig. 3.27. Same as in Fig. 3.7 except at 1800 UTC 28 September 2004.

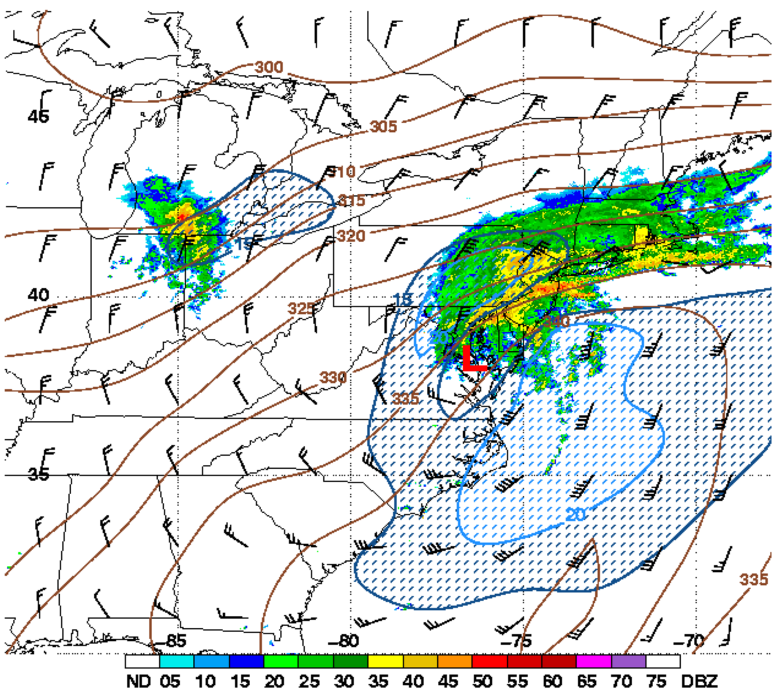

Fig. 3.28. Same as in Fig. 3.7 except at 0000 UTC 29 September 2004.

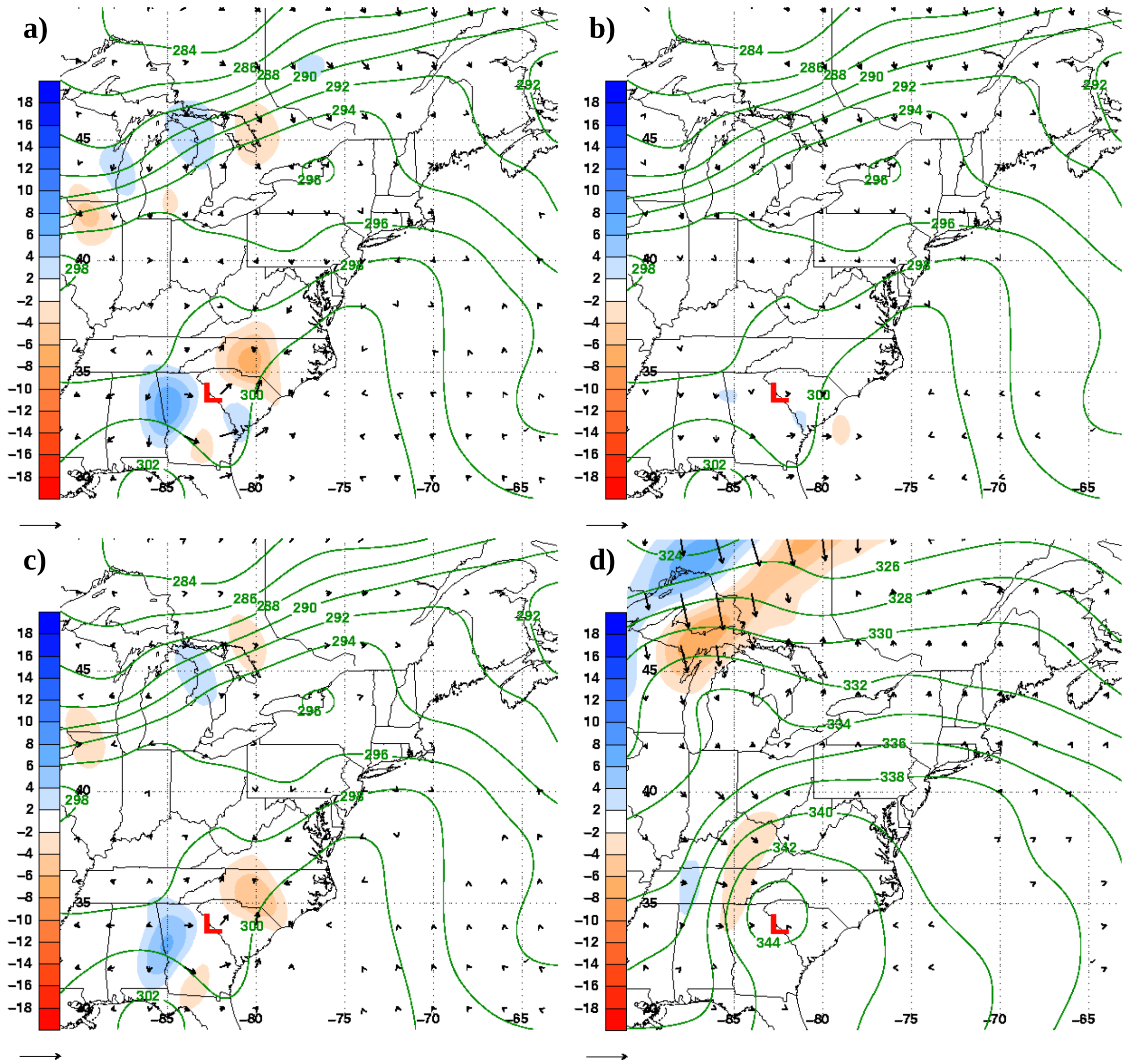

Fig. 3.29. Same as in Fig. 3.11 except at 0600 UTC 28 September 2004.

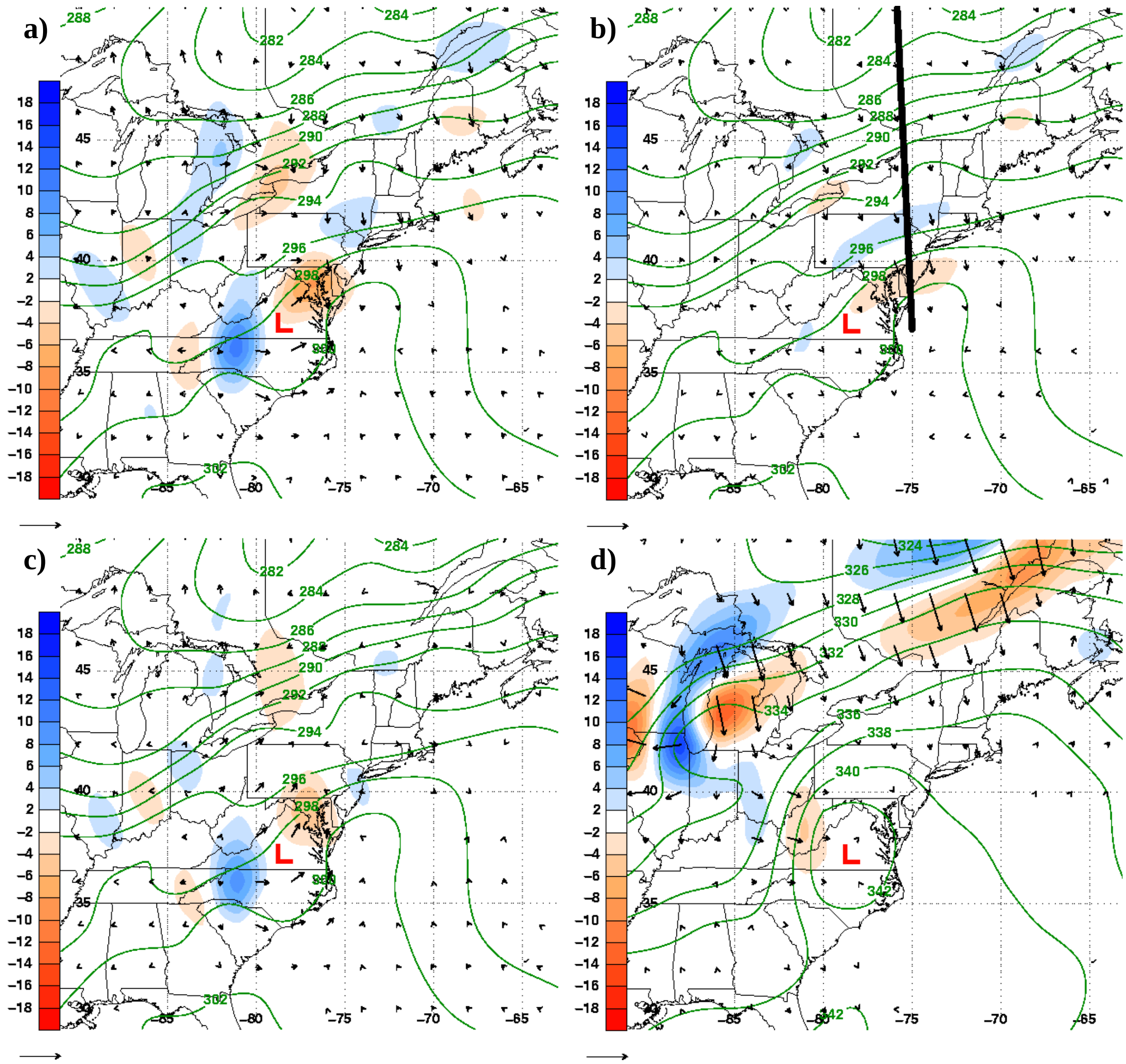

Fig. 3.30. Same as in Fig. 3.11 except at 1800 UTC 28 September 2004 with cross-section orientation for Fig. 3.33 shown in (b).

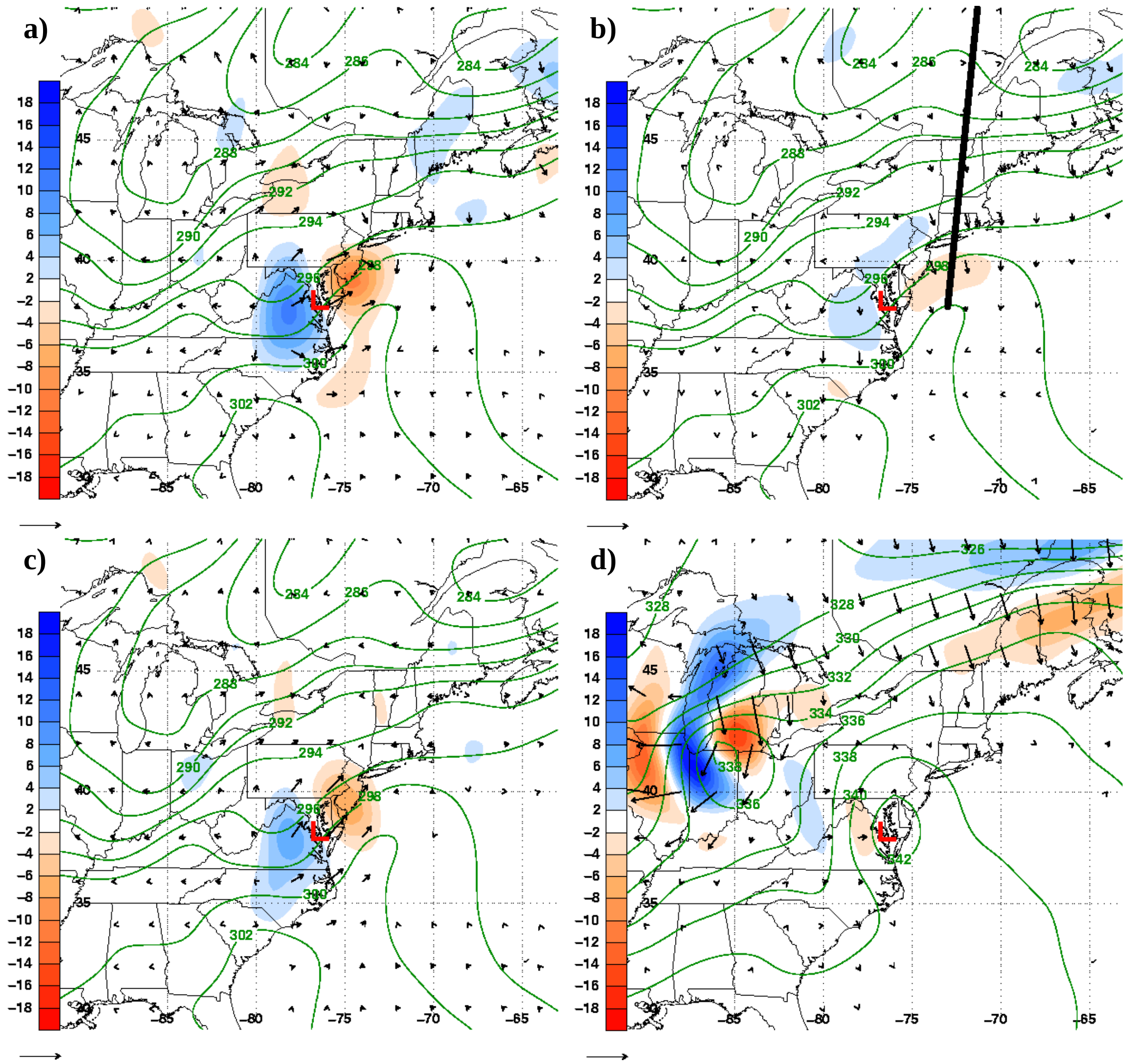

Fig. 3.31. Same as in Fig. 3.11 except at 0000 UTC 29 September 2004 with cross-section orientation for Fig. 3.34 shown in (b).

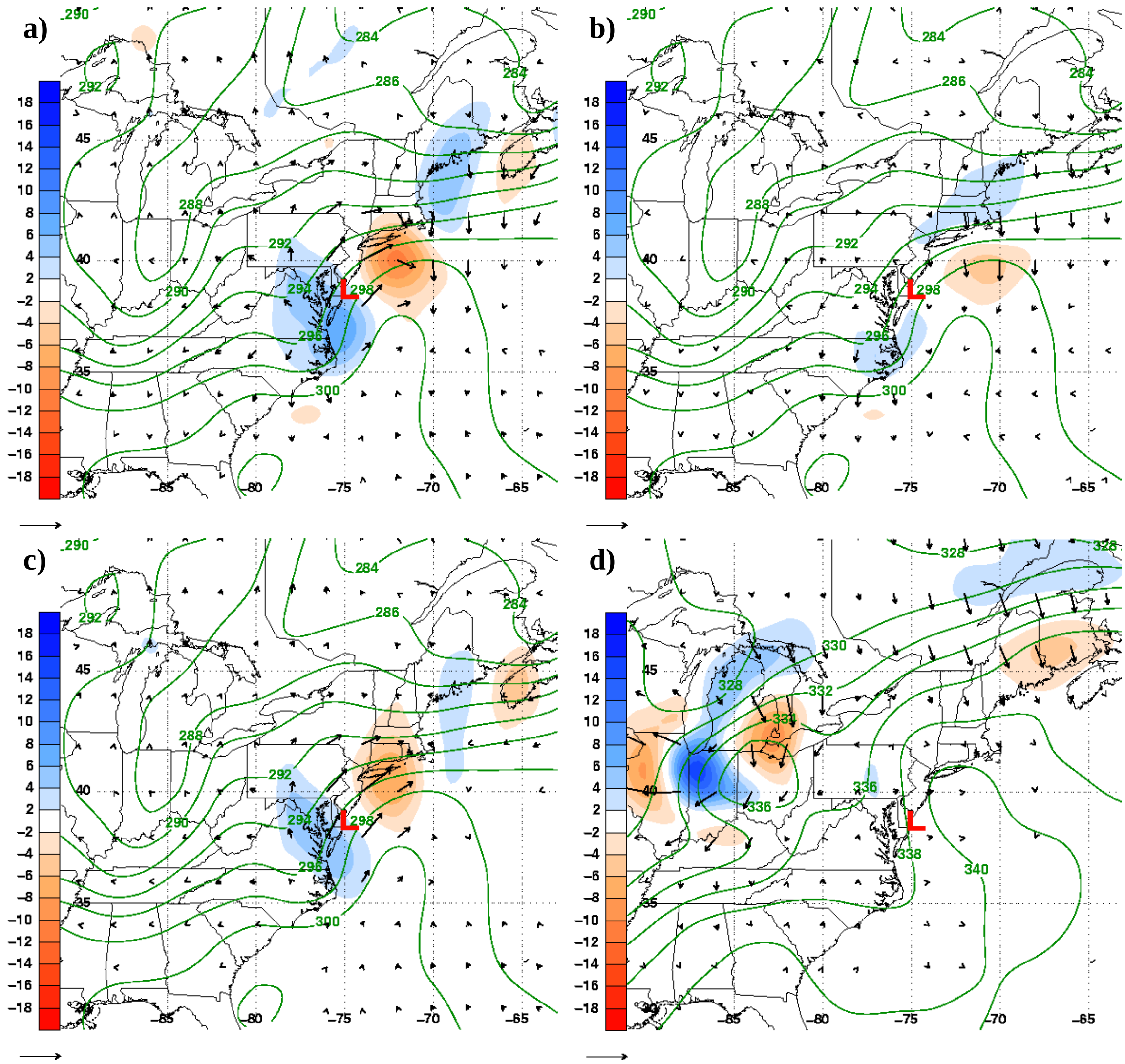

Fig. 3.32. Same as in Fig. 3.11 except at 0600 UTC 29 September 2004.

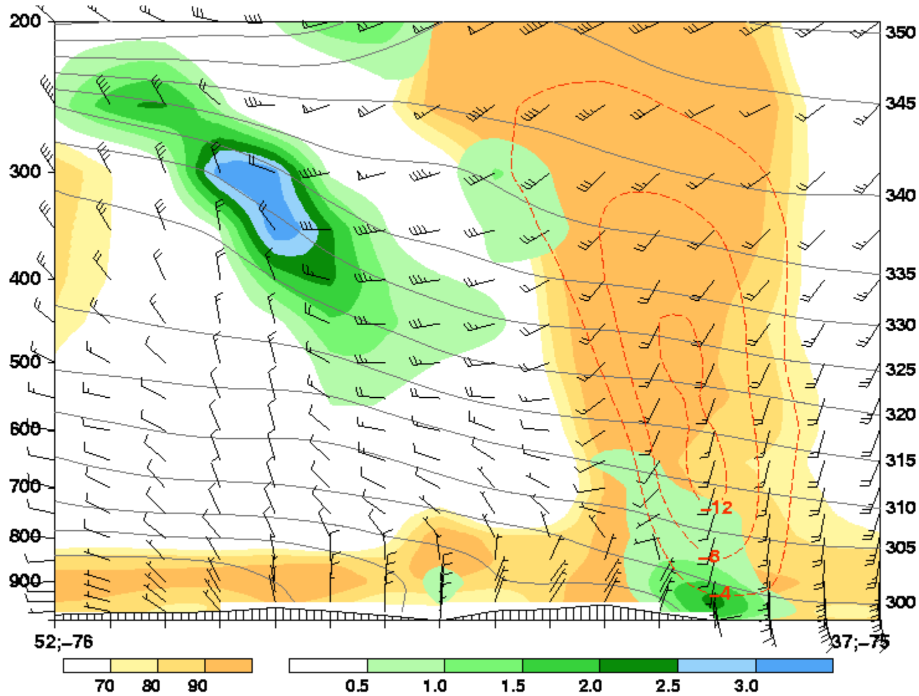

Fig. 3.33. Same as in Fig. 3.15 except at 1800 UTC 28 September 2004 with cross-section orientation shown in Fig. 3.30b.

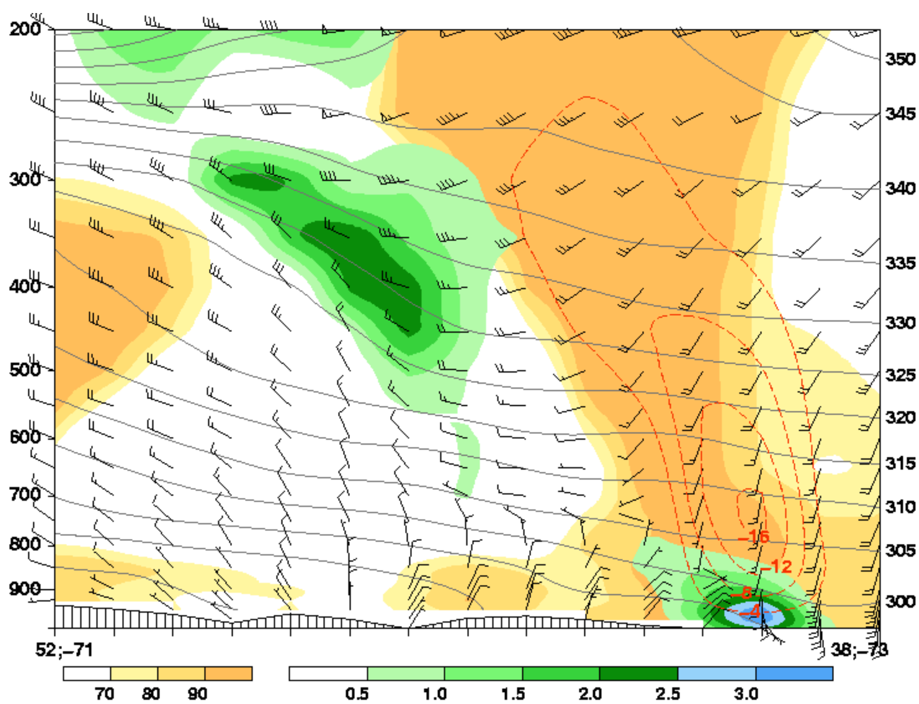

Fig. 3.34. Same as in Fig. 3.15 except at 0000 UTC 29 September 2004 with cross-section orientation shown in Fig. 3.31b.

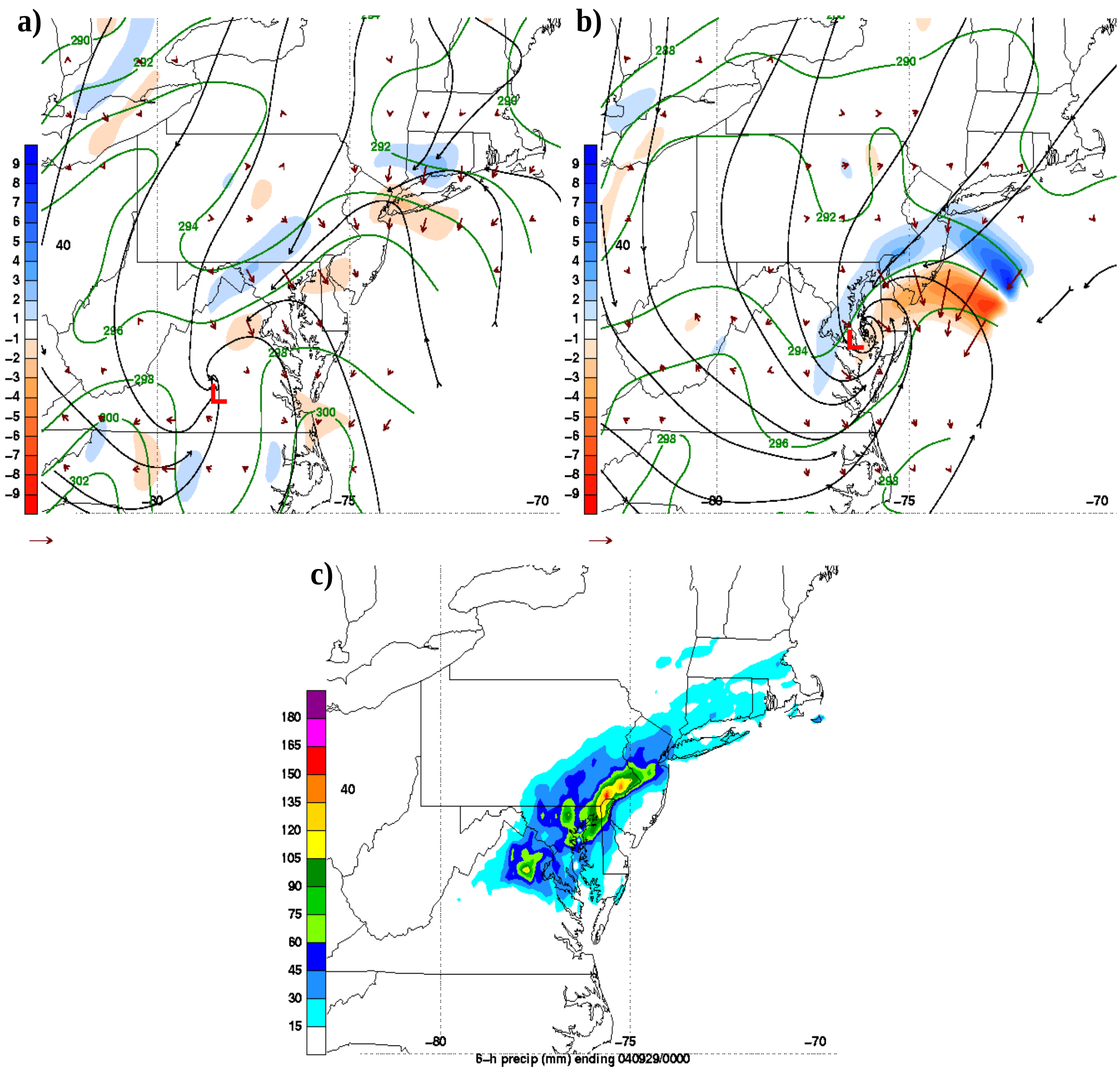

Fig. 3.35. (a) Same as in Fig. 3.18a except at 1800 UTC 28 September 2004. (b) Same as in Fig. 3.18a except at 0000 UTC 29 September 2004. (c) Same as in Fig. 3.18c except ending at 0000 UTC 29 September 2004.

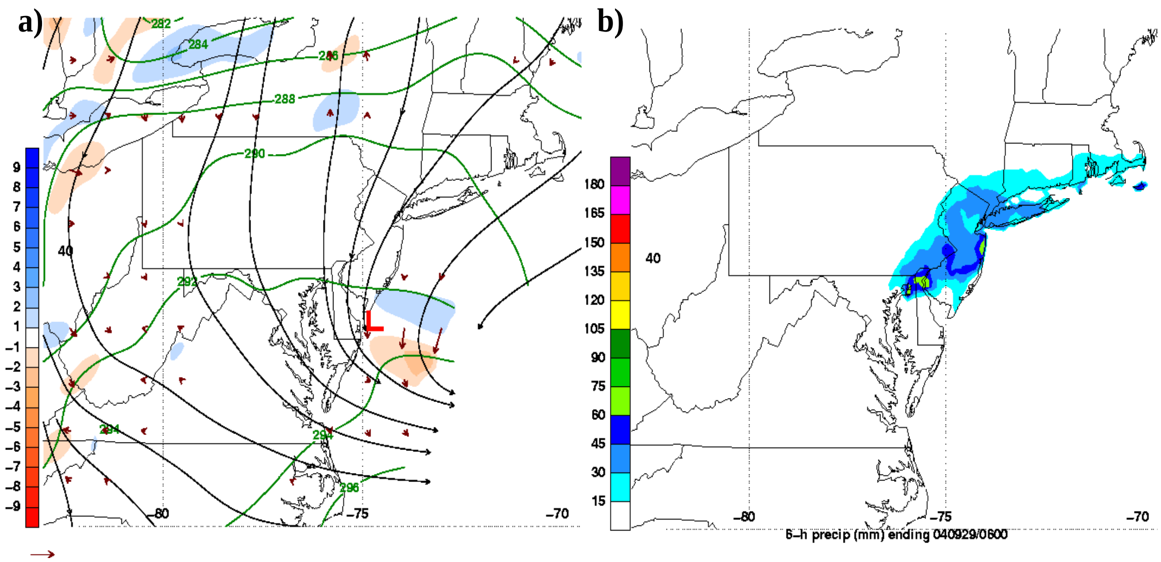

Fig. 3.36. (a) Same as in Fig. 3.18a except at 0600 UTC 29 September 2004. (b) Same as in Fig. 3.18c except ending at 0600 UTC 29 September 2004.

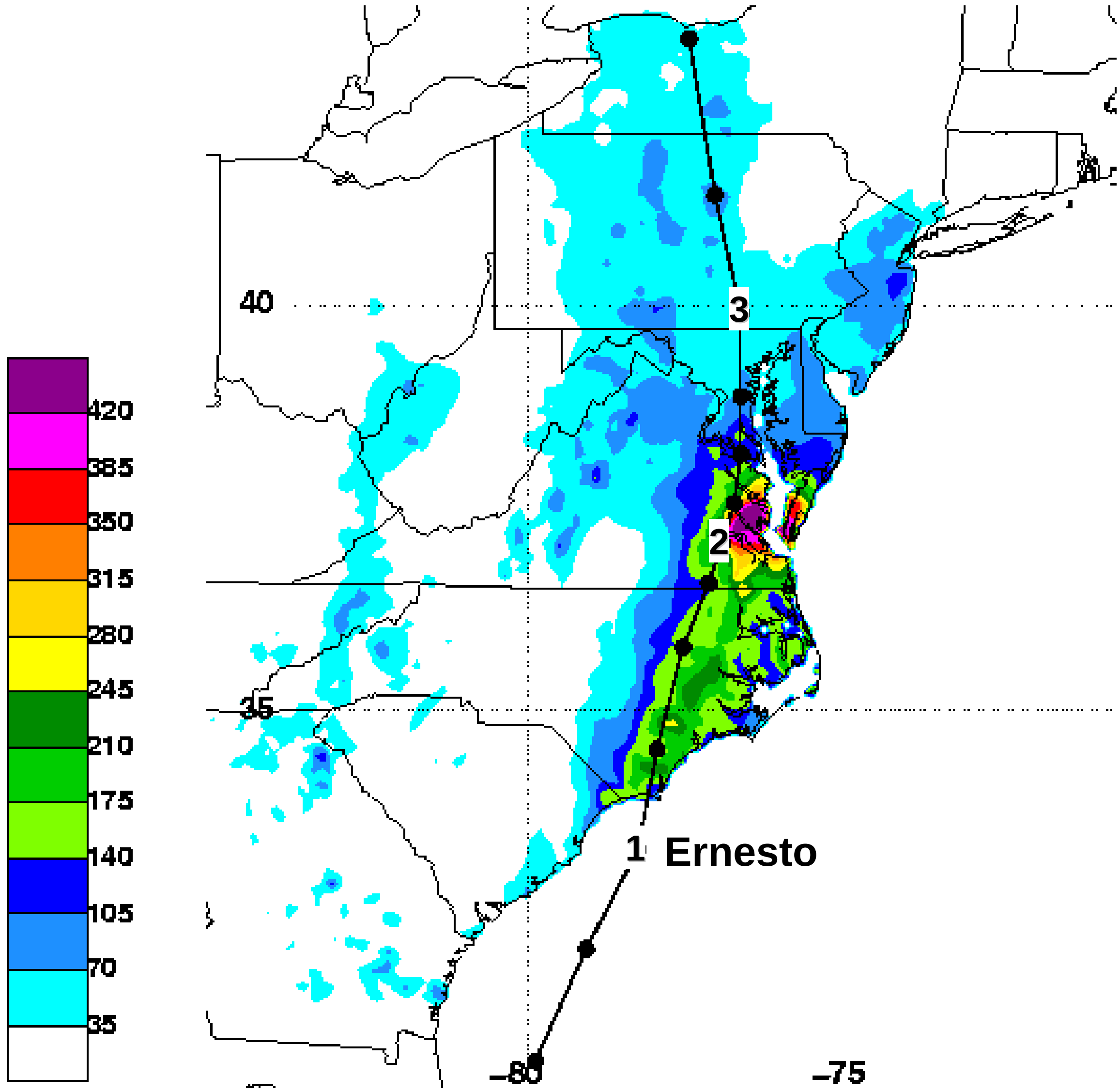

Fig. 3.37. Same as in Fig. 3.3 except with storm total precipitation (shaded every 35 mm) from Ernesto for 1200 UTC 31 August–1200 UTC 3 September 2006.

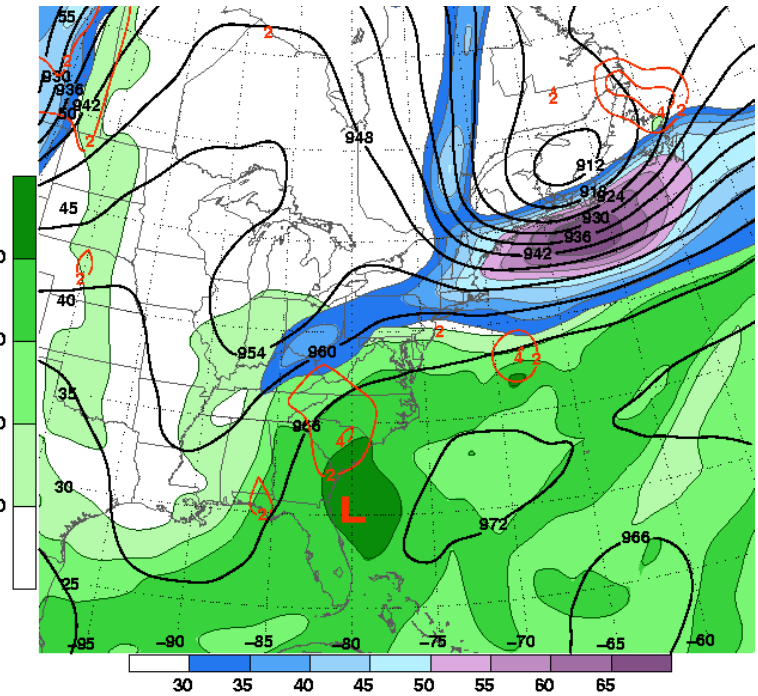

Fig. 3.38. Same as in Fig. 3.4 except at 1200 UTC 31 August 2006.

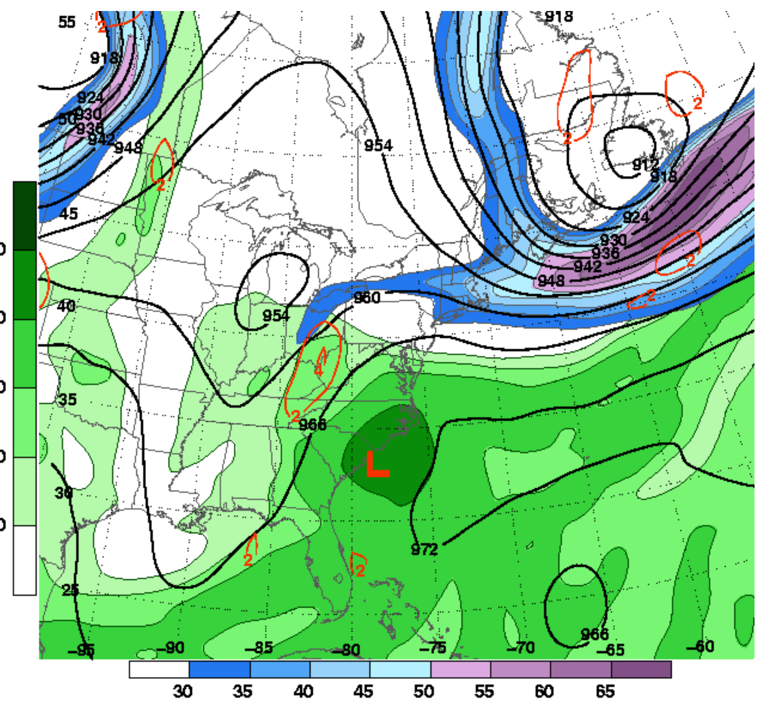

Fig. 3.39. Same as in Fig. 3.4 except at 0000 UTC 1 September 2006.

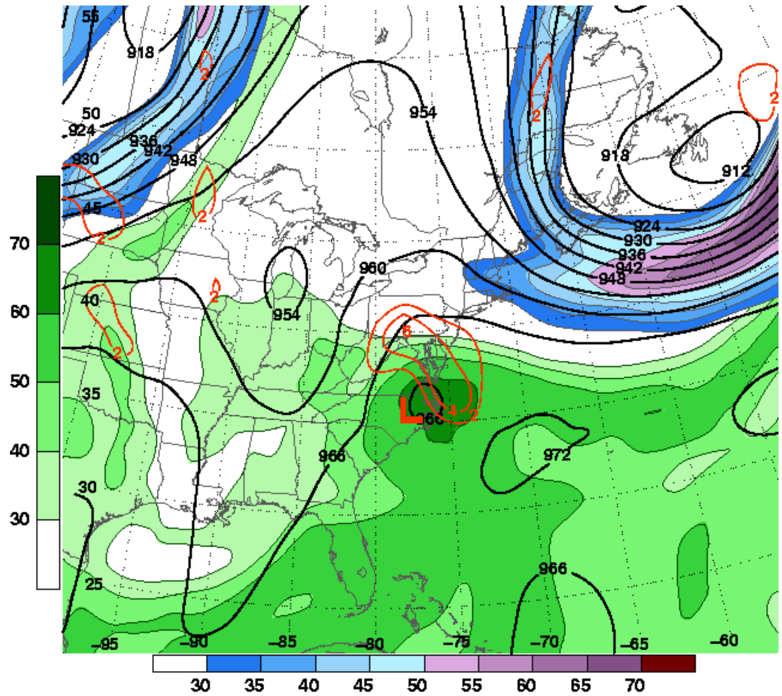

Fig. 3.40. Same as in Fig. 3.4 except at 1200 UTC 1 September 2006.

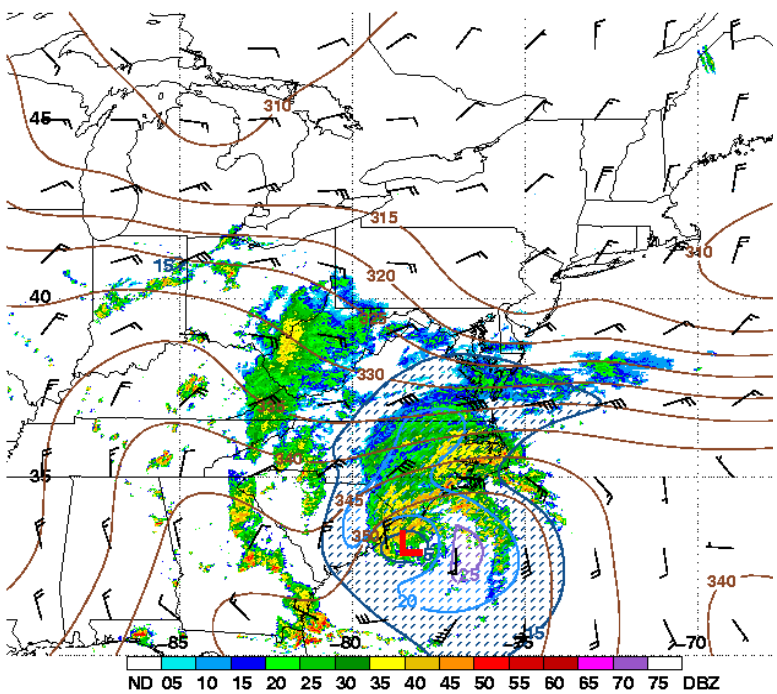

Fig. 3.41. Same as in Fig. 3.7 except at 0000 UTC 1 September 2006.

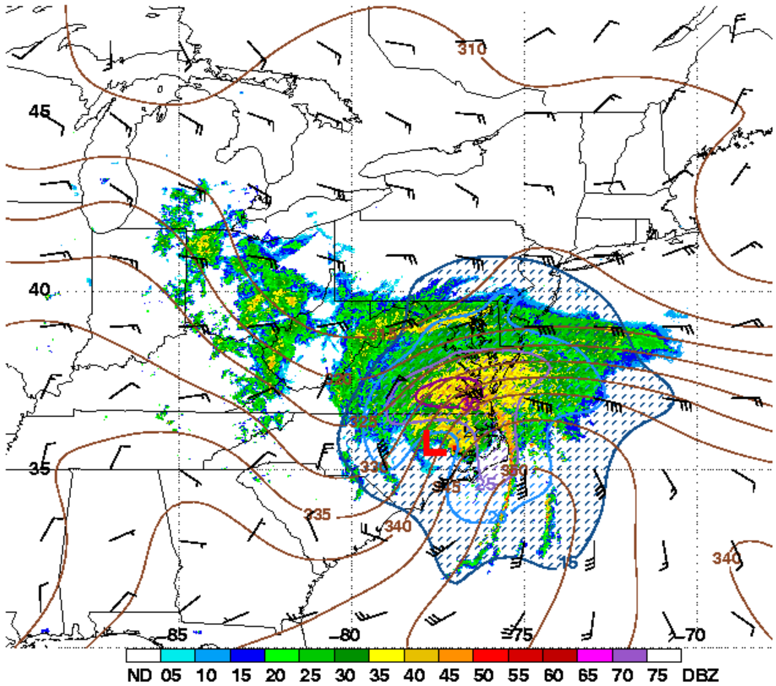

Fig. 3.42. Same as in Fig. 3.7 except at 1200 UTC 1 September 2006.

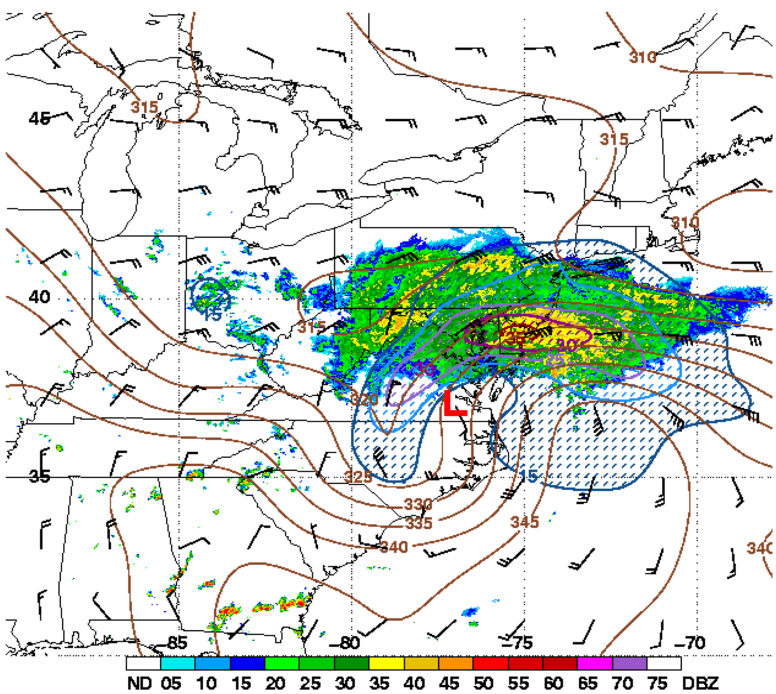

Fig. 3.43. Same as in Fig. 3.7 except at 0000 UTC 2 September 2006.

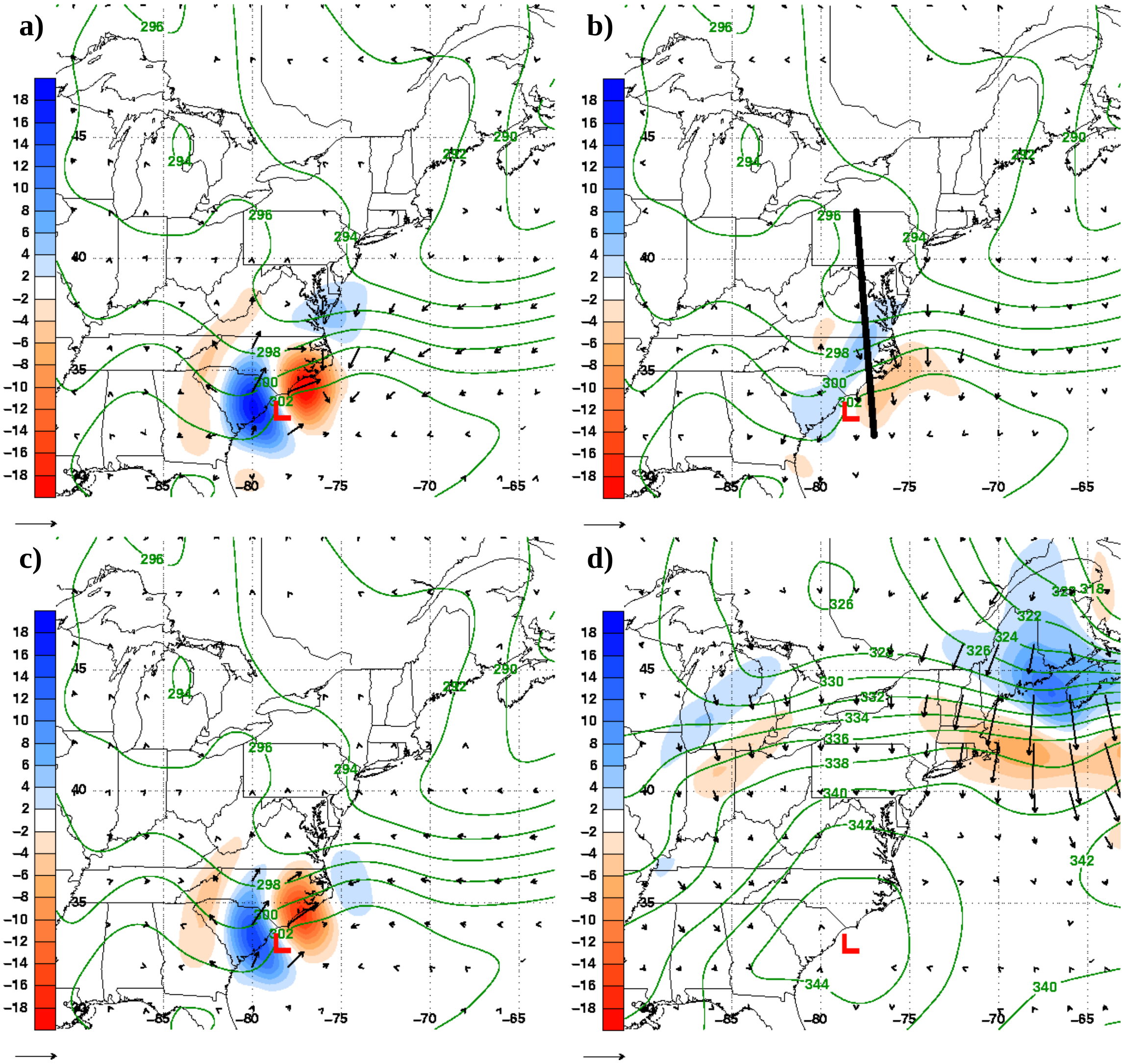

Fig. 3.44. Same as in Fig. 3.11 except at 0000 UTC 1 September 2006 with cross-section orientation for Fig. 3.47 shown in (b).

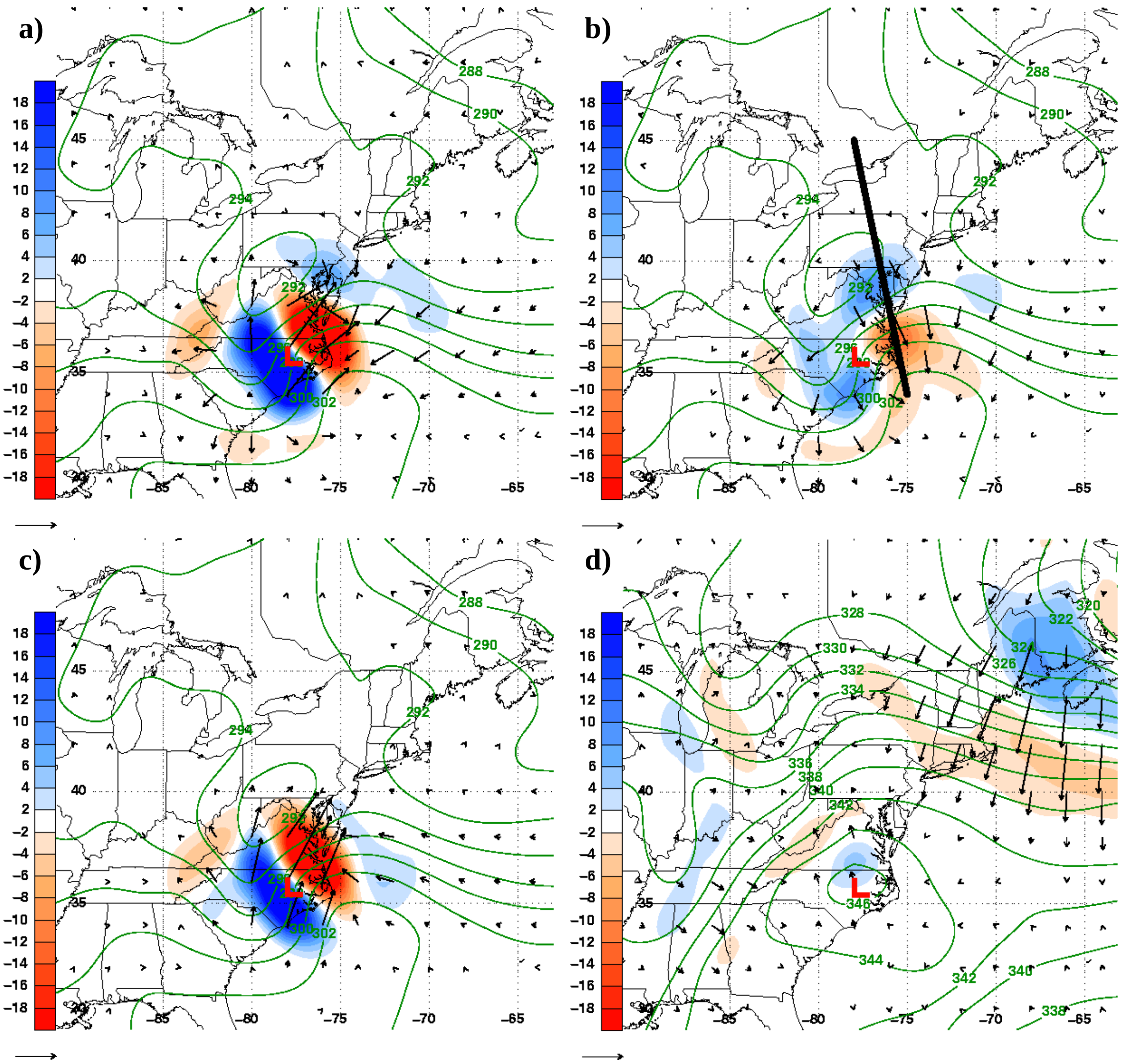

Fig. 3.45. Same as in Fig. 3.11 except at 1200 UTC 1 September 2006 with cross-section orientation for Fig. 3.48 shown in (b).

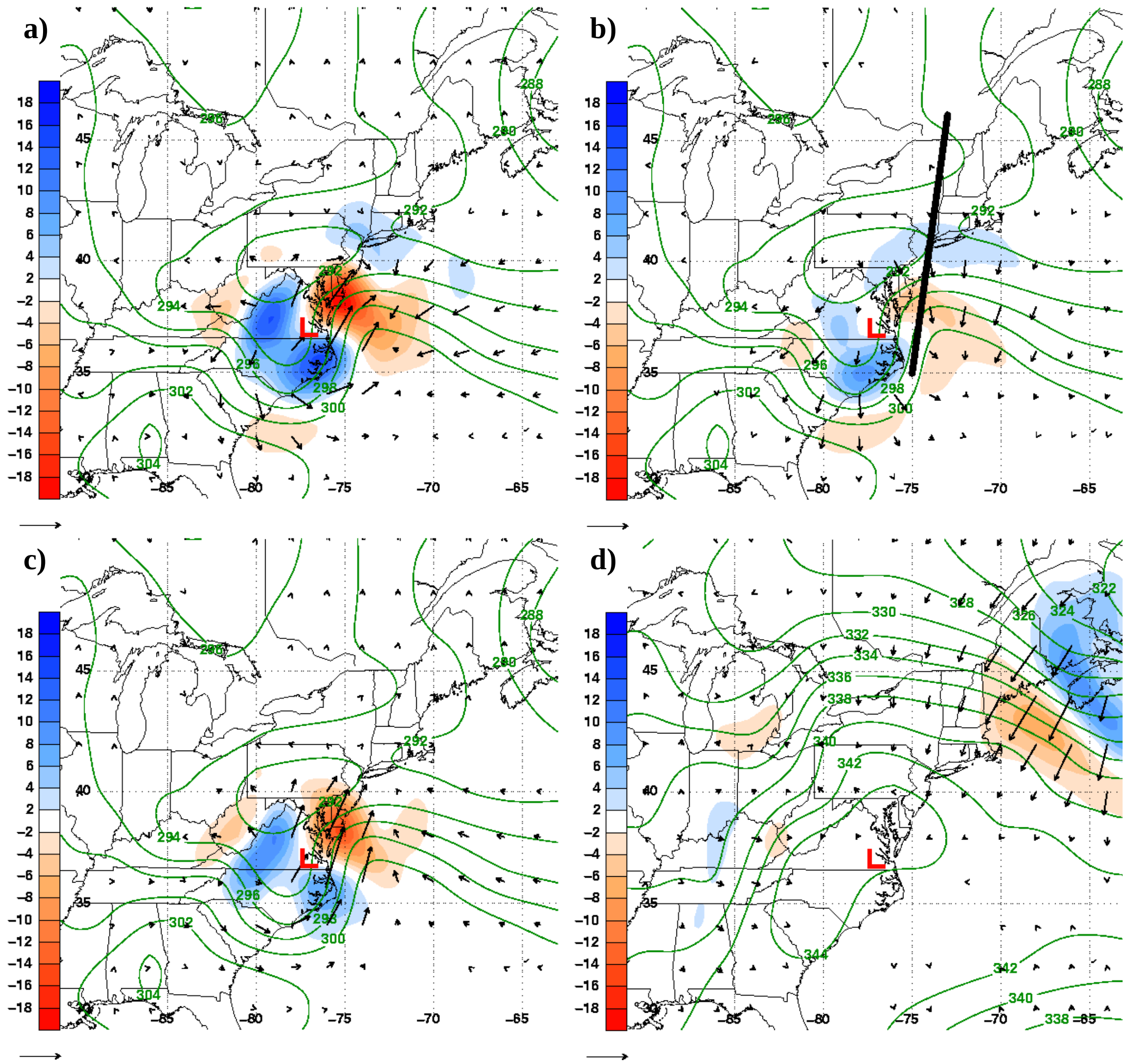

Fig. 3.46. Same as in Fig. 3.11 except at 0000 UTC 2 September 2006 with cross-section orientation for Fig. 3.49 shown in (b).

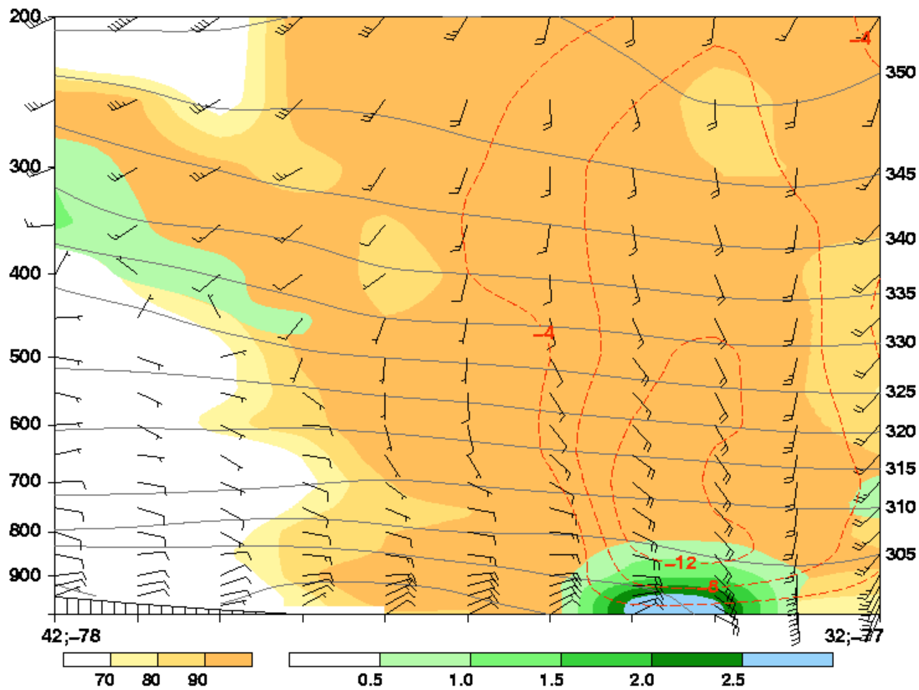

Fig. 3.47. Same as in Fig. 3.15 except at 0000 UTC 1 September 2006 with cross-section orientation shown in Fig. 3.44b.

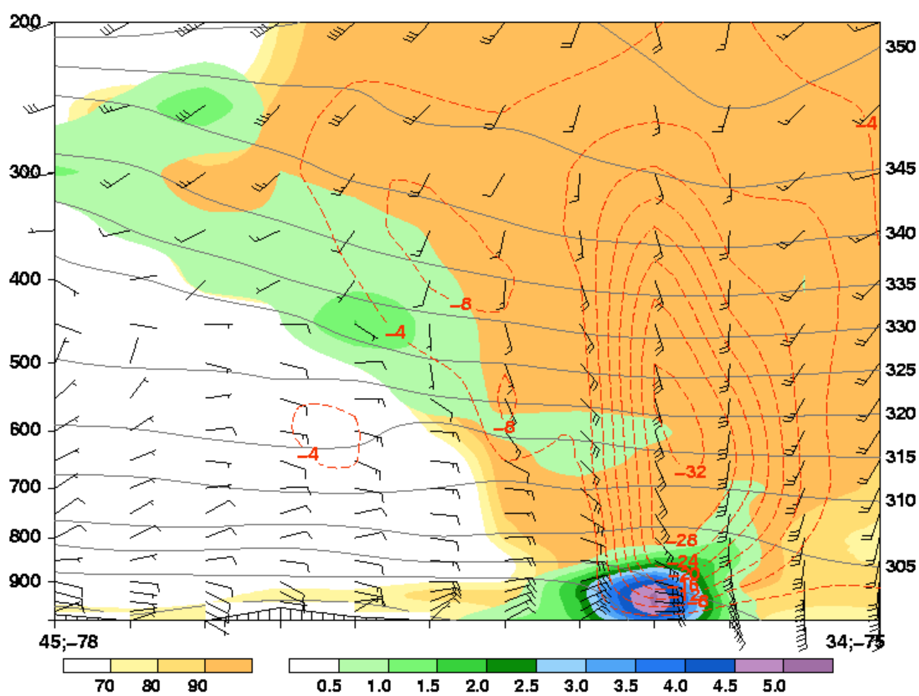

Fig. 3.48. Same as in Fig. 3.15 except at 1200 UTC 1 September 2006 with cross-section orientation shown in Fig. 3.45b.

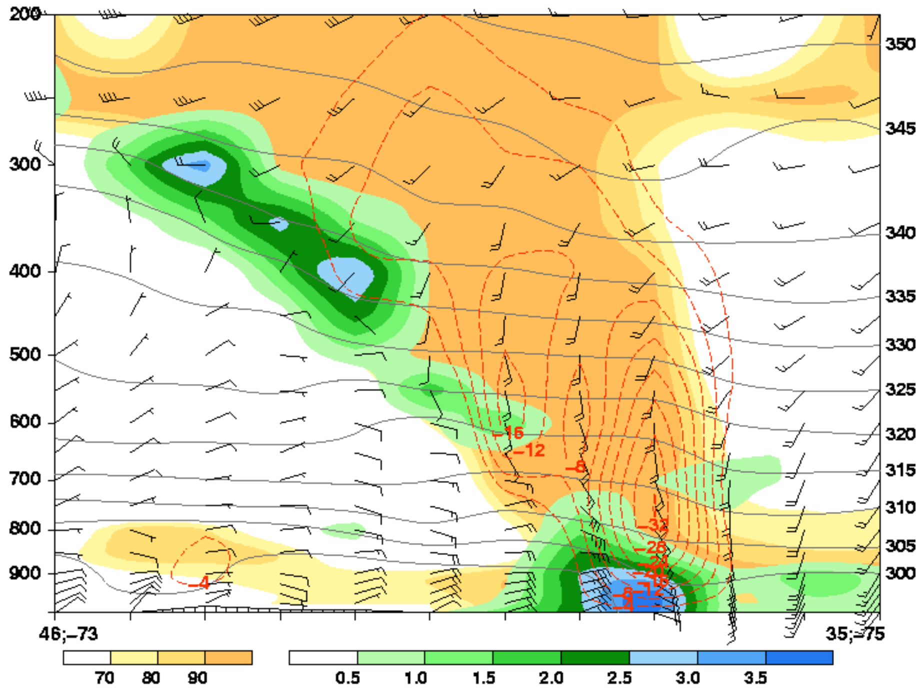

Fig. 3.49. Same as in Fig. 3.15 except at 0000 UTC 2 September 2006 with cross-section orientation shown in Fig. 3.46b.

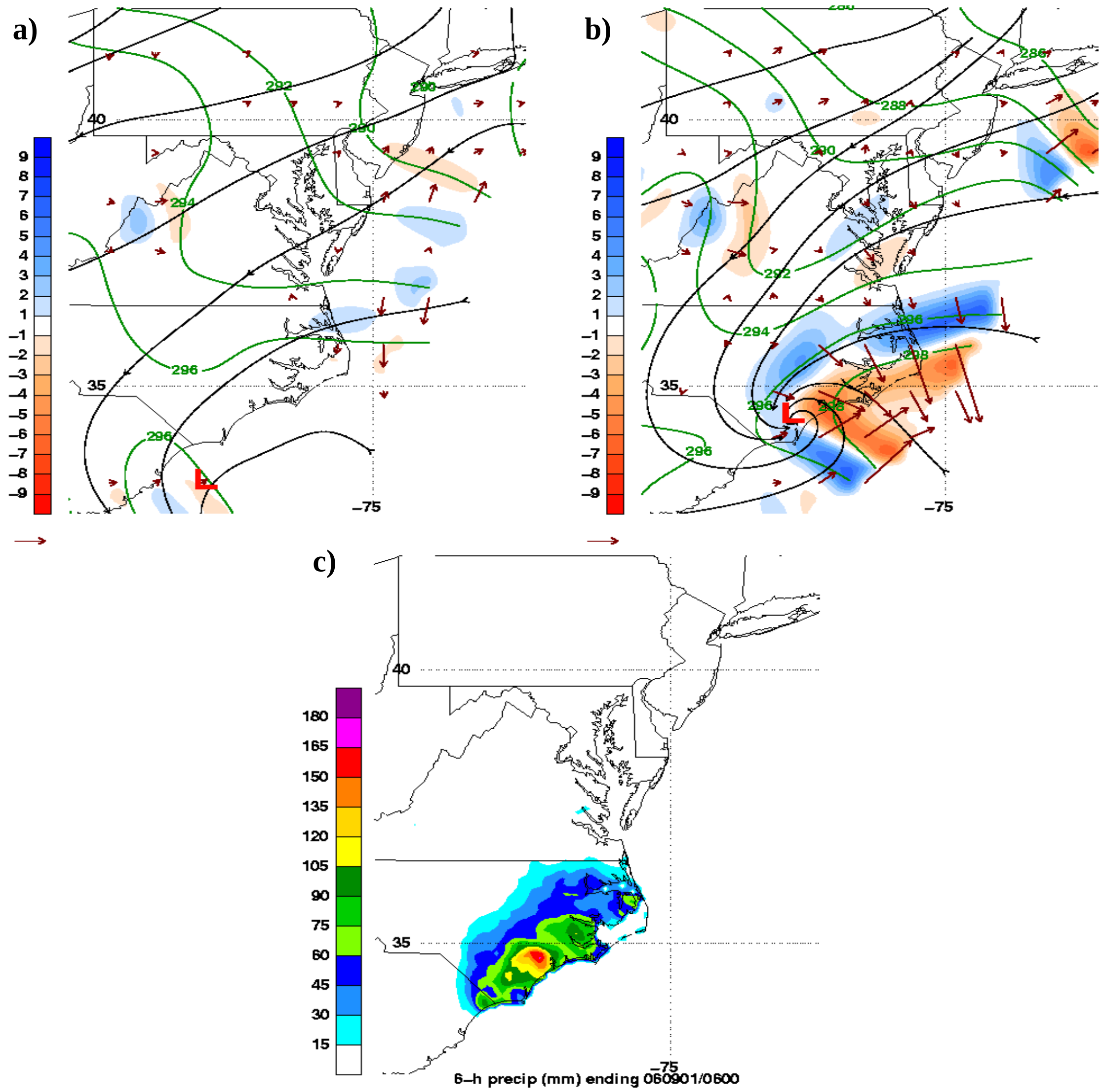

Fig. 3.50. (a) Same as in Fig. 3.18a except at 0000 UTC 1 September 2006. (b) Same as in Fig. 3.18a except at 0600 UTC 1 September 2006. (c) Same as in Fig. 3.18c except ending at 0600 UTC 1 September 2006.

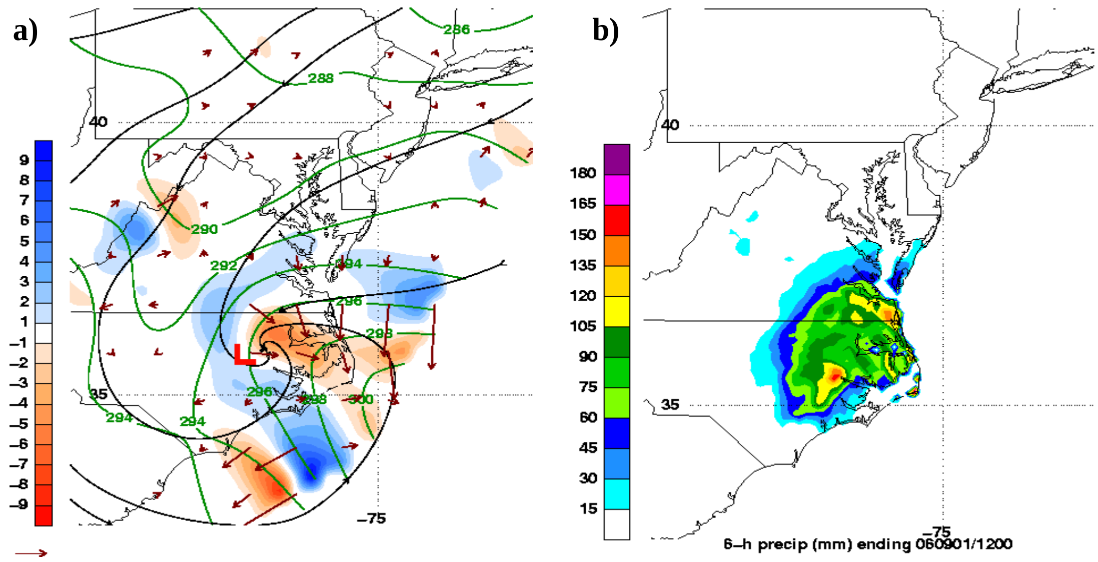

Fig. 3.51. (a) Same as in Fig. 3.18a except at 1200 UTC 1 September 2006. (b) Same as in Fig. 3.18c except ending at 1200 UTC 1 September 2006.

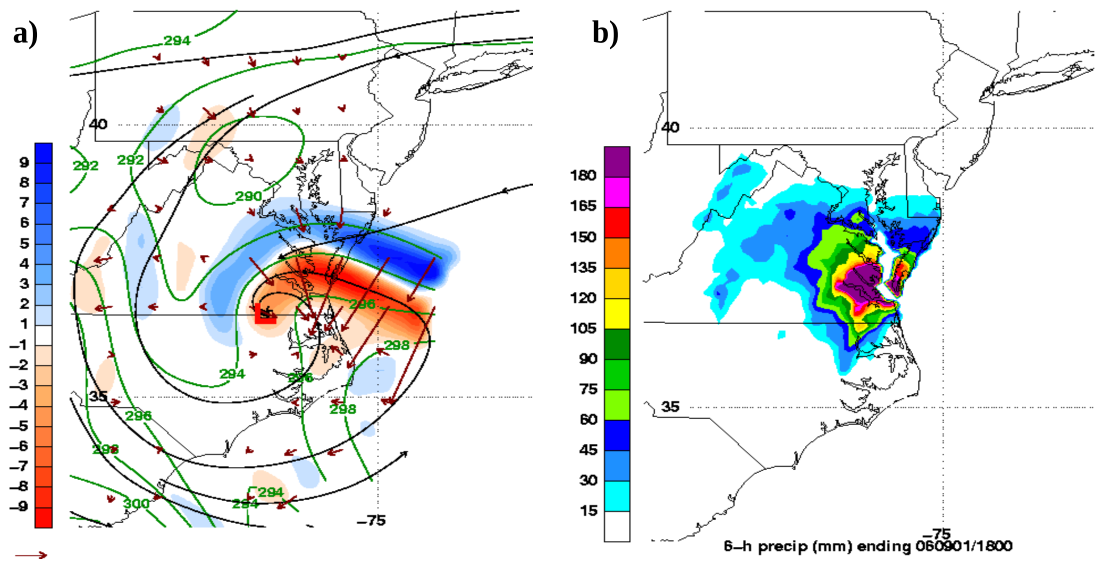

Fig. 3.52. (a) Same as in Fig. 3.18a except at 1800 UTC 1 September 2006. (b) Same as in Fig. 3.18c except ending at 1800 UTC 1 September 2006.

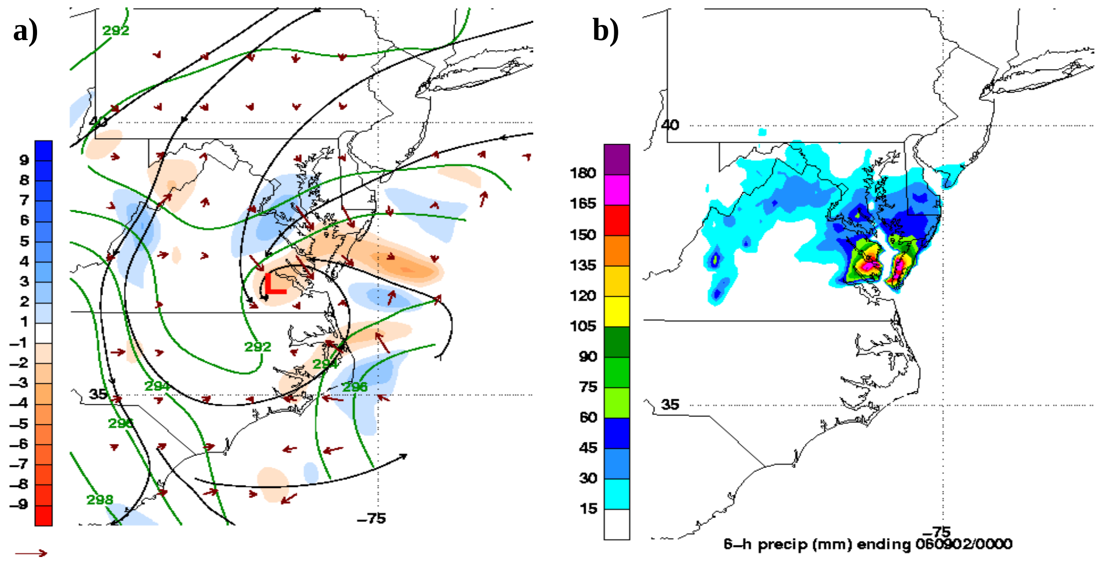

Fig. 3.53. (a) Same as in Fig. 3.18a except at 0000 UTC 2 September 2006. (b) Same as in Fig. 3.18c except ending at 0000 UTC 2 September 2006.

4. Discussion

4.1 Climatology Discussion

Atallah et al. (2007) studied the distribution of precipitation accompanying U.S. landfalling and transitioning TCs and found that a LOT precipitation distribution resulting from the interaction between a TC and an approaching strong midlatitude trough from the northwest corresponded to TCs undergoing ET, while a ROT precipitation distribution was associated with TCs that entered zonal upper-level flow and interacted predominantly with a downstream ridge. These findings can also be applied to the results found in the present climatology study. The interaction between a TC and a trough upstream of the TC occurs frequently in TC-related heavy precipitation events over the northeast U.S. In support of this assertion, a LOT precipitation distribution corresponds to 39 of the 52 (75%) landfalling and transitioning TCs that impacted the northeast U.S. with at least 100 mm of rainfall for 1950–2006 (see Fig. 3.1b). On the other hand, the aforementioned interaction corresponding to a ROT precipitation distribution (Atallah et al. 2007) rarely accompanies these TC-related heavy precipitation events in the northeast U.S., since a ROT precipitation distribution was associated with only three of the 52 (6%) TC events.

A predominantly symmetric (i.e., no-preferential) precipitation distribution, which contains heavy precipitation located on both sides of the TC track, is associated with TCs that are purely tropical (Frank 1977; Marks 1985; Rodgers et al. 1994; Jones et al. 2003). Results from this climatology study reveal that 10 of the 52 (19%) landfalling and transitioning TCs that impacted the northeast U.S. with at least 100 mm of rainfall for 1950–2006 were associated with a no-preferential precipitation distribution (Fig. 3.1b).

A significant interaction between the TC and its midlatitude environment did not occur in these cases.

Monthly climatology statistics show that the majority (40) of the 52 (77%) TC-related heavy precipitation events that impacted the northeast U.S. occurred in the months of August and September (Fig. 3.1c). These monthly climatology results from the present study are consistent with the findings from previous climatology studies, which have shown that Atlantic basin TCs (e.g., Landsea 1993; Neumann et al. 1993) and Atlantic basin TCs that experience ET (Hart and Evans 2001) occur most frequently in the months of August through October. Accordingly, the high frequency of occurrence of the TC-related heavy precipitation events that impacted the northeast U.S. during August and September can be explained plausibly by the climatologically favored rise in both Atlantic basin TC and ET activity during these months.

The results from the total accumulated precipitation analysis of the 16 most recent landfalling and transitioning TCs (2001–2006; see Table I) show that possible orographic precipitation enhancement is observed on the eastern slopes of the Appalachians, including the Blue Ridge Mountains in western North Carolina and northwestern Virginia, the Poconos in northeast Pennsylvania, the Berkshires in western Massachusetts, and the Catskills in southeast New York (Fig. 3.2). Orographic precipitation enhancement over the eastern slopes of the Appalachians during TC-related events was also documented accompanying Camille in 1969 (Schwarz 1970), Agnes in 1972 (Bosart and Dean 1991), Belle in 1976 (DeLuca 2004), and in previous climatology studies (Hart and Evans 2001; Hudgins 2004). Orographic precipitation over the northeast U.S. occurs when a TC tracks far enough inland that low-level easterly flow ahead of the TC is upslope along the eastern slopes of the Appalachians. A topographic map with preferred areas of possible orographic precipitation enhancement in the northeastern U.S. is provided in Fig. 4.1, which summarizes the findings related to orographic effects of the Appalachians in the present climatology study.

4.2 Case Study Discussion

The following subsection will discuss the results of case studies of Ivan (2004), Jeanne (2004), and Ernesto (2006). These three case studies highlight the dynamical mechanisms responsible for heavy precipitation accompanying landfalling and transitioning TCs in the northeast U.S.

Tropical cyclones Ivan (2004), Jeanne (2004), and Ernesto (2006) are associated with distinct precipitation distributions over the eastern U.S. Ivan (Fig. 3.3) and Jeanne (Fig. 3.22) exhibit a shift from an along-track and ROT precipitation distribution, respectively, over the southeast U.S. to a LOT precipitation distribution over the northeastern U.S., while Ernesto (Fig. 3.37) exhibits a ROT precipitation distribution over the mid-Atlantic region. The southwest–northeast-oriented band of heavy rainfall associated with the LOT precipitation distribution in Ivan covers a much broader area and is displaced slightly farther away from the TC track than in Jeanne, while the band of heavy rainfall associated with the ROT precipitation distribution in Ernesto is positioned the close to the TC track. Ernesto contains significantly higher storm-total precipitation amounts (maximum totals exceed 420 mm) over the northeast U.S. than Ivan and Jeanne (maximum totals are near 200 mm in both cases).

The role of upper-level outflow in downstream ridge development and jet streak enhancement has been documented in previous ET studies (e.g., Bosart and Lackmann 1995; Klein et al. 2002; Atallah and Bosart 2003; McTaggart-Cowan et al. 2003; Atallah et al. 2007), showing that diabatic processes (e.g., latent heating) associated with deep convection contribute significantly to amplification of the upper-level flow pattern. In the present study, diabatic heating is inferred from the heavy precipitation evident in the radar reflectivity analyses. Upper-level outflow from the TC produces significant upper-level ridge amplification over the eastern U.S. and western Atlantic and a poleward expansion of the precipitation field at the start of ET, which has also been documented in prior transitioning TCs over the eastern U.S. including Agnes in 1972 (Bosart and Dean 1991) and Floyd in 1999 (Atallah and Bosart 2003; Colle 2003).

In the present study, the process of upper-level jet streak enhancement due to the interaction between a TC and midlatitude trough is illustrated through upper-level Q_n diagnostics. Frontogenesis, which occurs in response to TC-induced outflow transporting tropical air into the relatively cool, dry air of a midlatitude trough, enhances the thermal gradient in the entrance region of the upper-level jet streak. In order to maintain geostrophic balance, a thermally direct transverse ageostrophic circulation, which is manifested as a 300-hPa banded pattern of QG frontogenesis with Q_n divergence (convergence) positioned along the cool (warm) side of the baroclinic zone, is produced to offset the enhancement of the thermal gradient by the geostrophic flow. The upper-level horizontal branch of this circulation acts to accelerate air parcels into the entrance region of the upper-level jet streak, subsequently leading to the intensification and back-building of the jet streak.

The upper-level trough pattern accompanying Ivan and Jeanne corresponds closely to the characteristic northwest pattern described in Harr et al. (2000) (see Figs. 1.5a,b) as the primary midlatitude trough is positioned to the northwest of the TC, while Ernesto is best related to the northeast flow pattern (see Figs. 1.5c,d) since the primary midlatitude trough is positioned to the northeast of Ernesto. In the northwest flow pattern, Ivan and Jeanne are associated with TC-induced ridge amplification that acts to strengthen the geopotential height gradient to the northwest of the TC between the ridge and the advancing midlatitude trough, resulting in an enhancement of the upper-level jet streak. Ensuing formation of an enhanced upper-level divergence band occurs as the divergence from the TC-induced upper-level outflow and the divergence that is characteristically found in the right entrance region of the upper-level jet streak become coupled. Jet streak enhancement during ET has been documented in previous studies (e.g., Hanley et al. 2001; Klein et al. 2002; McTaggart-Cowan et al. 2003; Ritchie and Elsberry 2003; Atallah et al. 2007).

The location of the midlatitude trough in relation to the TC is found to be important for determining where the upper-level dynamics most favorable for heavy precipitation would occur during ET. The upper-level divergence band that forms to the northwest of the TC produces a shift of the upper-level dynamics and precipitation distribution to LOT in Ivan and Jeanne. This LOT shift supports the findings from Atallah et al. (2007), in which a shift to a LOT precipitation distribution occurs as the upper-level trough from the northwest interacts with the TC. The formation of heavy precipitation located in advance of the TC (see Fig. 3.8 for Ivan and Fig. 3.27 for Jeanne), which was coincident with the formation of the divergence band, occurred in region A of the Bosart and Carr (1978) schematic (see Fig. 1.9). Region A is characterized by confluent flow downstream of an approaching midlatitude trough and poleward of the TC. In the case of Ernesto, the midlatitude trough was located to the northeast of Ernesto and much farther downstream than in Ivan and Jeanne, resulting in the upper-level dynamics favorable for heavy precipitation to shift ROT.

The existence of a moisture-rich environment in advance of Agnes in 1972 (Bosart and Carr 1978; Bosart and Dean 1991) and Floyd in 1999 (Atallah and Bosart 2003; Colle 2003) has been documented during previous TC-related heavy precipitation events over the northeast U.S. In the present study, a plume of high precipitable water values underneath the downstream ridge primes the environment with tropical moisture, resulting in the potential for heavy precipitation well in advance of the TC.

Tropical cyclone-induced ridge amplification at upper levels is also evident at lower levels (in the 925-hPa θ and θ_e analyses) as a TC tracks poleward over the eastern U.S. Significant 925-hPa thermal ridge development downshear of a TC is accompanied by a strengthening cyclonically curved low-level jet on the eastern side of the TC. This low-level jet acts to enhance the northward transport of tropical (i.e., high θ_e) air from the Atlantic in advance of the TC into a midlatitude low-level boundary that is located over the northeastern U.S. The development of a cyclonically curved low-level jet on the eastern side of a landfalling and transitioning TC over the northeast U.S. has also been documented previously by DeLuca (2004) during Belle (1972), Gloria (1985), and Bob (1991). The low-level jet was associated with an enhanced low-level geopotential height gradient between the TC and the diabatically amplified western Atlantic ridge.

Keyser et al. (1988, 1992) used an idealized model to study the structure of a midlatitude cyclone and its interaction with a midlatitude baroclinic zone. A partitioning of the Q vector into along- and cross-isentrope components was used to assist in the diagnostic analysis of the idealized model results. They found that the comma-shaped vertical motion field that is characteristic of a midlatitude cyclone develops from a modulation of the wave-scale Q_s dipole pattern by the frontal-scale Q_n banded pattern. The patterns revealed by the partitioned 925-hPa Q vector diagnostics conducted in the present case studies are consistent with those found in the cited idealized model studies. The results of these idealized modeling studies are applicable to the TC–trough/jet interactions associated with the ET of Ivan, Jeanne, and Ernesto.

Q vector diagnostics at 925-hPa are found to specify where QG forcing for ascent could provide a favorable environment for heavy rainfall. In the present case studies, QG forcing for ascent (descent) associated with Q vector convergence (divergence) generally occurs in between the TC and downshear (upshear) low-level thermal ridge (trough). The strongest QG forcing for ascent, which is associated with contributions from both the Q_n and Q_s convergence components, is coincident with the heaviest precipitation.

The convergence of Q_s has been shown by Martin (1999) to correspond to thermal ridge development while providing the predominant dynamical support for ascent in occluded extratropical cyclones. In the present study, the Q_s component of the Q vector contributes considerably to a rotation of the potential temperature gradient and to the total QG forcing for ascent. The strong cyclonic low-level circulation of the TC produces a well-defined Q_s divergence–convergence dipole pattern with convergence (divergence) located between the TC and the downshear (upshear) thermal ridge (trough). The Q_s

pattern accompanying the TC contributes to a cyclonic rotation of the potential temperature gradient from the eastern side of the thermal trough to the western side of the thermal ridge, resulting in an increasingly meridional orientation of the isentropes near the TC. The Q_s divergence–convergence dipole accompanying Ernesto is stronger than in Ivan and Jeanne as diagnoses of Ernesto are conducted immediately after landfall in North Carolina and therefore refer to a pronounced tropical circulation, whereas diagnoses of Ivan and Jeanne are conducted well after landfall along the Gulf Coast when subsequent weakening of the TC circulation over land has already occurred.

The interaction between a TC and a midlatitude low-level thermal boundary occurs as a TC tracks poleward, resulting in the development of a frontal boundary and asymmetries in the precipitation structure at the onset of ET (Bosart and Dean 1991; Harr and Elsberry 2000; Klein et al. 2000; Jones et al. 2003). At the start of ET, the development of a warm-frontal boundary to the northeast of a TC has been observed previously during Typhoons David (1997) and Opal (1997) (Harr and Elsberry 2000), and during the present case studies of Ivan (2004), Jeanne (2004), and Ernesto (2006). In the present case studies, the interaction between the TC and a midlatitude low-level boundary that is situated across the eastern U.S. leads to the development of a warm-frontal boundary in between the TC and downshear thermal ridge. A thermally direct transverse ageostrophic circulation associated with the warm-frontal boundary is marked by strong frontogenesis and a Q_n divergence–convergence banded pattern at 925 hPa. The flow along the warm-frontal boundary is highly confluent with a southeasterly component to the flow on the warm side of the boundary and a northerly component to the flow on the cool side of the boundary. The development of the warm-frontal boundary is coincident with a poleward expansion of the precipitation field into the northeastern U.S. as the Q_n convergence component along the warm-frontal boundary makes a significant contribution to the total QG forcing for ascent.

The development of a surface frontal boundary observed in Ivan, Jeanne, and Ernesto occurs in a similar manner to that observed during previous studies of cool-season coastal fronts (e.g., Bosart et al. 1972; Bosart 1975) and transitioning TCs over the northeast U.S. (Bosart and Dean 1991; Atallah and Bosart 2003; Colle 2003; DeLuca 2004). These previous studies documented that coastal frontogenesis occurred due to convergence accompanying land–sea thermal contrasts produced by cold-air damming and/or heat fluxes from the ocean and convergence due to differential friction. In the present study, the surface frontal boundary forms as oceanic heat fluxes of tropical air that is induced by the TC circulation enhance the land–sea thermal contrast along the warm-frontal boundary. The heaviest 6-h accumulated precipitation occurs in a mesoscale band located along and on the cold side of the surface frontal boundary. Banded mesoscale precipitation structures similar to those found in the present case studies have been previously documented with landfalling and/or transitioning TCs including Camille in 1969 (Schwarz 1970), Agnes in 1972 (Bosart and Dean 1991), and Floyd in 1999 (Atallah and Bosart 2003; Colle 2003).

Distinct vertical structures of the warm-frontal boundary are associated with the two LOT cases (Ivan and Jeanne) and the ROT case (Ernesto). In the case of Ivan and Jeanne, the juxtaposition of the TC and an upper-level midlatitude trough produces a tropospheric-deep region of frontogenesis and ascent in the equatorward entrance region of an upper-level jet. This tropospheric-deep region of frontogenesis and ascent tilts toward the cooler air (i.e., north-northwest) with height, resulting in heavy precipitation along and on the cool side of the low-level warm-frontal boundary and a LOT precipitation distribution as the TC moves toward the northeast. The tilted frontogenesis and ascent pattern is more intense in Ivan than in Jeanne as Ivan has a more pronounced interaction with the upper-level trough. In the case of Ernesto, strong, upright ascent and frontogenesis focused near the surface are located in a tropospheric-deep saturated environment that produces conditions favorable for heavy rainfall near the warm-frontal boundary. The interaction between Ernesto and the upper-level jet streak that is positioned to the northeast produces much weaker upper-level frontogenesis than in Ivan and Jeanne. The warm-frontal boundary associated with Ernesto contains a frontogenesis pattern that tilts toward the north-northeast, resulting in a ROT precipitation distribution accompanying the northward-moving Ernesto. In both LOT and ROT cases, the TC circulation induces a poleward transport of tropical air into the warm-frontal boundary. The cyclonically curved low-level jet on the eastern side of the TC further enhances the transport of tropical air from the Atlantic into the warm-frontal boundary, producing the deep ascent and heavy precipitation observed to the northeast of the TC. Furthermore, the confluent low-level flow along the warm-frontal boundary leads to a persistent supply of ample moisture from the boundary layer into the region of heavy precipitation.

4.3 Summary and Conceptual Models for Forecasters

Conceptual models (Figs. 4.2a–d and 4.3a,b) will be presented in this subsection to assist forecasters in identifying the key synoptic and mesoscale features that were discussed in this thesis. Although a separate conceptual model is given for the LOT and

ROT cases, emphasis should be placed on the LOT conceptual models (Figs. 4.2a,b and 4.3a) since a LOT precipitation distribution was associated with the majority (75%) of the 52 TC-related heavy precipitation events studied in the climatology, while a ROT precipitation distribution was associated with only a small proportion (6%) of these events.

A schematic diagram of the key upper- and lower-level features associated with heavy precipitation accompanying landfalling and transitioning TCs over the northeast U.S. is shown in Figs. 4.2a–d. A significant distinction in the upper-level synoptic pattern is evident between LOT (Fig. 4.2a) and ROT (Fig. 4.2c) precipitation distribution cases. In LOT cases, the interaction between the TC and an upper-level trough positioned to the northwest of the TC produces an enhanced upper-level jet streak, resulting in an environment conducive to heavy precipitation over the northeast U.S. as the upper-level dynamics shift LOT. In ROT cases, the interaction between the TC and an upper-level trough located to the northeast of the TC produces a jet streak much further downstream than in LOT cases, resulting in the upper-level dynamics favorable for heavy precipitation to shift ROT.

Several key low-level features are similar in the LOT (Fig. 4.2b) and ROT (Fig. 4.2d) cases. In both cases, a distinct low-level Q_s divergence–convergence dipole pattern with convergence (divergence) located in between the TC and downshear (upshear) low-level thermal ridge (trough) accompanies the strong cyclonic circulation of the TC. Additionally, a warm-frontal boundary that is marked by strong frontogenesis (i.e., Q_n vectors pointing toward warmer air) and a Q_n divergence–convergence banded pattern forms along a midlatitude low-level thermal boundary in between the TC and downshear thermal ridge. A broad area of heavy rainfall is positioned to the northeast of the TC, where Q_s and Q_n convergence are collocated to maximize the total Q vector convergence (i.e., QG forcing for ascent) over an area of strong low-level frontogenesis. The heaviest rainfall occurs along and on the cold side of a mesoscale surface boundary, where southeasterly flow on the warm side intersects northerly flow on the cool side. The southeasterly flow induced by the TC circulation and low-level jet is feeding tropical air from the Atlantic toward the surface boundary.

Important differences in the vertical structure across the warm-frontal boundary are noted in the LOT (Fig. 4.3a) and ROT (Fig. 4.3b) schematic cross sections. These cross sections, which are constructed parallel to the lower-level (e.g., 925–500-hPa) layer-averaged thermal gradient and across the region of strongest frontogenesis, portray the frontogenesis and ascent fields. The warm-frontal boundary associated with LOT cases is characterized by a tropospheric-deep frontogenesis pattern that tilts toward the cooler air with height and is strongest in the boundary layer and at upper-levels. The ascent pattern tilts toward cooler air with height and is located on the warm side of the frontogenesis maximum. Ascent is maximized in the midtroposphere above and on the warm side of the frontogenesis region. The warm-frontal boundary illustrated in the ROT schematic contains strong frontogenesis that is focused near the surface. Strong, upright ascent is located over and on the warm side of the frontal boundary with maximum values immediately above the boundary layer. In both LOT and ROT cases, low-level convergence that is implied by $\partial\omega/\partial p > 0$ in the boundary layer provides evidence for enhanced lift over the frontal boundary, with the latter case being more intense.

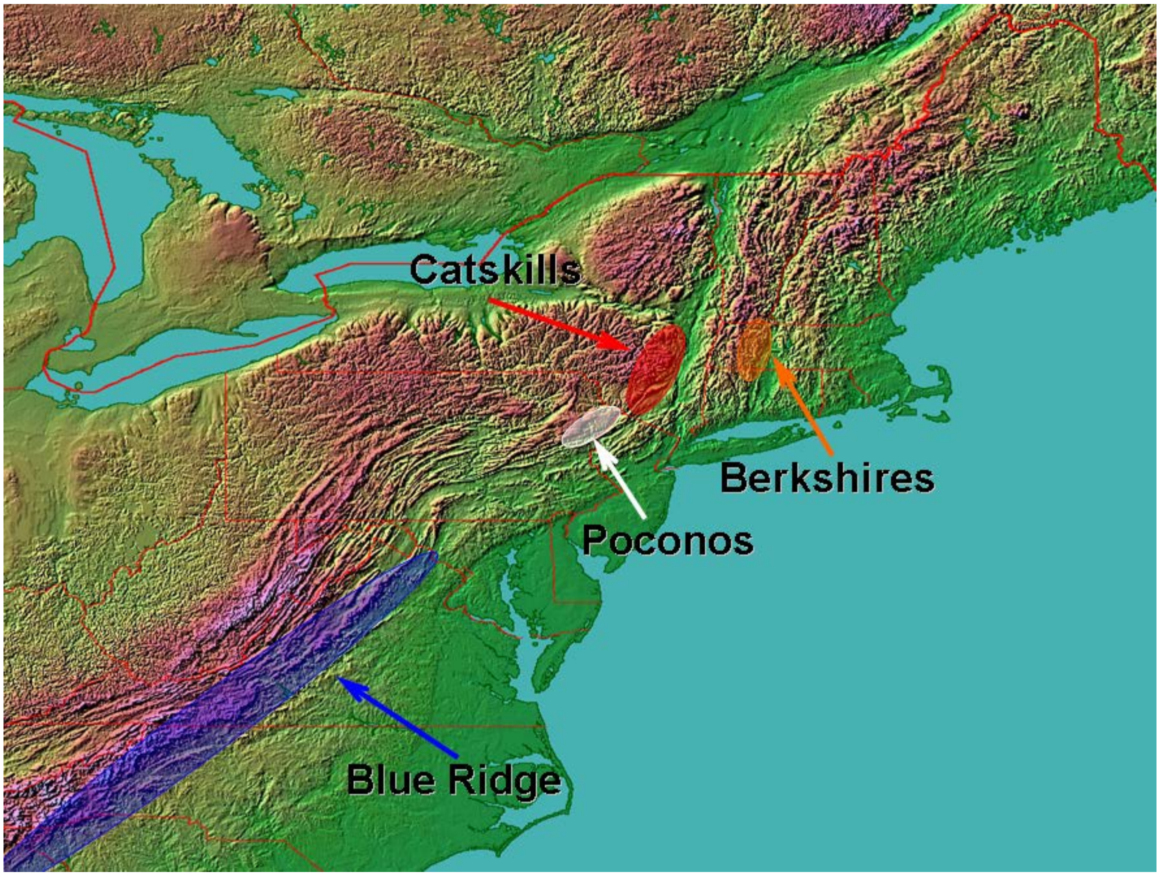

Fig. 4.1. Topographic map containing the preferred areas of possible orographic precipitation enhancement in the northeast U.S. based on results from Fig. 3.2. Topographic image from http://fermi.jhuaple.edu/states.html.

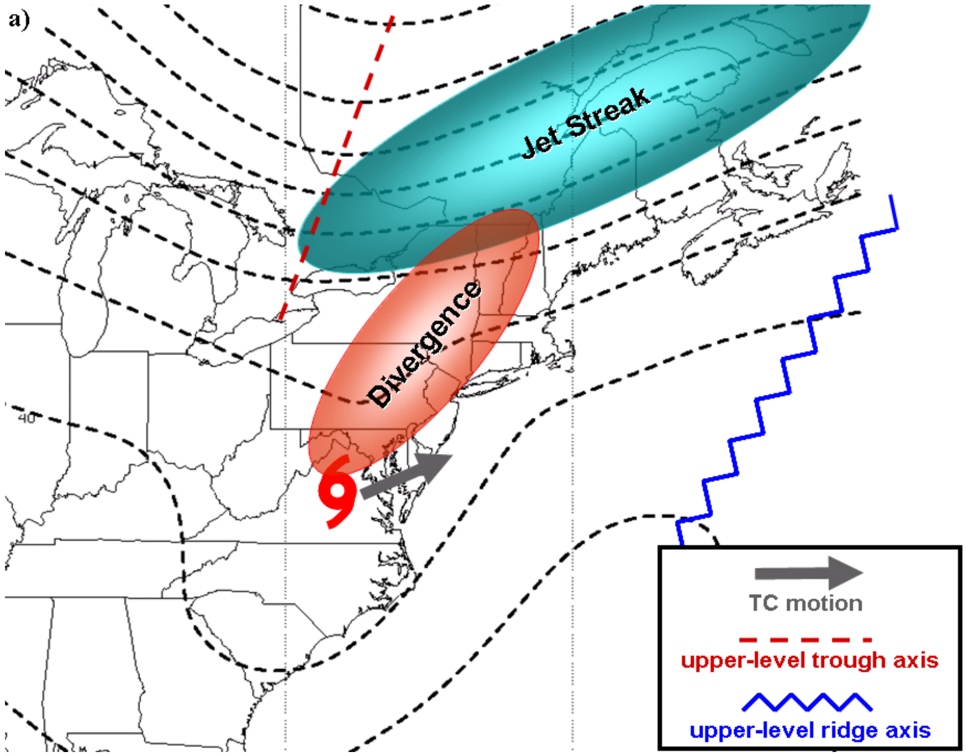

Fig. 4.2. Conceptual model illustrating the key ingredients for heavy precipitation accompanying landfalling and transitioning TCs over the northeast U.S. (a) Schematic of upper-level features associated with LOT precipitation distribution cases. Upper-level geopotential height dashed contoured in black, jet streak shaded in blue, divergence shaded in red, primary midlatitude trough axis denoted by the red-dashed line, TC-induced ridge axis denoted by the blue zig-zag line, center of TC circulation denoted by the red tropical storm symbol, and TC motion denoted by the gray arrow. (b) Schematic of lower-level features associated with LOT precipitation distribution cases. Low-level potential temperature contoured in black, area of heavy rainfall shaded in green, Q_s divergence–convergence shaded in teal–orange, Q_n divergence–convergence shaded in blue–red, Q_n vectors denoted by the brown arrows, low-level jet denoted by the thick blue arrow, center of TC circulation denoted by the red tropical storm symbol, and surface frontal boundary denoted by the purple line. (c) Same as in (a) except for ROT precipitation distribution cases. (d) Same as in (b) except for ROT precipitation distribution cases.

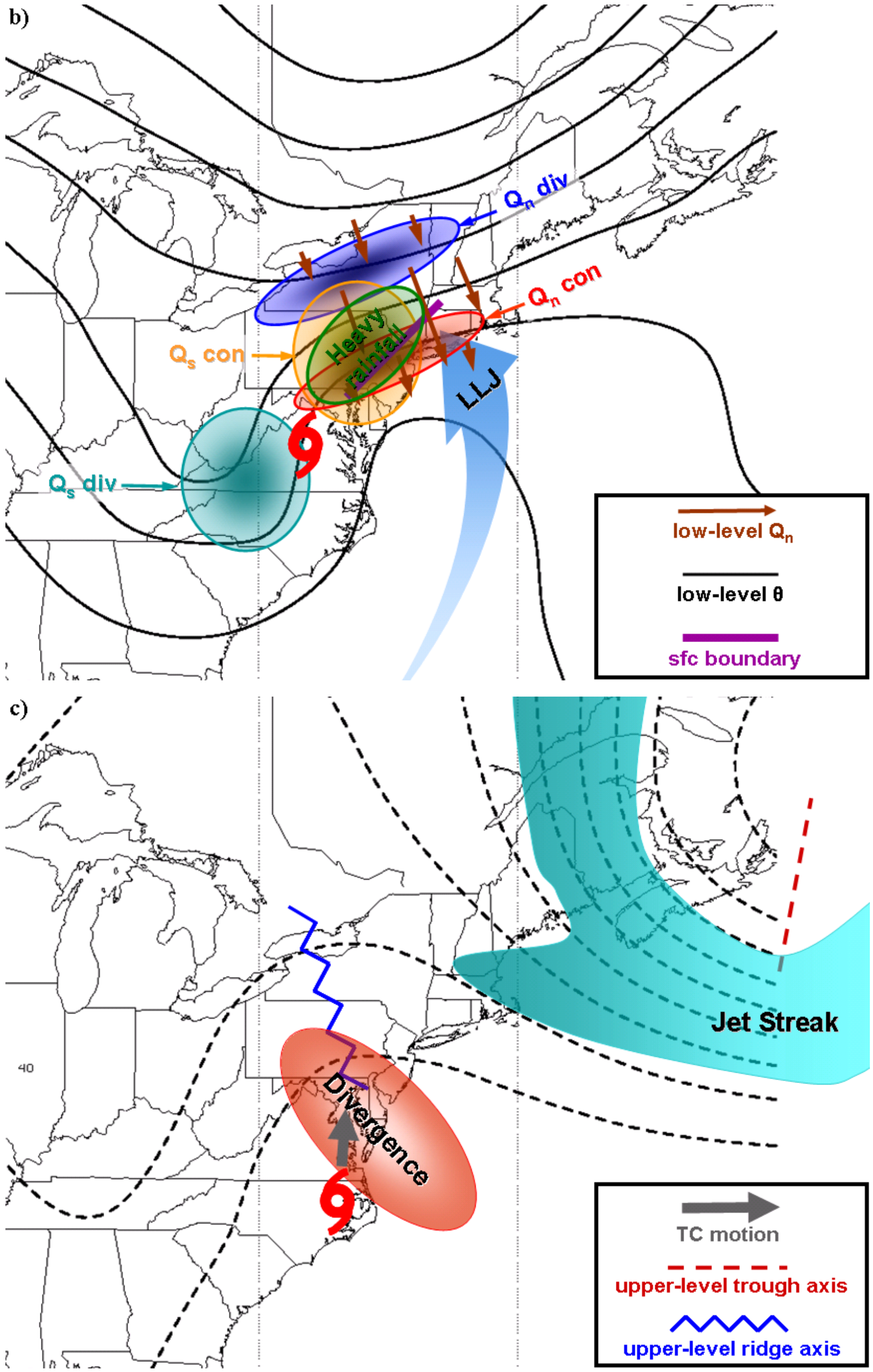

Fig. 4.2. *continued*.

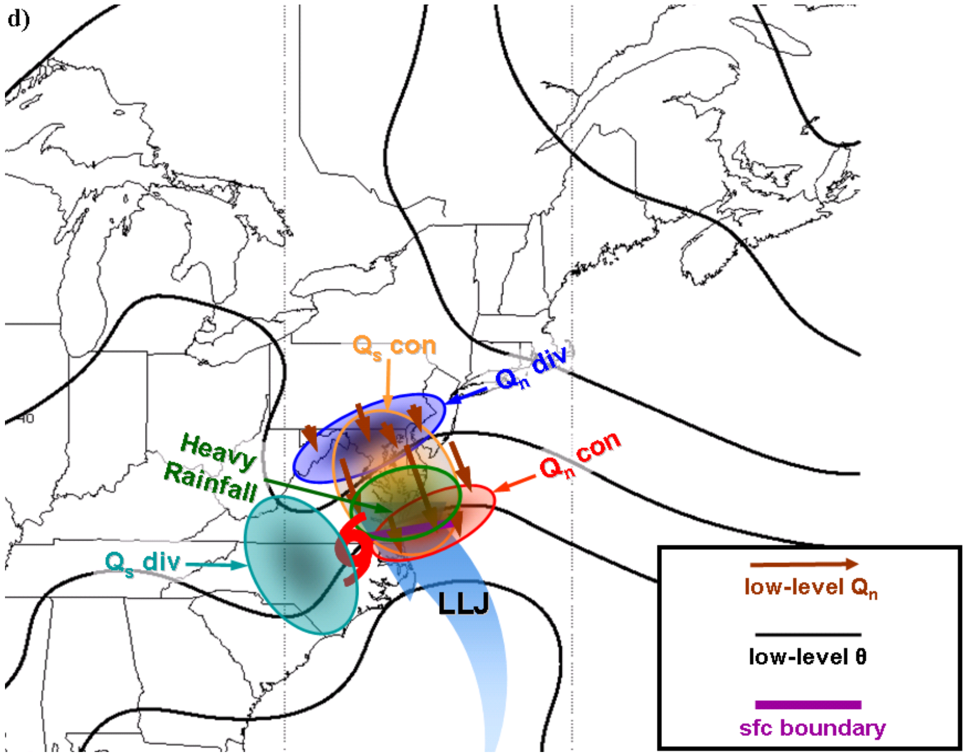

Fig. 4.2. *continued*.

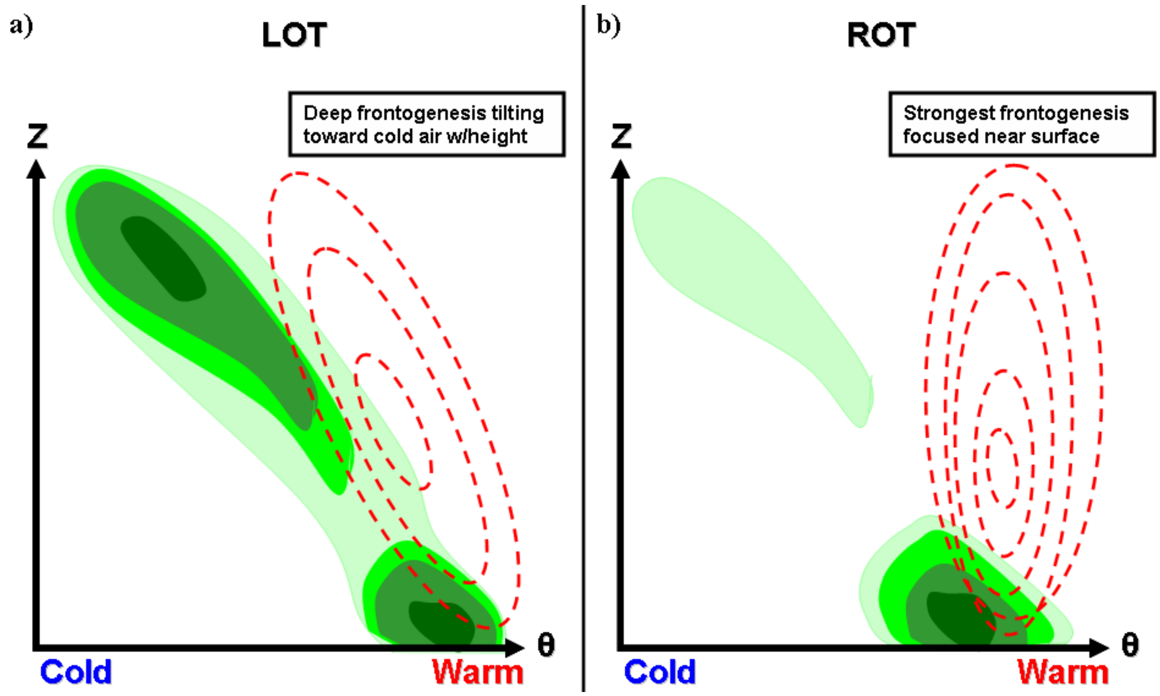

Fig. 4.3. Schematic cross section of the warm-frontal boundary found in (a) LOT precipitation distribution cases and (b) ROT precipitation distribution cases. Cross section includes frontogenesis shaded in green and vertical velocity dashed contoured in red.

5. Conclusions and Future Work

5.1 Conclusions

The main objective of this study was to understand how the observed mesoscale distribution of heavy rainfall accompanying landfalling and transitioning TCs over the northeast U.S. is modulated by interactions between these TCs and transient synoptic and mesoscale disturbances. A dataset of 52 landfalling and transitioning TCs that impacted the northeast U.S. with more than 100 mm of rainfall for 1950–2006 was prepared to enable the construction of a climatology of these TC-related heavy precipitation events. Three representative cases [Ivan (2004), Jeanne (2004), and Ernesto (2006)] were selected for detailed study in order to document and illustrate how the synoptic and mesoscale forcing modulates the precipitation distribution.

Monthly climatology statistics derived from the 52-TC dataset revealed that the majority (77%) of the 52 TC-related heavy precipitation events impacted the northeast U.S. during the climatologically favored months of August and September. The climatology results for precipitation distribution versus TC track showed that a LOT precipitation distribution corresponded to 75% of the 52 events, implying that these events were generally associated with TCs that eventually underwent ET over the northeast U.S. A no-preferential precipitation distribution and a ROT precipitation distribution were far less common in TC-related heavy precipitation cases, being associated with only a small number of events (19% and 6%, respectively).

The results from the case studies of Ivan, Jeanne, and Ernesto have identified important dynamical mechanisms responsible for heavy rainfall during these TC events. All three cases are associated with TC-induced upper-level downstream ridge development over the eastern U.S. and western Atlantic. A plume of high precipitable water values underneath the downstream ridge primes the environment with tropical moisture, resulting in the potential for heavy precipitation well in advance of the TC. The location of the primary upper-level trough/jet streak controls where the upper-level dynamics (i.e., divergence) favorable for heavy precipitation would occur relative to the poleward-moving TC. Ivan and Jeanne are associated with TC-induced upper-level ridge amplification that acts to strengthen the geopotential height gradient to the northwest of the TC between the ridge and an advancing midlatitude trough, resulting in the enhancement of an upper-level jet streak. Ensuing formation of an enhanced upper-level divergence band occurs as the divergence from the TC-induced upper-level outflow and the divergence from the upper-level jet streak become coupled. This upper-level divergence band, which forms to the northwest of the TC track, produces a shift of the precipitation distribution to LOT over the northeast U.S. In the case of Ernesto, the primary upper-level trough/jet streak is located to the northeast of Ernesto and much farther downstream than in Ivan and Jeanne, resulting in a shift of the upper-level divergence and precipitation distribution to ROT.

Characteristic low-level features that produce conditions favorable for heavy precipitation are found in all three cases. Q vector diagnostics links the presence of strong low-level QG forcing for ascent (i.e., Q vector convergence) to areas of heavy precipitation. QG forcing for ascent is maximized when Q_s and Q_n convergence are collocated. The interaction between the TC and midlatitude low-level warm-frontal boundary results in several distinct low-level features: 1) a cyclonically curved low-level jet located on the eastern side of the TC that acts to enhance the northward flux of tropical air from the Atlantic into the warm-frontal boundary, 2) a dipole pattern of Q_s forcing for ascent (descent) located between the TC and downshear (upshear) low-level thermal ridge (trough) with Q_s vectors oriented to produce a cyclonic rotation of the potential temperature gradient, and 3) a banded pattern of Q_n forcing for descent–ascent with Q_n vectors oriented toward warmer air (i.e., QG frontogenesis) positioned within the warm-frontal boundary beneath the equatorward entrance region of an upper-level jet streak. The heaviest precipitation is configured in mesoscale bands of enhanced rainfall that develop along the surface warm-frontal boundary.

The vertical structure of the warm-frontal boundary can be linked to either a LOT or ROT precipitation distribution. The warm-frontal boundary associated with a LOT precipitation distribution (Ivan and Jeanne) features a tropospheric-deep frontogenesis pattern that tilts toward the cooler air with height and is strongest in the boundary layer and within the entrance region of an upper-level jet streak. This frontogenesis pattern induces a tilted ascent pattern along and on the warm side of the frontal boundary. The warm-frontal boundary associated with a ROT precipitation distribution (Ernesto) features strong frontogenesis that is focused near the surface. This frontogenesis pattern induces strong, upright ascent that is located over and on the warm side of the frontal boundary and is maximized immediately above the boundary layer.

It is anticipated that successful integration and communication of the findings in this study through technology transfer will assist NWS operational forecasters during similar weather events in future situations, resulting in improved forecasts. The conceptual models provided in this thesis (Figs. 4.2a–d and 4.3a,b) can be applied by forecasters to assess the potential for TC-related heavy rainfall and flash flooding events over the northeast U.S.

5.2 Future Work

A detailed study of additional cases in the 52-TC dataset could be performed in order to advance an understanding of the important synoptic and mesoscale dynamical mechanisms responsible for producing heavy precipitation accompanying landfalling and transitioning TCs. A composite analysis of the 52 TCs identified in this dataset can be performed objectively to help identify characteristic dynamical signatures important to the development of heavy precipitation in these TCs. Furthermore, a comprehensive investigation could be conducted to assess how well the short- and medium-range forecasts for various operational models predict heavy precipitation events accompanying landfalling and transitioning TCs. This type of investigation can help improve forecast skill during future TC-related heavy precipitation events by taking past model performance into account.

Previous cool-season studies by Novak et al. (2004, 2006) have used cross-section analyses to diagnose the development of mesoscale bands of heavy snowfall. These cross-section analyses revealed that mesoscale band development occurred in the presence of frontogenesis, weak moist symmetric stability, and an ample supply of moisture. A cross-section analysis similar to that done by Novak et al. (2004, 2006) could be used to assess the potential for the development of mesoscale heavy precipitation bands along warm-frontal boundaries accompanying landfalling and transitioning TCs by examining characteristics of lift, stability, and moisture.

A high-resolution modeling study could be performed to diagnose the role of particular dynamic and thermodynamic processes involved in TC-related heavy precipitation events (e.g., diabatic contributions to TC-induced upper-level ridge development and to frontogenesis along the warm-frontal boundary; orographic effects on precipitation in northeastern U.S.). Modeling studies are increasingly attainable since NWS weather forecasting offices in the northeastern U.S. run their own models locally.

REFERENCES

Atallah, E., and L. F. Bosart, 2003: The extratropical transition and precipitation distribution of hurricane Floyd (1999). *Mon. Wea. Rev.*, **131**, 1063–1081.

———, ———, and A.R. Aiyyer, 2007: Precipitation distribution associated with landfalling tropical cyclones over the eastern United States. *Mon. Wea. Rev.*, **135**, 2185–2206.

Ballentine, R. J., 1980: A numerical investigation of New England coastal frontogenesis. *Mon. Wea. Rev.*, 108, 1479–1497.

Barnes S. L., 1964: A technique for maximizing details in numerical weather map analysis. *J. Appl. Meteor*, **3**, 396–409.

Bergeron, T., 1949: The problem of artificial control of rainfall on the globe. Part II: The coastal orographic maxima of precipitation in autumn and winter. *Tellus*, **1**, 15-32.

Bluestein, H.B., 1992: Synoptic-dynamic meteorology in the mid-latitudes: Volume I: Principles of kinematics and dynamics. Oxford, pp. 431.

Bosart, L. F., 1975: New England coastal frontogenesis. *Quart. J. Roy. Meteor. Soc.*, **101**, 957–978.

———, 1981: The Presidents' Day snowstorm of 18-19 February 1979: A subsynoptic-scale event. *Mon. Wea. Rev.*, **109**, 1542–1566.

———, 1984: The Texas coastal rainstorm of 17-21 September 1979: An example of synoptic-mesoscale interaction. *Mon. Wea. Rev.*, **112**, 1108–1133.

———, and F. H. Carr, 1978: A case study of excessive rainfall centered around Wellsville, New York, 20-21 June 1972. *Mon. Wea. Rev.*, **106**, 348–362.

———, and S. C. Lin, 1984: A diagnostic analysis of the Presidents' Day storm of February 1979. *Mon. Wea. Rev.*,**112**, 2148–2177.

———, and D. B. Dean, 1991: The Agnes rainstorm of June 1972: Surface feature evolution culminating in inland storm redevelopment. *Wea. and Forecasting*, **6**, 515–537.

———, and G. M. Lackmann, 1995: Postlandfall tropical cyclone reintensification in a weakly baroclinic environment: A case study of hurricane David (September 1979). *Mon. Wea. Rev.*, **123**, 3268-3291.

———, C. J. Vaudo, and J. H. Helsdon, 1972: Coastal frontogenesis. *J. Appl. Meteor.*, **11**, 1236–1258.

———, C.C. Lai, and R.A. Weisman, 1992: A case study of heavy rainfall associated with weak cyclogenesis in the northwest Gulf of Mexico. *Mon. Wea. Rev.*, **120**, 2469–2500.

Carr, F. H., and L. F. Bosart, 1978: A diagnostic evaluation of rainfall predictability for tropical storm Agnes, June 1972. *Mon. Wea. Rev.*, **106**, 348-362.

Chen, S.S., J.A. Knaff, and F.D. Marks, 2006: Effects of vertical wind shear and storm motion on tropical cyclone rainfall asymmetries deduced from TRMM. *Mon. Wea. Rev.*, **134**, 3190–3208.

Colle, B. A., 2003: Numerical simulations of the extratropical transition of Floyd (1999): Structural evolution and responsible mechanisms for the heavy rainfall over the northeast United States. *Mon. Wea. Rev.*, **131**, 2905–2926.

DeLuca, D. P., 2004: The distribution of precipitation over the Northeast accompanying landfalling and transitioning tropical cyclones. M.S. Thesis, Department of Earth and Atmospheric Sciences, University at Albany/SUNY, 178 pp.

desJardins M.L., K.F. Brill, and S.S. Schotz, 1991: GEMPAK5, Part1- GEMPAK5 programmer's guide. NASA Technical Memorandum, 4260 pp.

DiMego, G. J., and L. F. Bosart, 1982a: The transformation of tropical storm Agnes into an extratropical cyclone. Part I: The observed fields and vertical motion computations. *Mon. Wea. Rev.*, **110**, 385–411.

———, and ———, 1982b: The transformation of tropical storm Agnes into an extratropical cyclone. Part II: Moisture, vorticity and kinetic energy budgets. *Mon. Wea. Rev.*, **110**, 412–433.

Elsberry, R.L., 2005: Achievement of USWRP hurricane landfall research goal. *Bull. Amer. Meteor. Soc.*, **86**, 643–645.

Evans, J. L., and R. E. Hart, 2003: Objective indicators of the life cycle evolution of extratropical transition for Atlantic tropical cyclones. *Mon. Wea. Rev.*, **131**, 909–925.

———, and B.E. Prater-Mayes, 2004: Factors affecting the posttransition intensification of hurricane Irene (1999). *Mon. Wea. Rev.*, **132**, 1355–1368.

———, J.M. Arnott, and F. Chiaromonte, 2006: Evaluation of operational model cyclone structure forecasts during extratropical transition. *Mon. Wea. Rev.*, **134**, 3054–3072.

Foley, G. R., and B. N. Hanstrum, 1994: The capture of tropical cyclones by cold fronts off the west coast of Australia. *Wea. and Forecasting*, **9**, 577–592.

Franklin, J.L., R.J. Pasch, L.A. Avila, J.L. Beven, M.B. Lawrence, S.R. Stewart, and E.S. Blake, 2006: Atlantic hurricane season of 2004. *Mon. Wea. Rev.*, **134**, 981–1025.

Haggard, W. H., T. H. Bilton, and H. L. Crutcher, 1973: Maximum rainfall from tropical cyclone systems which cross the Appalachians. *J. Appl. Meteor.*, **12**, 50–61.

Hanley, D., J. Molinari, and D. Keyser, 2001: A composite study of the interactions between tropical cyclones and upper-tropospheric troughs. *Mon. Wea. Rev.*, **129**, 2570–2584.

Harr, P. A., and R. L. Elsberry, 2000: Extratropical transition of tropical cyclones over the western north Pacific. Part I: Evolution of structural characteristics during the transition process. *Mon. Wea. Rev.*, **128**, 2613–2633.

———, ———, and T. F. Hogan, 2000: Extratropical transition of tropical cyclones over the western north Pacific. Part II: The impact of midlatitude circulation characteristics. *Mon. Wea. Rev.*, **128**, 2634–2653.

Hart, R. E., 2003: A cyclone phase space derived from thermal wind and thermal asymmetry. *Mon. Wea. Rev.*, **131**, 585–616.

———, and J. L. Evans, 2001: A climatology of the extratropical transition of Atlantic tropical cyclones. *J. of Climate*, **14**, 546–564.

———, ———, and C. Evans, 2006: Synoptic composites of the extratropical transition life cycle of north Atlantic tropical cyclones: Factors determining posttransition evolution. *Mon. Wea. Rev.*, **134**, 553–578.

Higgins, R. W., W. Shi, E. Yarosh, and R. Joyce, 2000: Improved US precipitation quality control system and analysis. *NCEP/Climate Prediction Center ATLAS No. 6*.

Hoskins, B. J., and M. A. Pedder, 1980: The diagnosis of middle latitude synoptic development. *Quart. J. Roy. Meteor. Soc.*, **106,** 707–719.

———, I. Draghici, and H. Davies, 1978: A new look at the ω-equation. *Quart. J. Roy. Meteor. Soc.*, **104,** 31–38.

———, M. E. McIntyre, and A. W. Robertson, 1985: On the use and significance of isentropic potential vorticity maps. *Quart. J. Roy. Meteor. Soc.*, **111**, 877–946.

Hudgins, J., S. Keighton, K. Kostura, and J. Jackson, 2004: Climatology of heavy rainfall associated with tropical cyclones affecting the central Appalachians. *26th Conf. on Hurricanes and Tropical Meteorology, 3-7 May 2004, Miami, FL*.

Jones, S. C., P. A. Harr, J. Abraham, L. F. Bosart, P. J. Bowyer, J. L. Evans, D. E. Hanley, B. N. Hanstrum, R. E. Hart, F. Lalaurette, M. R. Sinclair, R. K. Smith, and C. Thorncroft, 2003: The extratropical transition of tropical cyclones: Forecast challenges, current understanding, and future directions. *Wea. and Forecasting*, **18**, 1052–1092.

Kalnay, E., M. Kanamitsu, and W. Baker, 1990: Global numerical weather prediction at the National Meteorological Center. *Bull. Amer. Meteor. Soc.*, **71**, 1410–1428.

———, ———, R. Kistler, W. Collins, D. Deaven, L. Gandin, M.Iredell, S. Saha, G. White, J. Woollen, Y. Zhu, M. Chelliah, W. Ebisuzaki, W. Higgins, J. Janowiak, K. C. Mo, C. Ropelewski, J. Wang, A. Leetmaa, R. Reynolds, R. Jenne, and D. Joseph, 1996: The NCEP/NCAR 40-year reanalysis project. *Bull. Amer. Meteor. Soc.*, **77**, 437–471.

Kanamitsu, M., J. Alpert, K. Campana, P. Caplan, D. Deaven, M. Iredell, B. Katz, H.L. Pan, J. Sela, and G. White, 1991: Recent changes implemented into the Global Forecast System at NMC. *Wea. Forecasting*, **6**, 425–435.

Keyser, D., M. J. Reeder, and R. J. Reed, 1988: A generalization of Petterssen's frontogenesis function and its relation to the forcing of vertical motion. *Mon. Wea. Rev.*, **116**, 762–780.

———, B.D. Schmidt, and D.G. Duffy, 1992: Quasigeostrophic vertical motions diagnosed from along- and cross-isentrope components of the Q vector. *Mon. Wea. Rev.*, **120**, 731–741.

Kistler, R., E. Kalnay, W. Collins, S. Saha, G. White, J. Woollen, M. Chelliah, W. Ebisuzaki, M. Kanamitsu, V. Kousky, H. van den Dool, R. Jenne, and M. Fiorino, 2001: The NCEP/NCAR 50-year reanalysis: Monthly means CD-ROM and documentation. *Bull. Amer. Meteor. Soc.*, **82**, 247–267.

Klein, P. M., P. A. Harr, and R. L. Elsberry, 2000: Extratropical transition of western north Pacific tropical cyclones: An overview and conceptual model of the transformation stage. *Wea. and Forecasting*, **15**, 373–395.

———, ———, and ———, 2002: Extratropical transition of western north Pacific tropical cyclones: Midlatitude and tropical cyclone contributions to reintensification. *Mon. Wea. Rev.*, **130**, 2240–2259.

Knabb R.D., and M. Mainelli, 2006: Tropical cyclone report: hurricane Ernesto 24 August–1 September 2006. National Hurricane Center, 36 pp. [Available online at http://www.nhc.noaa.gov/pdf/TCR-AL052006_Ernesto.pdf]

Kornegay, F. C., and D. G. Vincent, 1976: Kinetic energy budget analysis during interaction of tropical storm Candy (1968) with an extratropical frontal system. *Mon. Wea. Rev.*, **104**, 849–859.

Kurz, M., 1992: Synoptic diagnosis of frontogenetic and cyclogenetic processes. *Meteor. Atmos. Phys.*, **48,** 77–91.

Landsea, C. W., 1993: A climatology of intense (or major) Atlantic hurricanes. *Mon. Wea. Rev.*, **121**, 1703-1713.

Lonfat, M., F.D. Marks, and S.S. Chen, 2004: Precipitation distribution in tropical cyclones using the Tropical Rainfall Measuring Mission (TRMM) microwave imager: A Global Perspective. *Mon. Wea. Rev.*, **132**, 1645–1660.

Marks, F.D., 1985: Evolution of the structure of precipitation in hurricane Allen (1980). *Mon. Wea. Rev.*, **113**, 909–930.

———, and P. M. Austin, 1979: Effects of the New England coastal front on the distribution of precipitation. *Mon. Wea. Rev.*, **107**, 53–67.

———, L. K. Shay, and PDT-5, 1998: Landfalling tropical cyclones: Forecast problems and associated research opportunities. *Bull. Amer. Meteor. Soc.*, **79**, 305-323.

Martin, J.E., 1999: Quasigeostrophic forcing of ascent in the occluded sector of cyclones and the trowal airstream. *Mon. Wea. Rev.*, **127**, 70–88.

Matano, H, 1958: On the synoptic structure of hurricane Hazel, 1954, over the eastern United States. *J. of the Meteor. Soc. of Japan*, **36**, 23–31.

———, and M. Sekioka, 1971: Some aspects of extratropical transformation of a tropical cyclone. *J. of the Meteor. Soc. of Japan*, **49**, 736–743.

McAdie, C.J., and M.B. Lawrence, 2000: Improvements in tropical cyclone track forecasting in the Atlantic basin, 1970–98. *Bull. Amer. Meteor. Soc.*, **81**, 989–997.

McTaggart-Cowan, R., J. R. Gyakum, and M. K. Yau, 2001: Sensitivity testing of extratropical transitions using potential vorticity inversions to modify initial conditions: Hurricane Earl case study. *Mon. Wea. Rev.*, **129**, 1617–1636.

———, ———, and ———, 2003: The influence of the downstream state on extratropical transition: Hurricane Earl (1998) case study. *Mon. Wea. Rev.*, **131**, 1910–1929.

Neumann, C. J., B. R. Jarvinen, A. C. Pike, and J. D. Elms, 1993: *Tropical Cyclones of the North Atlantic Ocean, 1871–1992.* National Climatic Data Center and National Hurricane Center, Coral Gables, FL, 193 pp.

Nielsen, J. W., 1989: The formation of New England coastal fronts. *Mon. Wea. Rev.*, **117**, 1380–1401.

———, and P. P. Neilley, 1990: The vertical structure of New England coastal fronts. *Mon. Wea. Rev.*, **118**, 1793–1807.

Novak, D.R., L.F. Bosart, D. Keyser, and J.S. Waldstreicher, 2004: An observational study of cold season–banded precipitation in northeast U.S. cyclones. *Wea. Forecasting*, **19**, 993–1010.

———, J.S. Waldstreicher, D. Keyser, and L.F. Bosart, 2006: A forecast strategy for anticipating cold season mesoscale band formation within eastern U.S. cyclones. *Wea. Forecasting*, **21**, 3–23.

Palmén, E., 1958: Vertical circulation and release of kinetic energy during the development of hurricane Hazel into an extratropical storm. *Tellus*, **10**, 1–23.

Passarelli, R. E., and H. Boehme, 1983: The orographic modulation of pre-warm-front precipitation in southern New England. *Mon. Wea. Rev.*, **111**, 1062–1070.

Petterssen, S., and S. J. Smebye, 1971: On the development of extratropical cyclones. *Quart. J. Roy. Meteor. Soc.*, **97**, 457–482.

Rappaport, E. N., 2000: Loss of life in the United States associated with recent Atlantic tropical cyclones. *Bull. Amer. Meteor. Soc.*, **81**, 2065–2073.

Richwien, B. A., 1980: The damming effect of the southern Appalachians. *Nat. Wea. Dig.*, **5**, 2–12.

Ritchie, E.A., and R.L. Elsberry, 2003: Simulations of the extratropical transition of tropical cyclones: Contributions by the midlatitude upper-level trough to reintensification. *Mon. Wea. Rev.*, **131**, 2112–2128.

———, and ———, 2007: Simulations of the extratropical transition of tropical cyclones: Phasing between the upper-level trough and tropical cyclones. *Mon. Wea. Rev.*, **135**, 862–876.

Rodgers, E.B., J.J. Baik, and H.F. Pierce, 1994: The environmental influence on tropical cyclone precipitation. *J. Appl. Meteor.*, **33**, 573–593.

Roebber, P. J., J. R. Gyakum, and D. N. Trat, 1994: Coastal frontogenesis and precipitation during ERICA IOP 2. *Wea. Forecasting*, **9**, 21-44.

Schwarz, F. K., 1970: The unprecedented rains in Virginia associated with the remnants of hurricane Camille. *Mon. Wea. Rev.*, **98**, 851–859.

Shapiro, L.J., 1983: The asymmetric boundary layer flow under a translating hurricane. *J. Atmos. Sci.*, **40**, 1984–1998.

Simpson, R. H., 1974: The hurricane disaster-potential scale. *Weatherwise*, **27**, 169, 186.

Sinclair, M. R., 2002: Extratropical transition of southwest Pacific tropical cyclones. Part I: Climatology and mean structure changes. *Mon. Wea. Rev.*, **130**, 590–609.

Srock, A. F., 2005: A study of precipitation enhancement in landfalling tropical cyclones due to induced mesoscale features. M.S. Thesis, Department of Earth and Atmospheric Sciences, University at Albany/SUNY, 176 pp.

Tuleya, R.E., M. DeMaria, and R.J. Kuligowski, 2007: Evaluation of GFDL and simple statistical model rainfall forecasts for U.S. landfalling tropical storms. *Wea. Forecasting*, **22**, 56–70.